論文 / 著書情報
Article / Book Information

題目(和文)	超臨界乾燥によるリチウム空気電池の炭素電極作製
Title(English)	Supercritical drying process for fabricating carbon electrodes for Li-air battery
著者(和文)	サキナソフィヤ
Author(English)	Shofiyah Sakinah
出典(和文)	学位:博士(工学), 学位授与機関:東京工業大学, 報告番号:甲第12426号, 授与年月日:2023年3月26日, 学位の種別:課程博士, 審査員:下山 裕介,関口 秀俊,久保内 昌敏,多湖 輝興,松本 秀行
Citation(English)	Degree:Doctor (Engineering), Conferring organization: Tokyo Institute of Technology, Report number:甲第12426号, Conferred date:2023/3/26, Degree Type:Course doctor, Examiner:,,,,
学位種別(和文)	博士論文
Type(English)	Doctoral Thesis

SUPERCRITICAL DRYING PROCESS FOR FABRICATING CARBON ELECTRODES FOR LI-AIR BATTERY

SHOFIYAH SAKINAH

IN THE PARTIAL FULFILLMENT OF THE REQUIREMENTS FOR THE DEGREE OF DOCTOR OF ENGINEERING (CHEMICAL SCIENCE AND ENGINEERING)

GRADUATE SCHOOL OF MATERIAL AND CHEMICAL TECHNOLOGY

TOKYO INSTITUTE OF TECHNOLOGY

MARCH 2023

Acknowledgment

This Ph.D. dissertation was accomplished thanks to Allah and the help of many individuals around me. I want to express my gratitude to Sato-Yo International Scholarship Foundation, which helps me during my study.

I want to thank my academic advisor, Professor Yusuke Shimoyama, for always being there for me with advice, assistance, and helpful suggestions for my laboratory life. This dissertation would not have been completed without his guidance. I am also grateful to all professors and lecturers at the Chemical Science and Engineering Department who have shared their knowledge with me in class.

I thank all Shimoyama laboratory members, especially Nattanai Kunanusont, Yuya Murakami, Peany Houng, Hao Yingquan, Thossaporn Wijakmatee, and others, for valuable comments and polite chats during the research meeting.

I would also like to thank my parents, Haznan Abimanyu and Dessy Gumilan Sari; my sisters, Aisyah Tsabitah and Khodijah Syukriyah; and my brothers, Musthafa Al-Akhyar and Muhammad Faiz Abdurrahman who have always been there for me from afar.

Table of Contents

List of Figures

List of Table

Chapter 1 Introduction

1.1 Background and motivation

The drying industry develops because of science and requires more specific and advanced materials, especially in manufacturing microelectronic chips and biological products. To obtain those materials, researchers have been searching for an alternative method for heat drying or evaporation drying in recent years due to its disadvantages in having surface tension and capillary stress causing the materials' pores to collapse. Then, supercritical-assisted drying was introduced as a new method. Supercritical-assisted drying is a method that uses a fluid above its critical points, which is called a supercritical fluid [1,2]. The unique characteristic of this fluid is that it has both liquid and gas characteristics, where it has the density of a liquid, the viscosity of the gas, and the thermal conductivity and diffusion coefficient between gas and fluid [3]. Carbon dioxide is usually used in the actual application since it has a relatively low critical point.

Moreover, supercritical carbon dioxide ($scCO_2$) is known for its properties such as inertness, inflammability, non-toxicity, low cost, and availability in high purity [4]. Then, $scCO_2$ is used in supercritical-assisted drying, which is proven superior in fabricating highly porous materials [5-7]. Even though many researchers stated the advantage of supercritical drying, only a few explanations of this method's mechanism and factors affecting the drying products are available.

In today's energy field, Li-air batteries are expected to be alternative fuels in resolving the environmental challenges caused by fossil fuels because of their high potential energy compared to Li-ion batteries. Gasoline is told to have a theoretical energy density of 13,000 W h kg^{-1}, while Li-air battery is 11,680 W h kg^{-1}. However, the practical use of gasoline and Li-air battery is still low compared to their theoretical value [8]. However, another research found that modifying the combination of gases for the battery affects its performance. For example, the gas supply combination of O_2 and CO_2, where the CO_2 amount is 50 %, shows a high capacity of 6,750 mA h g^{-1} when supplying only O_2 or CO_2 shows a low discharge capacity [9].

In the Li-air battery, the cathode is the most substantial part of the battery that can limit its performance. The battery fails primarily due to the cathode pores clogging by discharge

products, which prevents gas from entering the system; thus, the discharging could not continue. As a result, a cathode with high porosity is required to optimize battery performance [10, 11].

Then, the combination of these pieces of information, a successful example of manufacturing a high-porosity carbon electrode using supercritical drying, was recently published. However, porous electrodes have been found to limit battery cyclability because discharged products might shatter the electrode pores due to their low mechanical strength. Although increasing the cathode's polymer content, which bonded carbon particles, could increase the cyclability, the discharge capacity fell [12]. Therefore, mechanical strength must be improved without increasing the polymer content.

Besides acetylene carbon black, which was used in the previous research, other carbon types can be considered for the conductive material. Carbon nanostructures such as fullerenes, carbon nanotubes, and carbon nanofibers are chosen for many electrical applications due to their excellent electrical, thermal, and mechanical properties [13]. However, due to its easy production and low cost, carbon nanofiber is the best candidate for carbon black's alternatives [14,15].

This research aims to understand the expansion behavior and homogeneous formation of solvent and $scCO_2$ to manage the structure of porous materials. Additionally, the information of solvent and $scCO_2$ behavior was applied in fabricating electrodes using the robust carbon nanofiber. Finally, optimize the carbon electrode fabrication with supercritical drying.

1.2 The objective of this research

This research is divided into two kinds of experiments; fundamental and applicative experiments. For the fundamental experiment, several solvents with $scCO_2$ were explored under diverse supercritical fluid parameters such as pressurization rate, temperature, type of solvent, solvent quantity, and CO_2 flow rate using a high-pressure cell with an observation window to understand its expansion behavior and homogeneous formation better.

Then, for the applicative experiment, carbon aerogels were fabricated by utilizing supercritical drying with varied solvent compositions and drying temperatures to evaluate the effect of drying parameters on aerogel structure. Moreover, carbon nanofiber is applied to the electrode instead of carbon black to investigate the effect of conductive material type on the battery performance.

Finally, an experiment using the results of fundamental and applicative experiments was conducted to obtain an optimized electrode for Li-air battery application.

1.3 Contents of dissertation

Chapter 1 discusses the research's background and motivation, followed by the objective of this research. Then comes a brief description of the dissertation's contents.

Chapter 2 describes the fundamentals of Li-O_2/CO_2 batteries and supercritical fluid, including their recent application and research.

Chapter 3 discusses the experiments and research for solvent expansion and homogeneous formation of organic solvent with $scCO_2$. This section describes how the experiment was carried out utilizing a view cell apparatus and the research of solvent expansion and homogeneous formation under various supercritical fluid parameters such as pressurization rate, temperature, solvent type, solvent amount, and CO_2 flow rate.

Chapter 4 explains the experiment and investigation of electrode fabrication using $scCO_2$ drying and the effect of drying parameters on the battery morphology. The experiment was carried out as applicative experiment of chapter 3. Where, in chapter 3, the experiment only used organic solvent and CO_2 while in this chapter, the actual electrode fabrication with various drying parameters were held. Drying parameters which were investigated in this chapter are solvent amount and drying temperature. Then, carbon nanofiber is used as an alternative to carbon black for electrode ingredients. It also explains the application of fabricated carbon nanofiber electrodes for Li-air batteries.

Chapter 5 focuses on the experimental and investigation section for carbon nanofiber aerogel fabrication by $scCO_2$ for electrode optimization from the results of Chapter 3 and Chapter 4. The investigation includes morphology, porosity measurement, and battery performance.

Chapter 6 will summarize all results of this research and the direction of possible future works.

1.4 References

[1] Marzouk Benali, Yacine Boumghar, "Supercritical Fluid-Assisted Drying", *Handbook of Industrial Drying (4th Edition)* (2014) 1261-1269

[2] Nathalie Job, Alexandre Théry, René Pirard, José Marien, Laurent Kocon, Jean-Noël Rouzaud, François Béguin, Jean-Paul Pirard, "Carbon aerogels, cryogels and xerogels: Influence of the drying method on the textural properties of porous carbon materials", *Carbon* 43 (2005) 2481-2494

[3] Wei Du, Rasool Kamal, Zongbao K.Zhao, "Biodiesel", *Comprehensive Biotechnology (Third Edition)* (2019) 66-78

[4] Bengisu Topuz, Gülçin Günal, Selcan Guler, Halil Murat Aydin, "Use of supercritical CO_2 in soft tissue decellularization", *Methods in Cell Biology* 157 (2020) 49-79

[5] İbrahim Şahin, Yaprak Özbakır, Zeynep İnönü, Zeynep Ulker, and Can Erkey, "Kinetics of Supercritical Drying of Gels", *Gels* 4 (2018)

[6] Motohiro Kinoshita, Taiki Sugamura, YusukeShimoyama, "Effect of solvent species inside wet gel on fabrication of titania nanoparticle by supercritical carbon dioxide drying", *The Journal of Supercritical Fluids* 110 (2016) 90-96

[7] Nobuyuki Kawakami, Yoshito Fukumoto, Takashi Kinoshita, Kohei Suzuki and Ken-ichi Inoue, "Preparation of Highly Porous Silica Aerogel Thin Film by Supercritical Drying", *Japanese Journal of Applied Physics* 39 (2000) 182-184

[8] G. Girishkumar, B. McCloskey, A. C. Luntz, S. Swanson, and W. Wilcke, "Lithium-air battery: Promise and challenges", *The Journal of Physical Chemistry Letters* 1 (2010) 2193-2203

[9] Kensuke Takechi, Tohru Shiga and Takahiko Asaoka, "A Li–O_2/CO_2 battery", *Chemical Communications* 47 (2011) 3463-3465

[10] Alexander Kraytsberg and Yair Ein-Eli, "Review on Li–air batteries—Opportunities, limitations and perspective", *Journal of Power Sources* 196 (2011) 886-893

[11] S. Reza Younesi, Sigita Urbonaite, Fredrik Björefors, KristinaEdström, "Influence of the cathode porosity on the discharge performance of the lithium–oxygen battery", *Journal of Power Sources* 196 (2011) 9835-9838

[12] Nattanai Kunanusont and Yusuke Shimoyama, "Porous carbon electrode for Li-air battery fabricated from solvent expansion during supercritical drying", *The Journal of Supercritical Fluids* 133 (2018) 77-85

[13] Quoc Ngo, Toshishige Yamada, Makoto Suzuki, Yusuke Ominami, Alan M. Cassell, Jun Li, M. Meyyappan, and Cary Y. Yang, "Structural and Electrical Characterization of Carbon Nanofibers for Interconnect Via Applications", *IEEE Transactions on Nanotechnology* 6 (2007) 688-695

[14] Chenyu Wei and Deepak Srivastava, "Nanomechanics of carbon nanofibers: Structural and elastic properties", *Applied Physics Letters* 85 (2004) 2208

[15] Inpil Kang, Yun Yeo Heung, Jay H.Kim, Jong Won Lee, Ramanand Gollapudi, Srinivas Subramaniam, Suhasini Narasimhadevara, Douglas Hurd, Goutham R. Kirikera, Vesselin Shanov, Mark J.Schulz, Donglu Shi, Jim Boerio, Shankar Mall, Marina Ruggles-Wren, "Introduction to carbon nanotube and nanofiber smart materials", *Composites Part B: Engineering* 37 (2006) 382-394

Chapter 2 Literature Review

2.1 Supercritical fluid

2.1.1 Supercritical carbon dioxide and its characteristic

A supercritical fluid exists at pressures and temperatures exceeding its critical point. Its unusual features, the combination of liquid and gas phases shown in Table 2.1, make it widely used. These properties can be controlled by changing pressure and temperature. Carbon dioxide is the most used compound in a supercritical state because of its inertness, inflammability, non-toxicity, low cost, and availability in high purity, and it has a low critical point which is easier to handle. It reaches a critical state above 31.1 °C and 7.38 MPa [1, 2].

There are many applications of supercritical fluid. For example, supercritical fluid can extract compounds for food [3] and the oil industry [4] because of its high solubility with hydrophobic compounds. Furthermore, in the pharmaceutical field, active pharmaceutical ingredients (APIs) alone or combined with various biodegradable polymers are recrystallized with supercritical fluid to improve their physical qualities, such as bioavailability [5]. Also, a supercritical fluid is used as an anti-solvent to produce 3D materials [6] and nanoparticles [7, 8] by a supercritical drying process.

2.1.2 Supercritical carbon dioxide drying

The drying process is mainly separated into three types: evaporation, freeze, and supercritical, and the products are called xerogel, cryogel, and aerogel, respectively. In conventional drying, evaporation drying is the simplest because it requires heating only. However, because it requires high temperatures and a long time to remove the solvent, it uses much energy and time, which is inefficient. Moreover, the probability of getting a highly porous material is less because surface tension and capillary stress in evaporation drying damage the pores [9, 10].

In modern drying methods, freeze-drying and supercritical drying are introduced. Freeze-drying is a method where the solvent is frozen and sublimated. This method can retain the material's pores; however, the pores are mainly macroporous and irregular. In the case of supercritical drying, because supercritical fluid and organic solvent will form a homogenous phase, the surface tension and capillary stress will not damage the pores. Furthermore, by using

$scCO_2$ as the supercritical fluid, drying can be done at a moderate temperature and pressure. Thus, a highly porous material can be obtained [11].

Huang et al. explain in their paper that drying DMAC from poly(vinylidene fluoride) or PVDF at varied operating temperatures and pressures results in varying porosity, as seen in Figure 2.1. Higher temperature results in slightly low porosity, while higher pressure results in slightly higher porosity [12]. Another study on highly porous carbon electrodes made with supercritical drying found that high pressure led to more significant porosity [13]. These findings indicate that supercritical drying parameters are vital to control a material's porosity. Examples of porous materials fabricated by supercritical drying are shown in Table 2.2.

2.2 Li-air battery

The Li-air battery is expected to be a fossil fuel alternative to tackle environmental problems due to fossil fuel because of its high potential energy compared to Li-ion batteries, and oxidation of 1 kg lithium releases 11,680 W h $kg^{-1,}$ which is comparable with gasoline. However, although Li-air battery is expected to become a fossil fuel substitute, there are challenges in improving the anode, air cathode, and electrolyte to meet the expectation [24].

Products are deposited inside the pores of the air cathode as a result of the discharge reaction. The gas that needs to enter the battery system is obstructed due to this deposition, limiting battery performance. According to certain studies, an air cathode's pore volume, porosity, and thickness are required to create places for the reaction products to deposit. Therefore, a high porosity air cathode with large pores is necessary to boost battery performance [25, 26]. The illustration of the clogged cathode and the ideal cathode is shown in Figure 2.1.

In research by Takechi et al., a Li-air battery using an O_2 and CO_2 mixture with a CO_2 ratio of 50 % can improve the battery's capacity three times higher than a Li-air battery using pure CO_2. However, although it has high battery capacity because the discharge reaction produces $Li_2CO_{3,}$ which is difficult to decompose, Li-O_2/CO_2 battery is told to be suitable as a primary battery that is supposed to be used once and then discarded [27].

The other report explains that Li-O_2/CO_2 (1:1) using DME and DMSO-based electrolytes can be recharged. Because, Li_2CO_3, which is the main product of the discharge reaction, did not appear after charging [28]. In addition, some air cathode research was conducted to increase battery performance; some of the research is summarized in Table 2.3.

Table 2.1 Gas, Supercritical, and liquid properties

	Density (g cm^{-3})	Diffusion (cm^2 s^{-1})	Viscosity (g $cm^{-1} \cdot s^{-1}$)
Gas	10^{-3}	10^{-1}	10^{-4}
Supercritical	10^{-1} to 1 Liquid like	10^{-4} to 10^{-3} Liquid like	10^{-4} to 10^{-3} Gas like
Liquid	1	$<10^{-5}$	10^{-2}

Table 2.2 Porous materials fabricated by $scCO_2$ drying

Materials	Precursor solution	Drying condition	Application	Ref.
RuO_2-loaded PVDF HFP aerogels	PVDF HFP/acetone/ethanol solution	200 bar 35 ºC	Supercapacitor	[14]
Agar aerogel	Agar/water gel undergone solvent exchange with ethanol	10 MPa 313 K	Pharmaceutical	[15]
β-chitin aerogel	*β*-chitin/water gel undergone solvent exchange with 2-propanol	10 MPa 60 ºC	Biotechnology	[16]
Porous silicon	Silicon/ethanol	100 bar 40 ºC	N/A	[17]
Cellulose nanofibrils aerogel	Cellulose nanofibrils in ethanol/water	100 bar 45 ºC	Food, cosmetic, biomedical	[18]
Ag nanoparticle-loaded cellulose nanofiber aerogels	Carbon nanofibril hydrogel in ethanol	20 MPa 373 K	Antibacterial and antifungal	[19]
Canola protein aerogels	Canola seed meal treated with $CaCl_2$, solvent exchange to ethanol	N/A	Biological applications	[20]
CMC-HEC aerogel	Carboxymethylcellulose/ 3-hydroxyethylcellulose hydrogel in ethanol	200 bar 45 ºC	Hygiene, agriculture, pharmaceutical, and biomedical fields	[21]
Vitamin-loaded starch aerogel	Starch hydrogel-vitamin loaded in ethanol	20 MPa 45 ºC	Biomedical	[22]
MWCNT interconnected $NiCo_2O_4$ aerogels	Ni-Co precursor/MWCNT in DMF	1000 psi 14 ºC	Ethanol fuel cell	[23]

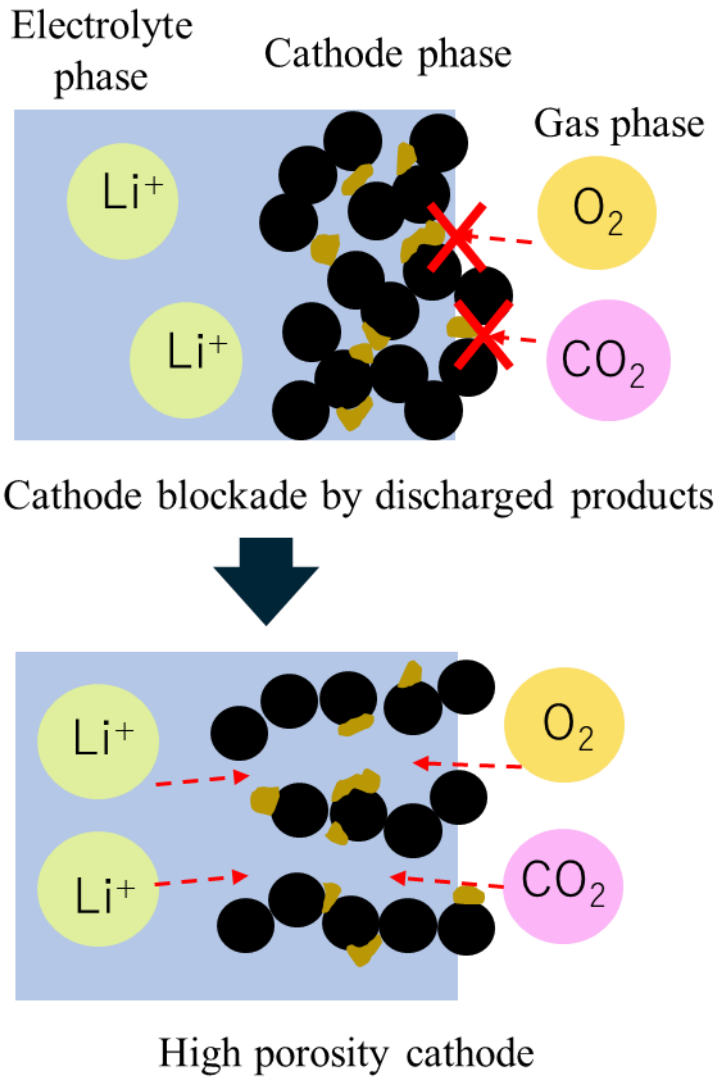

Figure 2.1 Illustration of the air-cathode problem and the ideal air-cathode

Table 2.3 Summary of Li-air battery research

Cathode materials	Electrolyte	Max capacity (mA h g^{-1})	Cyclability	Ref.
KB/PVDF on Ni meshed	$LiPF_6$ in DMSO	2300	21 cycles	[28]
KB/PTFE on stainless steel meshed	$LiCF_3SO_3$ in TEGDME	1800	10 cycles (30 h/cycle)	[29]
Super P/PTFE on stainless steel meshed	$LiClO_4$ in DMSO	9750	17 cycles (10 h/cycle)	[30]
KB/Bi-CoPc/PTFE on Nickel foam	LiTFSI and Bi-CoPc in TEGDME	7000	171 cycles (5 h/cycle)	[31]
Ru/N-doped carbon nanotube/PVDF on carbon paper	LiTFSI in TEGDME	12000	190 cycles (5 h/cycle)	[32]
Macroporous-mesoporous carbon (MMC) from mesoporous SiO_2 with NiO as the template	$LiNO_3$ in DMAc	2799	55 cycles (5 h/cycle)	[33]
Cathode with mesoporous/macroporous Co_3O_4 ultrathin nanosheets	LiTFSI in TEGDME	11 882	80 cycles (2.5 h/cycle)	[34]
Super P	LiTFSI in [bmim][Tf_2N]	100	N/A	[35]
CNTs	LiTFSI in TEGDME	8379	29 cycles (20 h/cycle)	[36]
3D NCNT/G	LiTFSI in $LiNO_3$/DMSO	17534.1	185 cycles (10 h/cycle)	[37]

2.3 Carbon nanofiber

Nowadays, many researchers are trying to invent renewable energy. However, most renewable energy needs large-scale energy storage and must be efficient, low cost, and environment friendly. Carbon-based electrodes are widely used for those energy storage devices due to their electrical quality, such as capacity, energy density, and power density [38].

In the Li-air battery world, carbon is widely utilized for the cathode compartment, letting the gases enter the battery system, and the gases react with lithium-ion on the carbon surface. Carbon is used mainly because of its low cost but it has high conductivity and surface area [39]. Furthermore, there are carbon nanotubes and carbon nanofibers in various types of carbon, which are expected to be excellent material composites [40]. However, since carbon nanofiber is easier to produce and cheaper than carbon nanotube, it is expected to be in the front for electrochemical application.

2.4 References

[1] Xiaoxue Zhang, Saara Heinonen and Erkki Levänen, "Applications of supercritical carbon dioxide in materials processing and synthesis", *RSC Advances* 4 (2014) 61137-61152

[2] Walter Leitner, "Designed to dissolve", *Nature* 405 (2000) 129-130

[3] Maša Knez Hrnčič, Darija Cör, Mojca Tancer Verboten, Željko Knez, "Application of supercritical and subcritical fluids in food processing", *Food Quality and Safety* 2 (2018) 59-67

[4] Praskovya L. Pavlova, Andrey V. Minakov, Dmitriy V. Platonov, Vladimir A. Zhigarev, and Dmitriy V. Guzei , "Supercritical Fluid Application in the Oil and Gas Industry: A Comprehensive Review", *Sustainability* 14 (2022) 698

[5] Ranjith Kumar Kankala, Yu Shrike Zhang, Shi-Bin Wang, Chia-Hung Lee, Ai-Zheng Chen, "Supercritical Fluid Technology: An Emphasis on Drug Delivery and Related Biomedical Applications", *Advanced Healthcare Materials* 6 (2017) 1700433

[6] C. A. García-González, M. C. Camino-Rey, M. Alnaief, C. Zetzl, I. Smirnova, "Supercritical drying of aerogels using CO_2: Effect of extraction time on the end material textural properties", *The Journal of Supercritical Fluids* 66 (2012) 297-306

[7] K.Byrappa, S.Ohara, T.Adschiri, "Nanoparticles synthesis using supercritical fluid technology – towards biomedical applications", *Drug Delivery Reviews* 60 (2008) 299-327

[8] Yuya Murakami, Yusuke Shimoyama, "Supercritical extraction of emulsion in microfluidic slug-flow for production of nanoparticle suspension in aqueous solution", *The Journal of Supercritical Fluids* 118 (2016) 178-184

[9] G. Conzatti, D. Faucon, M. Castel, F. Ayadi, S. Cavalie, A. Tourrette, "Alginate/chitosan polyelectrolyte complexes: A comparative study of the influence of the drying step on physicochemical properties", *Carbohydrate Polymers* 172 (2017) 142-151

[10] Mahnaz Shahzamani, Rouhollah Bagheria, Mahmood Masoomi, Majid Haghgoo, Akram Dourani, "Effect of drying method on the structure and porous texture of silica-polybutadiene hybrid gels: Supercritical vs. ambient pressure drying", *Journal of Non-Crystalline Solids* 460 (2017) 119-124

[11] Mariangela Guastaferro, Ernesto Reverchon and Lucia Baldino, "Polysaccharide-Based Aerogel Production for Biomedical Applications: A Comparative Review", *Materials* 14 (2021) 1631

[12] Shirong Huang, Guozhong Wu, Shimou Chen, "Preparation of microporous poly(vinylidene fluoride) membranes via phase inversion in supercritical CO_2", *Journal of Membrane Science* 293 (2007) 100-110

[13] Nattanai Kunanusont and Yusuke Shimoyama, "Porous carbon electrode for Li-air battery fabricated from solvent expansion during supercritical drying", *The Journal of Supercritical Fluids* 133 (2018) 77-85

[14] Maria Sarnoa, Carmela Scudieri, Eleonora Ponticorvo, Lucia Baldino, Stefano Cardea, Ernesto Reverchon, "High performance PVDF HFP_RuO_2 supercapacitors production by supercritical drying", *The Journal of Supercritical Fluids* 176 (2021) 1055323

[15] M. P. Dirauf, P. C. Wagner, A. S. Braeuer, "Mass transfer kinetics inside bio-(aero)gels during solvent exchange and supercritical drying: On the relevance of advection, gel-porosity and a peculiarity regarding the tortuosity", *The Journal of Supercritical Fluids* 191 (2022) 105762

[16] Pakavadee Ratanajiajaroen, Masahiro Ohshima, "Preparation of highly porous β-chitin structure through nonsolvent–solvent exchange-induced phase separation and supercritical CO_2 drying", *The Journal of Supercritical Fluids* 68 (2012) 31-38

[17] St. Frohnhoff, R. Arens-Fischer, T. Heinrich, J. Fricke, M. Arntzen, W. Theiss, "Characterization of supercritically dried porous silicon", *Thin Solid Films* 255 (1995) 115-118

[18] Clémentine Darpentignyb, Guillaume Nonglaton, Julien Bras, Bruno Jean, "Highly absorbent cellulose nanofibrils aerogels prepared by supercritical drying", *Carbohydrate Polymers* 229 (2020) 115560

[19] Juntao Tang, Yang Song, Feiping Zhao, Stewart Spinney, Juliana da Silva Bernardes, Kam Chiu Tam, "Antibacterial and antifungal properties of Ag nanoparticle-loaded cellulose nanofiber aerogels prepared by supercritical CO_2 drying", *The Journal of Supercritical Fluids* 143 (2019) 44568

[20] Sarah E. FitzPatrick, Santanu Deb-Choudhury, Steve Ranford, Mark P. Staiger, "Canola protein aerogels via salt-induced gelation and supercritical carbon dioxide drying", *European Polymer Journal* 168 (2022) 111126

[21] Lucia Baldino, Simona Zuppolini, Stefano Cardea, Laura Diodato, Anna Borriello, Ernesto Reverchon, Luigi Nicolais, "Production of biodegradable superabsorbent aerogels using a supercritical CO_2 assisted drying", *The Journal of Supercritical Fluids* 156 (2020) 104681

[22] Iolanda De Marco, Ernesto Reverchon, "Starch aerogel loaded with poorly water-soluble vitamins through supercritical CO_2 adsorption", *Chemical Engineering Research and Design* 119 (2017) 221-230

[23] Santhana Sivabalan, Jayaseelan Tae-Hoon, Ko S. Radhakrishnan, Cheol-Min Yang, Hak-Yong Kim, Byoung-Suhk Kim, "Novel MWCNT interconnected NiCo2O4 aerogels prepared by a supercritical CO_2 drying method for ethanol electrooxidation in alkaline media", *International Journal of Hydrogen Energy* 41 (2016) 13504-13512

[24] G. Girishkumar, B. McCloskey, A. C. Luntz, S. Swanson, and W. Wilcke, "Lithium-air battery: Promise and challenges", *The Journal of Physical Chemistry Letters* 1 (2010) 2193-2203

[25] S. Reza Younesi, Sigita Urbonaite, Fredrik Björefors, KristinaEdström, "Influence of the cathode porosity on the discharge performance of the lithium–oxygen battery", *Journal of Power Sources* 196 (2011) 9835-9838

[26] Chao Shen, Jianxin Xie, Teng Liu, Mei Zhang, Petru Andrei, Liyu Dong, Mary Hendrickson, Edward J. Plichta and Jim P. Zheng, "Influence of Pore Size on Discharge Capacity in Li-Air Batteries with Hierarchically Macroporous Carbon Nanotube Foams as Cathodes", *Journal of The Electrochemical Society* 165 (2018) A2833

[27] Kensuke Takechi, Tohru Shiga and Takahiko Asaoka, "A Li–O_2/CO_2 battery", *Chemical Communications* 47 (2011) 3463-3465

[28] Hyung-Kyu Lim, Hee-Dae Lim, Kyu-Young Park, Dong-Hwa Seo, Hyeokjo Gwon, Jihyun Hong, William A. Goddar, Hyung jun Kim, and Kisuk Kang, "Toward a Lithium–"Air" Battery: The Effect of CO_2 on the Chemistry of a Lithium–Oxygen Cell", *Journal of the American Chemical Society* 135 (2013) 9733-9742

[29] Yali Liu, Rui Wang, Yingchun Lyu, Hong Li and Liquan Chen, "Rechargeable Li/CO_2–O_2 (2 : 1) battery and Li/CO_2 battery", *Energy & Environmental Science* 7 (2014) 677-681

[30] Wei Yin, Alexis Grimaud, Florent Lepoivre, Chunzhen Yang, and Jean Marie Tarascon, "Chemical vs Electrochemical Formation of Li_2CO_3 as a Discharge Product in Li−O_2/CO_2 Batteries by Controlling the Superoxide Intermediate", *The Journal of Physical Chemistry Letter* 8 (2017) 214-222

[31] Zixuan Liu, Yantao Zhang, Chuankun Jia, Hao Wan, Zhe Peng, Yujing Bi, Yang Liu, Zhangquan Peng, Qing Wang, Hong Li, Deyu Wang, Ji-Guang Zhang, "Decomposing lithium carbonate with a mobile catalyst", *Nano Energy* 36 (2017) 390-397

[32] Peng-Fang Zhang, Yan-Qiu Lu, Yi-Jin Wu, Zu-Wei Yin, Jun-Tao Li, Yao Zhou, Yu-Hao Hong, Yu-Yang Li, Ling Huang, Shi-Gang Sun, "High-performance rechargeable Li-CO_2/O_2 battery with Ru/N-doped CNT catalyst", *Chemical Engineering Journal* 363 (2019) 224-233

[33] Do Youb Kim, Xing Jin, Chang Hyun Lee, Dong Wook Kim, Jungdon Suk, Jeong Kuk Shon, Ji Man Kim, Yong ku Kang, "Improved electrochemical performance of ordered mesoporous carbon by incorporating macropores for Li–O_2 battery cathode", *Carbon* 133 (2018) 118-126

[34] Feng Wu, Xiaoxiao Zhang, Taolin Zhao, Renjie Chen, Yusheng Ye, Man Xie and Li Li, "Hierarchical mesoporous/macroporous Co_3O_4 ultrathin nanosheets as free-standing catalysts for rechargeable lithium–oxygen batteries" *Journal of Materials Chemistry A* 3 (2015) 17620-17626

[35] Shaomao Xu, Shyamal K. Das, and Lynden A. Archer, "The Li-CO_2 battery: a novel method for CO_2 capture and utilization", *RSC Advances* 3 (2013) 6656

[36] Xin Zhang, Qiang Zhang, Zhang Zhang, Yanan Chen, Zhaojun Xie, Jinping Wei and Zhen Zhou, "Rechargeable Li-CO_2 batteries with carbon nanotubes as air cathodes", *Chemical Communications* 51 (2015) 14636-9

[37] Ying Xiao, Feng Du, Chuangang Hu, Yong Ding, Zhong Lin Wang, Ajit Roy, and Liming Dai, "High-Performance Li-CO_2 Batteries from Free-Standing, Binder-Free, Bifunctional Three-Dimensional Carbon Catalysts", *ACS Energy Letters* 5 (2020) 916-921

[38] Jazer Jose H.Togonon, Pin-Chieh Chiang, Hong-Jhen Lina, Wei-CheTsai, Hung-Ju Yen, "Pure carbon-based electrodes for metal-ion batteries", *Carbon Trends* 3 (2021) 100035

[39] Zhaoyin Wen, Chen Shen, Yan Lu, "Air Electrode for the Lithium–Air Batteries: Materials and Structure Designs", *ChemPlusChem* 80 (2015) 270-287

[40] Inpil Kang, Yun Yeo Heung, Jay H.Kim, Jong Won Lee, Ramanand Gollapudi, Srinivas Subramaniam, Suhasini Narasimhadevara, Douglas Hurd, Goutham R. Kirikera, Vesselin Shanov, Mark J.Schulz, Donglu Shi, Jim Boerio, Shankar Mall, Marina Ruggles-Wren, "Introduction to carbon nanotube and nanofiber smart materials", *Composites Part B: Engineering* 37 (2006) 382-394

Chapter 3 Investigation of organic solvent expansion under supercritical CO_2

3.1 Statement of problems and objectives

Understanding solvent expansion behavior and homogeneous phase, as described in Chapter 1, are vital for controlling the structure of electrodes or materials via supercritical drying. In this part, several solvents with supercritical carbon dioxide under diverse parameters of supercritical fluid: pressurization rate, temperature, type of solvent, solvent quantity, and CO_2 flow rate are examined.

3.2 Experimental

3.2.1 Materials

Acetone (purity 99.0 %), 1-butanol (purity 99.0 %), ethanol (purity 99.5%), 1-Methyl-2-pyrrolidone (NMP, with purity higher than 99.0 %), dimethyl sulfoxide (DMSO, with purity higher than 99.0 %), and o-xylene (purity higher than 98.0 %) were supplied from Wako Pure Chemical Industries, Ltd. Carbon dioxide (CO_2) with the purity over 99.5 % was supplied by Fujii-Bussan Co., Ltd. The molecular structures of organic solvents are shown in Figure 3.1.

3.2.2 Apparatus and procedure

High pressure was utilized along with an examination window or view cell to study solvent expansion, where the apparatus is shown in Figure 3.2. First, the view cell was warmed to prevent sudden temperature rise when pressurization started. Then, a predetermined amount of the organic solvent described in Table 3.1 was added to a glass cell, installed in a view cell, and the view cell was tightly closed. The temperature of the view cell was fixed to 40 °C before the experiment began. For the temperature parameter experiment, in addition to 40 °C, the temperature was set to 60 and 80 °C.

CO_2 from a CO_2 cylinder was delivered through a silica gel column and cooled down to form liquified CO_2. The liquified CO_2 was pumped into the cell until the pressure meter reading was 20 MPa. The examination of organic solvents and supercritical carbon dioxide was continued until it reached the homogeneous phase, and the whole process was captured with a video camera in a batch method. The experiment was carried out under various conditions displayed in Table 3.1.

For the CO_2 flow rate parameter investigation, after the system reached 20 MPa, the control valve at the exit of the apparatus was opened to allow CO_2 to flow out. A control valve controls the flow of CO_2 while monitoring the flow meter.

3.2.3 Analysis

The time from the start of the experiment until the pressure hit 20 MPa was plotted against the expansion rate. The initial height of the solvent is given as h_0, the height of the solvent over time is given as h, and the expansion rate is given as h/h_0. The experiment was then repeated with the variation of pressurization rates, solvent amounts, apparatus temperatures, solvent type, and CO_2 flow rate to investigate the effect on solvent expansion and homogeneous phase development.

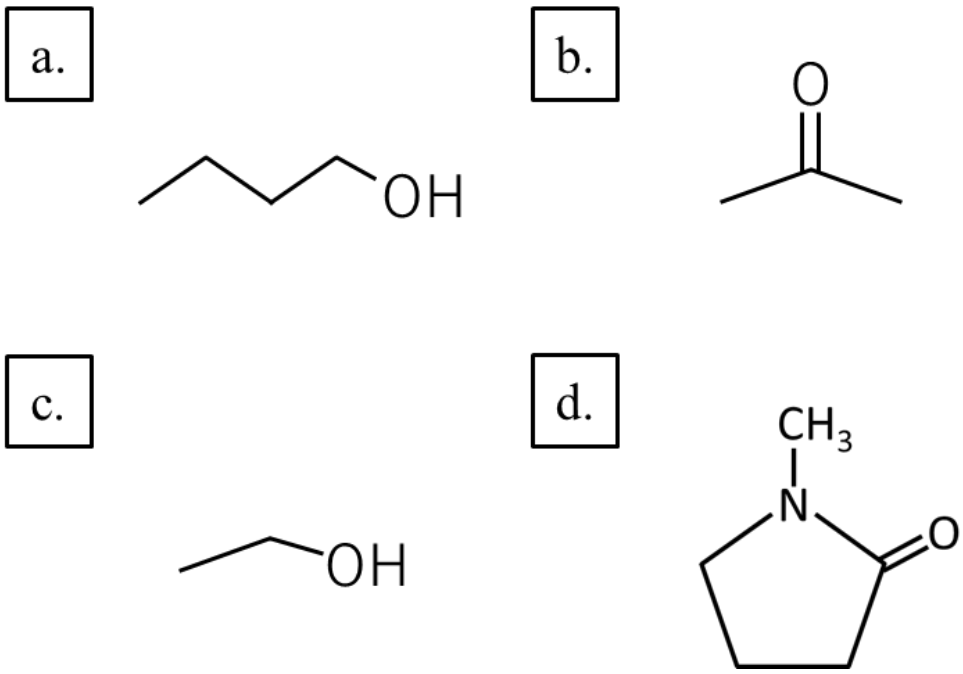

Figure 3.1 Solvent molecular structure: a) acetone, b) 1-butanol, c) ethanol, and d) NMP

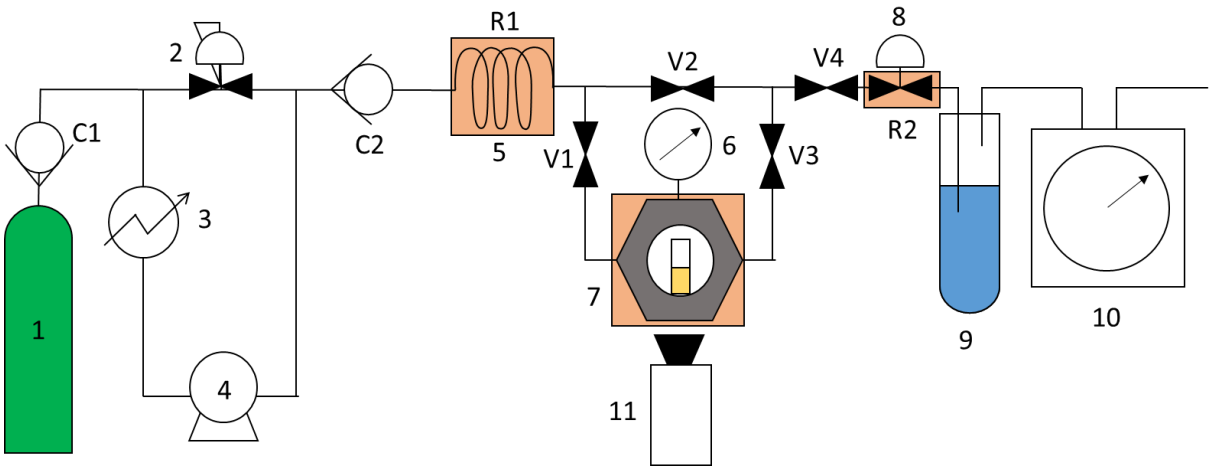

1. Liquefied carbon dioxide
2. Back pressure valve
3. Condenser
4. Pump
5. Heat coil
6. Pressure meter
7. View-cell
8. Control valve
9. Solvent trap
10. Flow meter
11. Video camera

C1-C2 Check valve

V1-4 Stop valve

R1-2 Ribbon heater

Figure 3.2 Apparatus scheme for view cell experiment

Table 3.1 Experiment conditions for view cell experiment

Solvent	Quantity (mmol)	Pressurization rate ($MPa \cdot min^{-1}$)	Temperature (°C)	Average CO_2 outlet flow rate ($ml \cdot min^{-1}$)	Average CO_2 outlet flow rate ($mol \cdot min^{-1}$)
Pressurization rate parameter					
NMP	7.6067	0.234	40		
NMP	7.6435	0.513	40	Batch	
NMP*	7.6415	0.964	40		
Temperature parameter					
NMP*	7.6415	0.964	40		
NMP	7.6405	1.34	60	Batch	
NMP	7.5779	1.67	80		
Ethanol	7.7209	1.12	40		
Ethanol	7.5646	1.33	60	Batch	
Ethanol	7.6644	1.33	80		
Acetone	7.6687	1.32	40		
Acetone	7.5826	1.32	60	Batch	
Acetone	7.5964	1.34	80		
Solvent type parameter					
NMP**	5.0207	1.34	40		
Acetone	5.0740	1.35	40		
1-butanol	5.0567	1.66	40	Batch	
Ethanol	5.0901	1.34	40		
DMSO	5.0877	1.98	40		
o-xylene	5.0518	1.90	40		
Solvent amount parameter					
NMP	3.9120	1.70	40		
NMP**	5.0207	1.34	40	Batch	
NMP*	7.6415	0.964	40		
NMP	9.8003	1.14	40		
Flow rate parameter					
NMP*	7.6415	0.964	40	Batch	
NMP	7.6112	1.33	40	96.21	3.90×10^{-3}
NMP	7.6092	1.55	40	146.6	5.94×10^{-3}
NMP	7.6516	1.55	40	200.3	8.12×10^{-3}

* Same data

** Same data

3.3 Result and discussion

3.3.1 Pressurization rate parameter

Figure 3.3 depicts a video camera illustration for various pressurization speeds. The images indicate that $scCO_2$ dissolves into the solvents in the first stage, causing the solvent volume to grow. When the solvent expands, the black and gray phases are visible. The black phase is the CO_2-rich phase, while the gray phase is the CO_2-low phase. The solvent height decreases after the expansion phase, which could be happened after the $scCO_2$ amount entering the solvent reaches a saturation point. Thus, the solvent transfer to the supercritical $scCO_2$ phase is greater than the $scCO_2$ transfer to the solvent phase. Finally, after some time, $scCO_2$ and solvent form a homogeneous phase where the border of solvent and $scCO_2$ cannot be observed. Figure 3.4, Figure 3.5, and Figure 3.6 depict the expansion rate and pressure vs. time for slow, moderate, and rapid pressurization, respectively. According to the graph, faster pressurization leads to lower expansion and a faster transition to solvent and supercritical carbon dioxide. Because faster pressurization results in faster supercritical carbon dioxide intake than slower pressurization.

3.3.2 Temperature parameter

Figure 3.7 depicts a video camera image of NMP at various experiment temperatures. First, $scCO_2$ dissolves into the solvent and expands it; at this point, the black and gray phases described in Section 3.3.1 occur. Then, $scCO_2$ and NMP become homogeneous. Figure 3.6, Figure 3.8, and Figure 3.9 depict NMP expansion vs. time graphs at 40, 60, and 80 °C. The graphs illustrate that for NMP and $scCO_2$, reaching the homogeneous phase takes longer at higher temperatures. However, the expansion does not change significantly, even at greater temperatures, where it occurs gradually over time. This event could happen because, at higher temperatures, $scCO_2$ density decreases dramatically [1], and a low density reduces $scCO_2$'s capacity to dissolve into NMP and makes it take longer to have NMP saturated with $scCO_2$ [2].

Figure 3.10 presents images of ethanol and $scCO_2$ at various temperatures. Supercritical CO_2 dissolves into ethanol and expands until $scCO_2$ and ethanol become homogeneous, similar to NMP case. Figure 3.11, Figure 3.12, and Figure 3.13 show graphs of ethanol expansion and pressure rising versus time at 40, 60, and 80 °C. The duration to establish a homogeneous phase does not change considerably in this graph. However, the expansion of ethanol decreases dramatically as temperature rises.

Figure 3.14 provides images of acetone and $scCO_2$ at various temperatures. The process for achieving a homogeneous phase is identical to that of NMP and ethanol. Figure 3.15, Figure 3.16, and Figure 3.17 show graphs of acetone expansion rate and pressure growth vs. time at 40, 60, and 80 °C. For ethanol and acetone cases, the duration to achieve a homogeneous phase does not dramatically change with temperature, although the expansion rate drops. However, this phenomenon did not happen in NMP because the vapor pressure of NMP is not significantly change, considerably when the temperature rises.

On the other hand, the vapor pressure of ethanol and acetone varies substantially with temperature. At higher temperatures, the vapor pressure of ethanol and acetone increases dramatically. As a result, more ethanol and acetone are evaporated and transferred into the CO_2 phase, reducing solvent expansion. Table 3.2 shows the vapor pressures of NMP, ethanol, and acetone at 40, 60, and 80 °C as derived using the Antoine equation (Equation 3.1), with A, B, and C values from the literature [3-5].

$$log\ P = A - \frac{B}{C + T} \qquad \text{(Equation 3.1)}$$

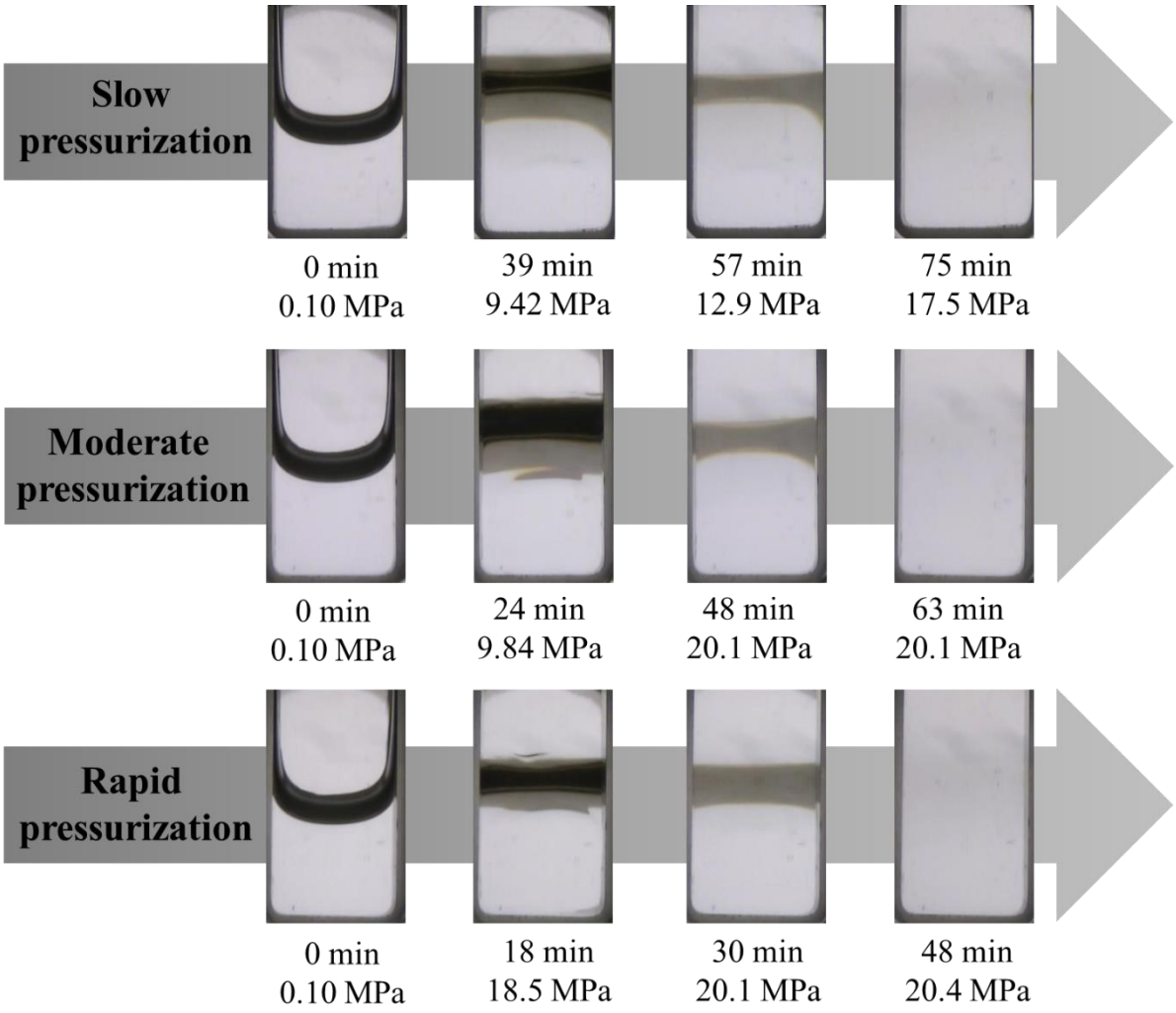

Figure 3.3 Time-lapse images for CO_2 and NMP at different pressurization rates from the beginning of the experiment until the homogenous phase was formed

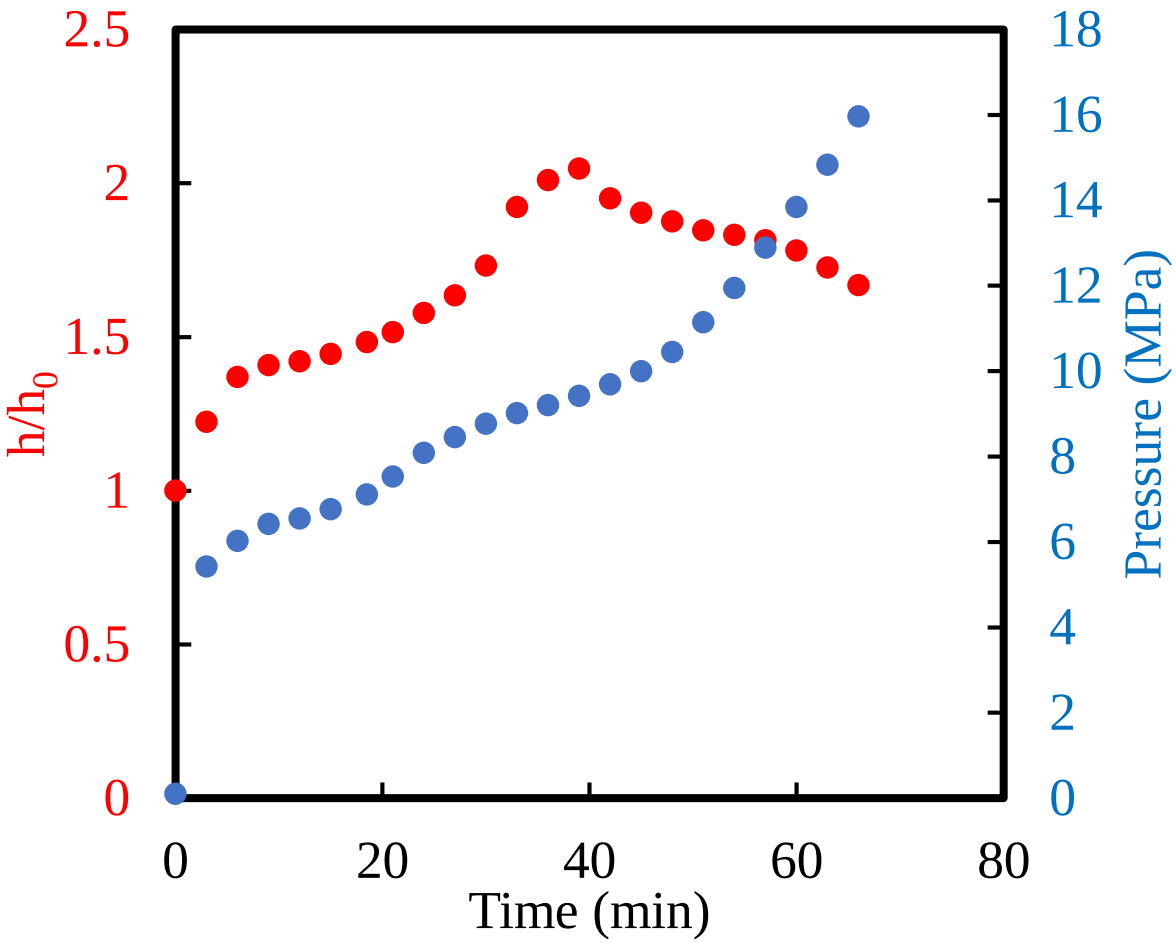

Figure 3.4 expansion rate (red) and pressure (blue) against time for slow pressurization (0.234 MPa·min^{-1})

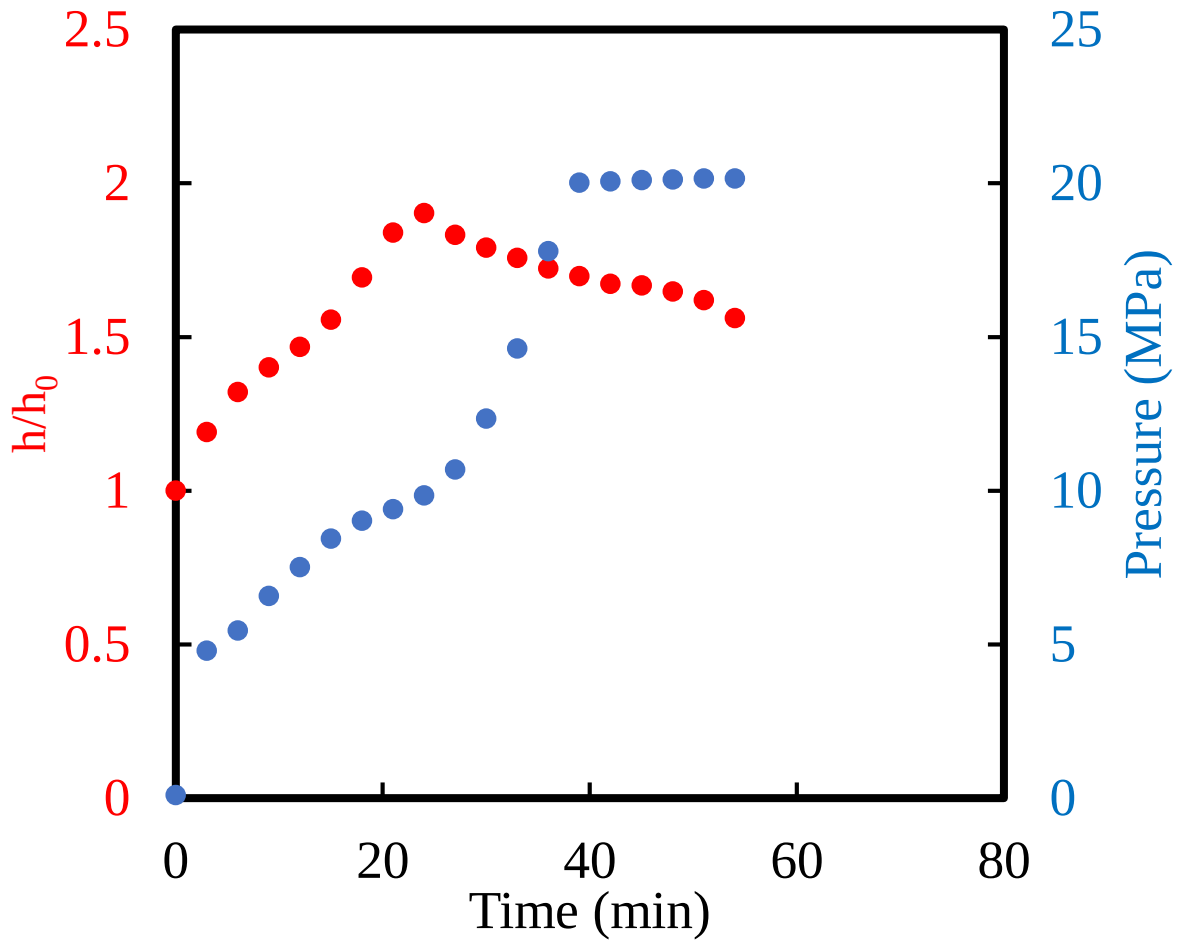

Figure 3.5 NMP expansion rate (red) and pressure (blue) against time for moderate pressurization (0.513 MPa·min^{-1})

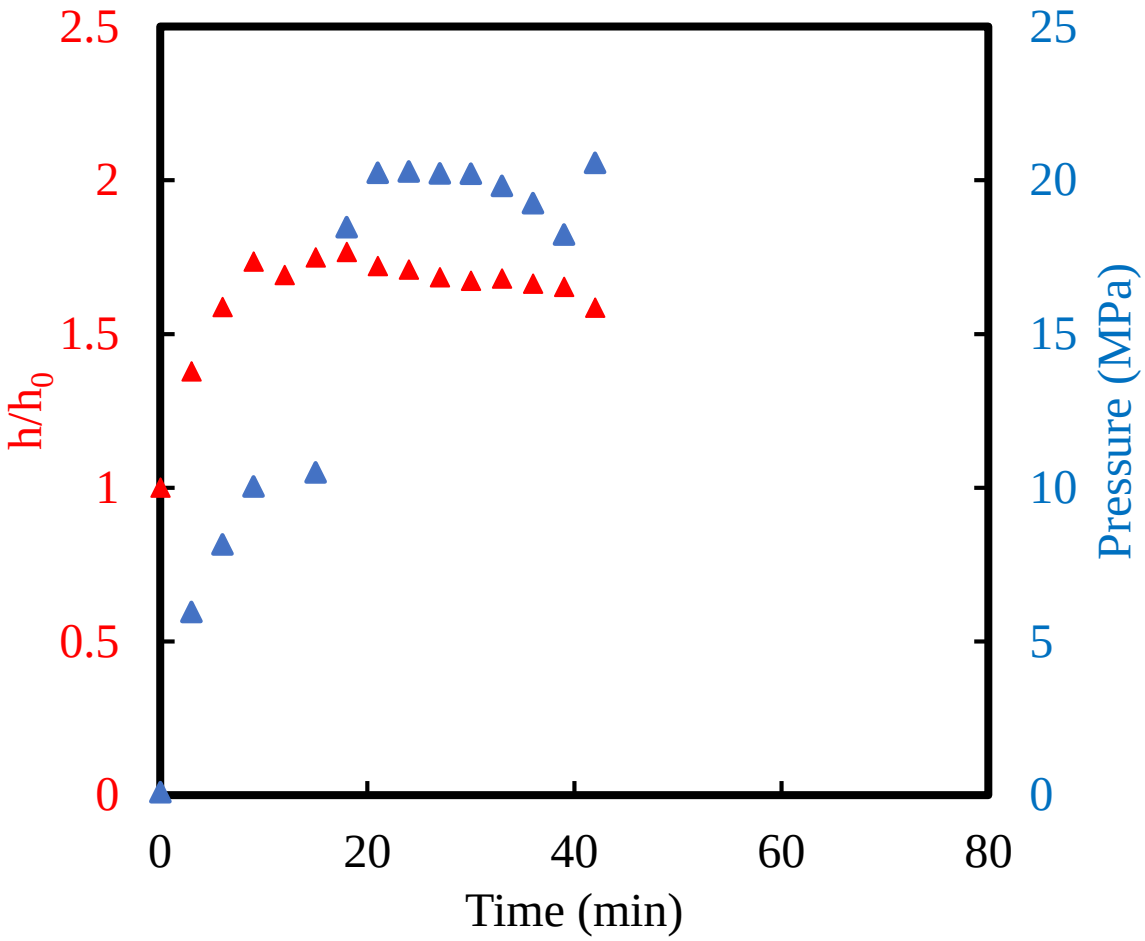

Figure 3.6 NMP expansion rate (red) and pressure (blue) against time for slow pressurization (0.964 MPa·min^{-1})

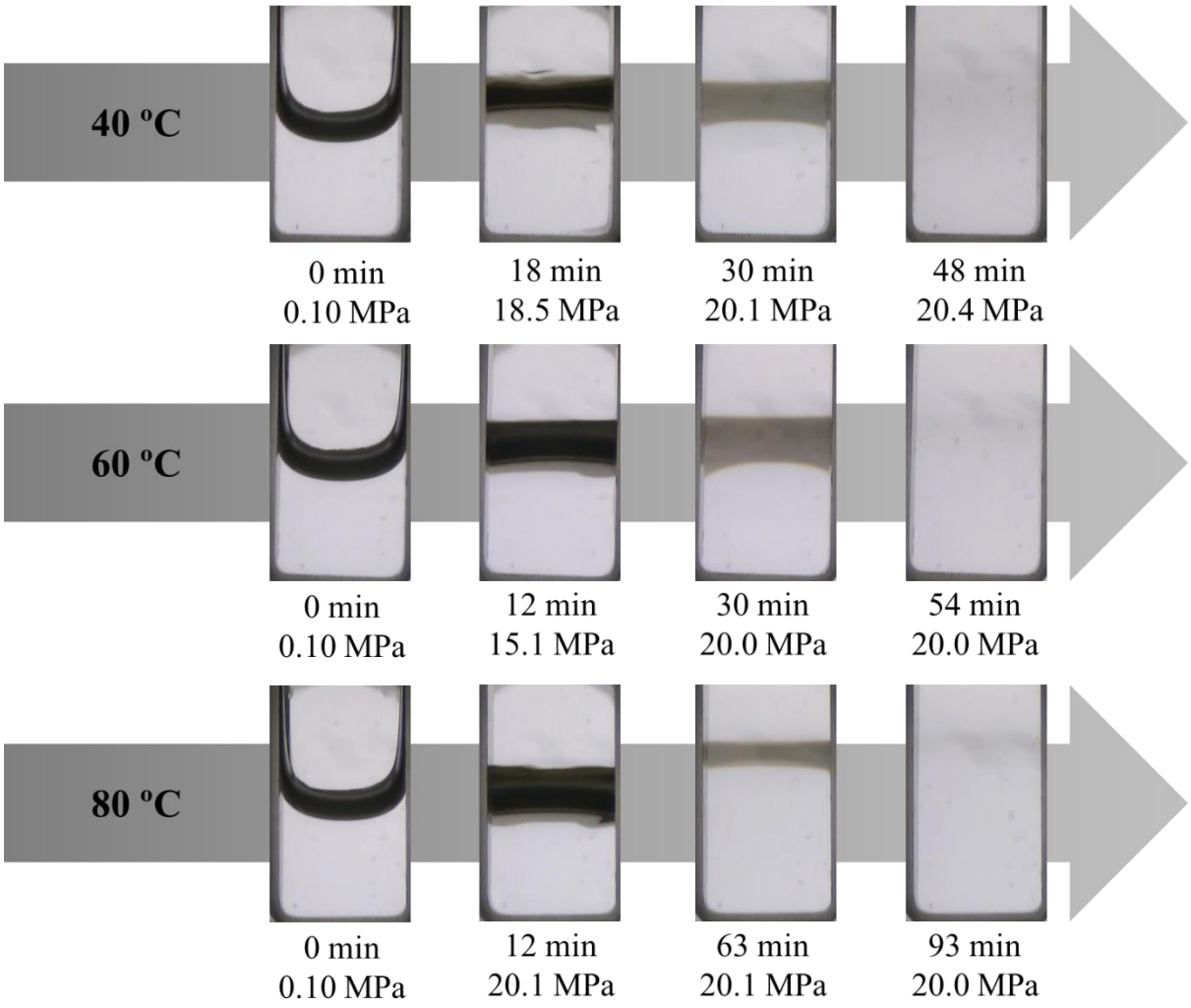

Figure 3.7 Time-lapse images for CO_2 and NMP at different temperatures of 40, 60, and 80 °C from the beginning of the experiment until the homogenous phase was formed

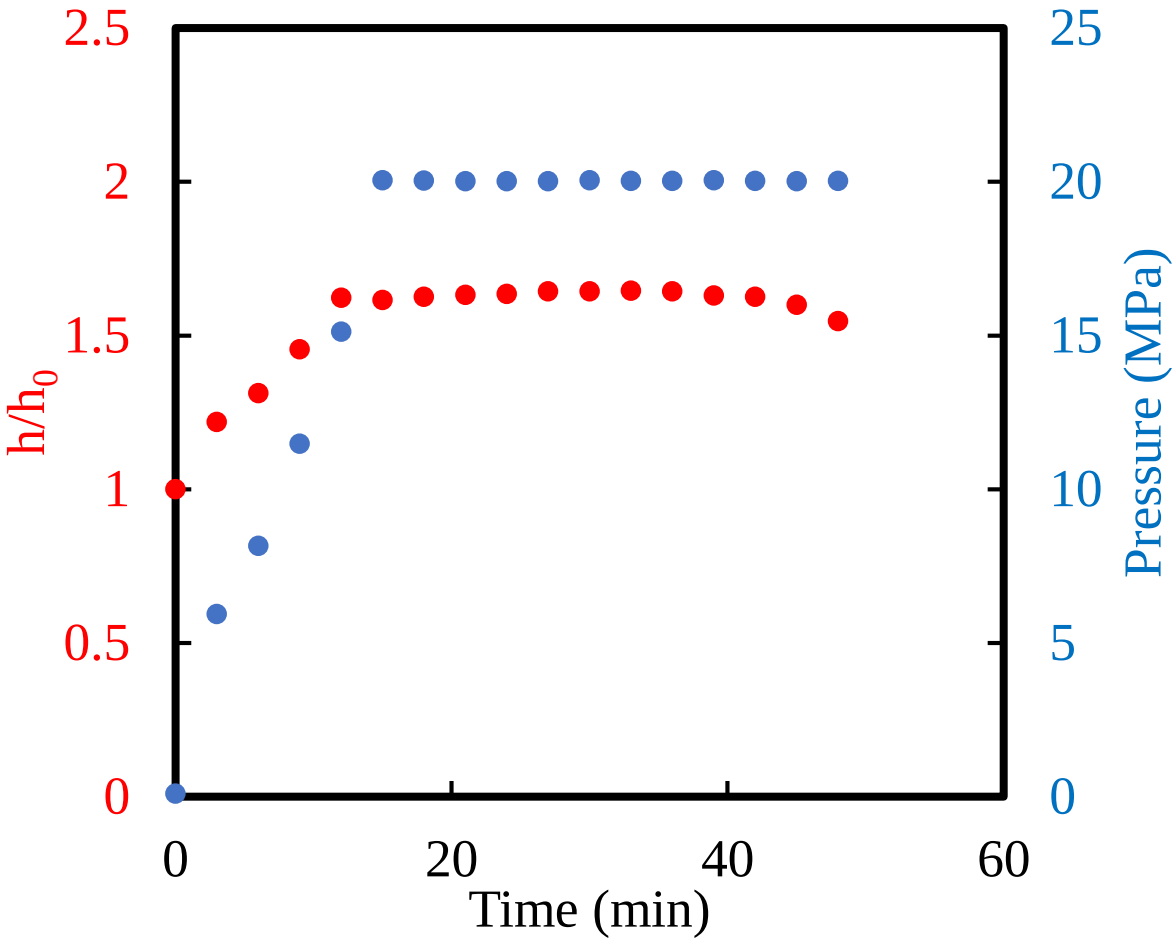

Figure 3.8 NMP expansion rate (red) and pressure (blue) against time at 60 ºC

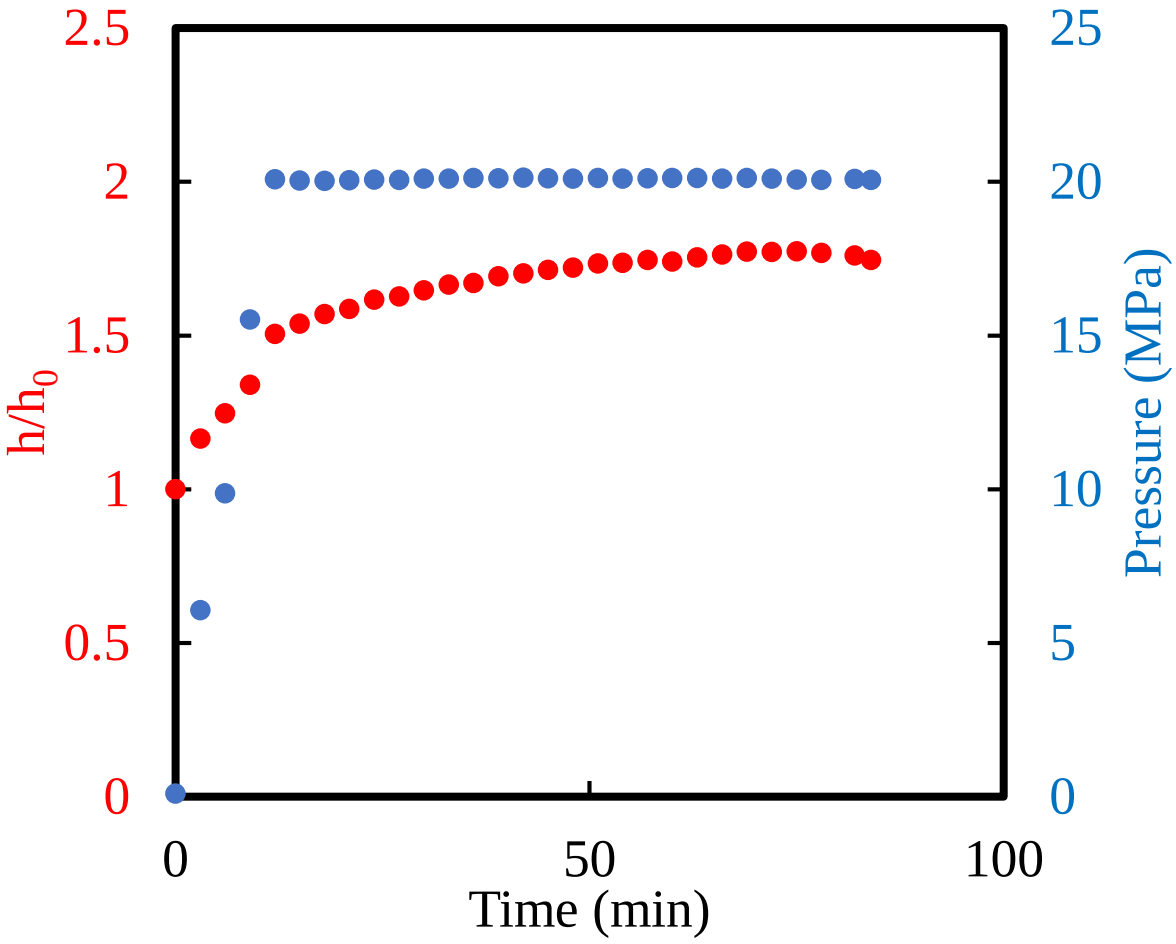

Figure 3.9 NMP expansion rate (red) and pressure (blue) against time at 80 ºC

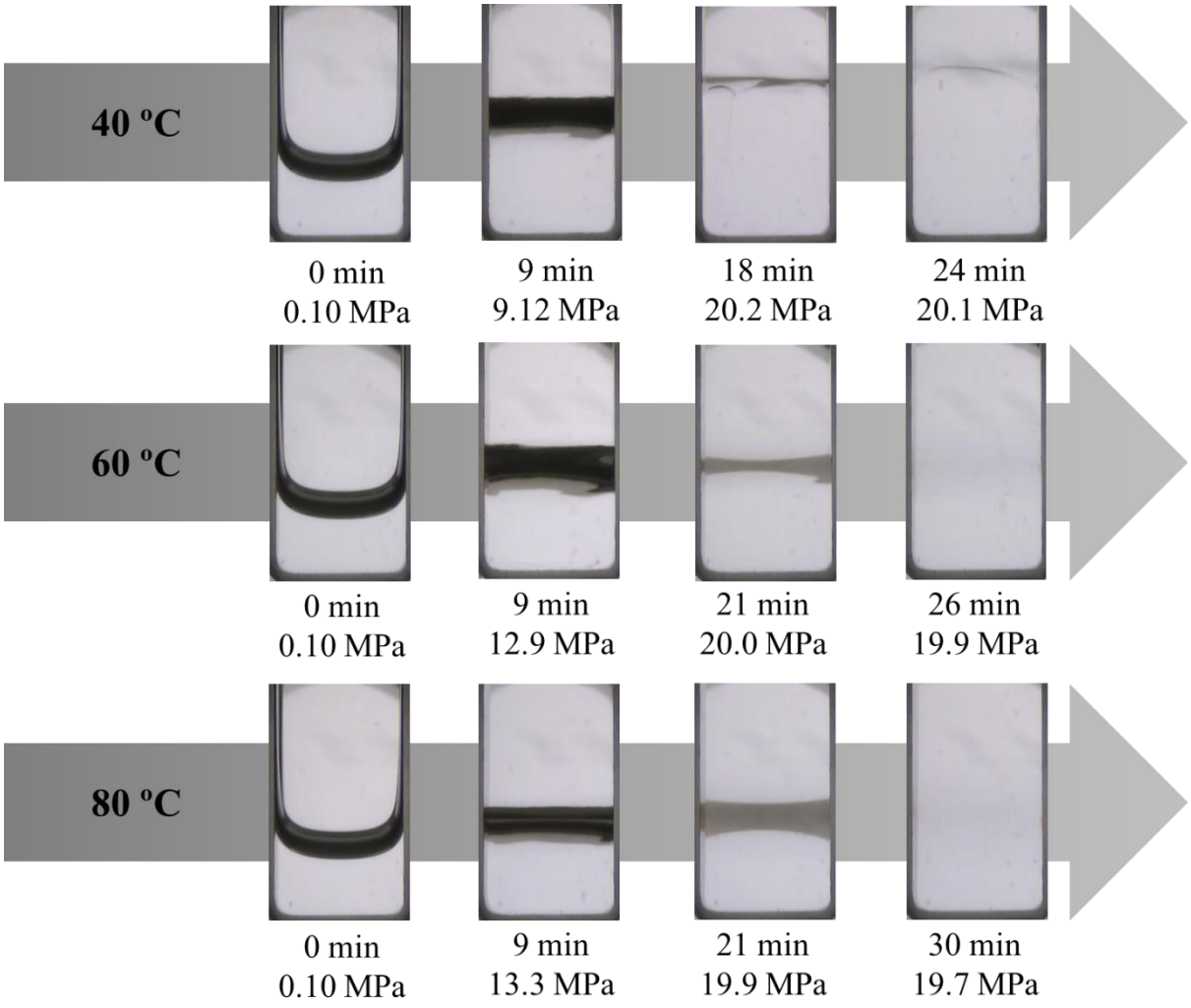

Figure 3.10 Time-lapse images for CO_2 and ethanol at different temperatures of 40, 60, and 80 ºC from the beginning of the experiment until the homogenous phase was formed

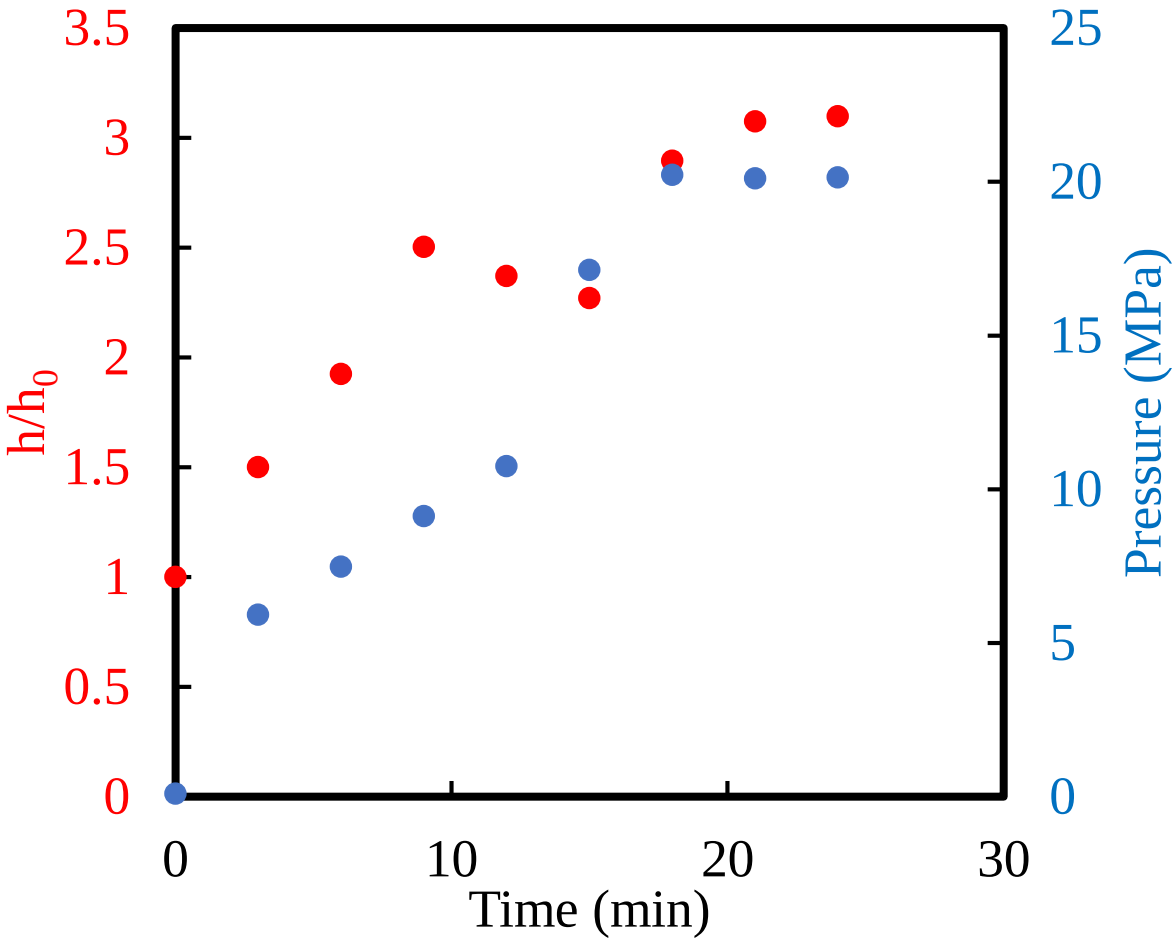

Figure 3.11 Ethanol expansion rate (red) and pressure (blue) against time at 40 ºC

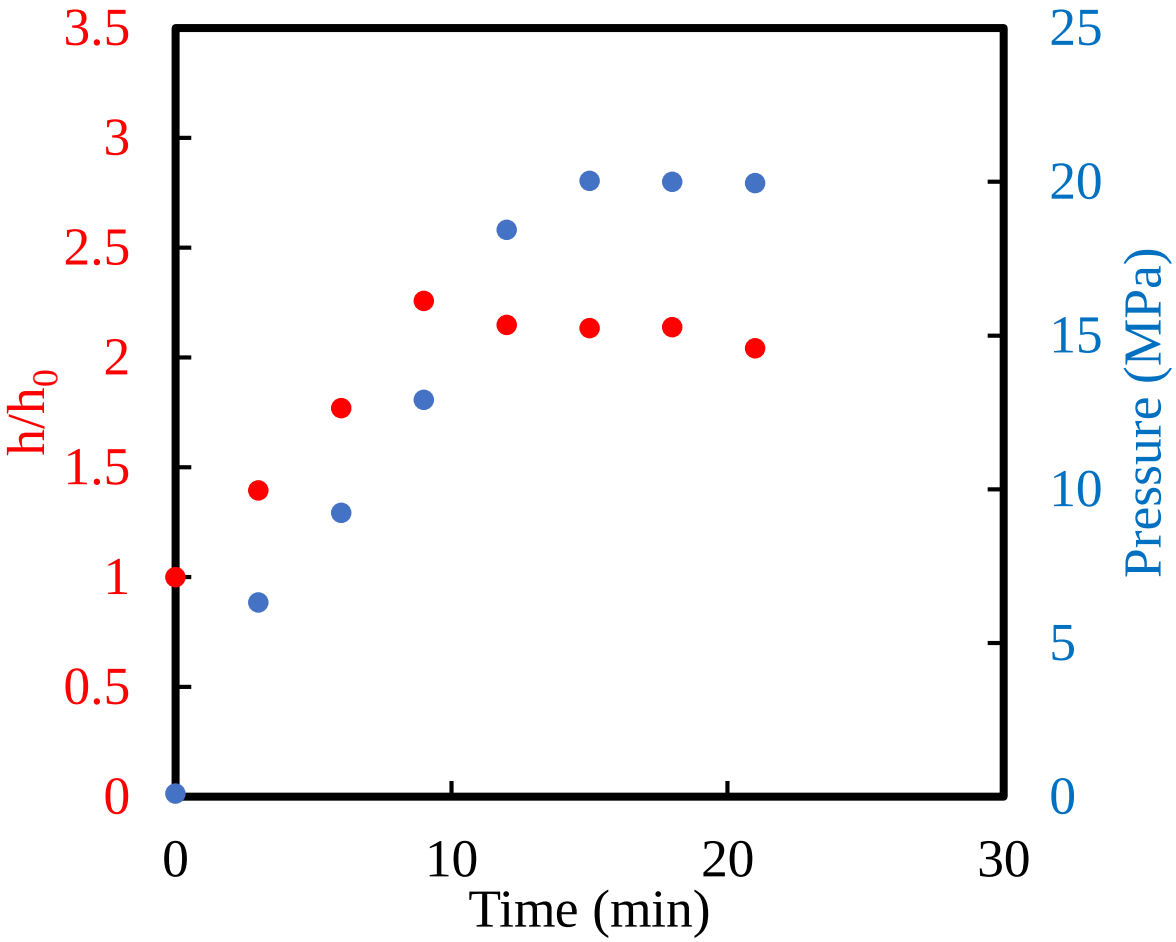

Figure 3.12 Ethanol expansion rate (red) and pressure (blue) against time at 60 ºC

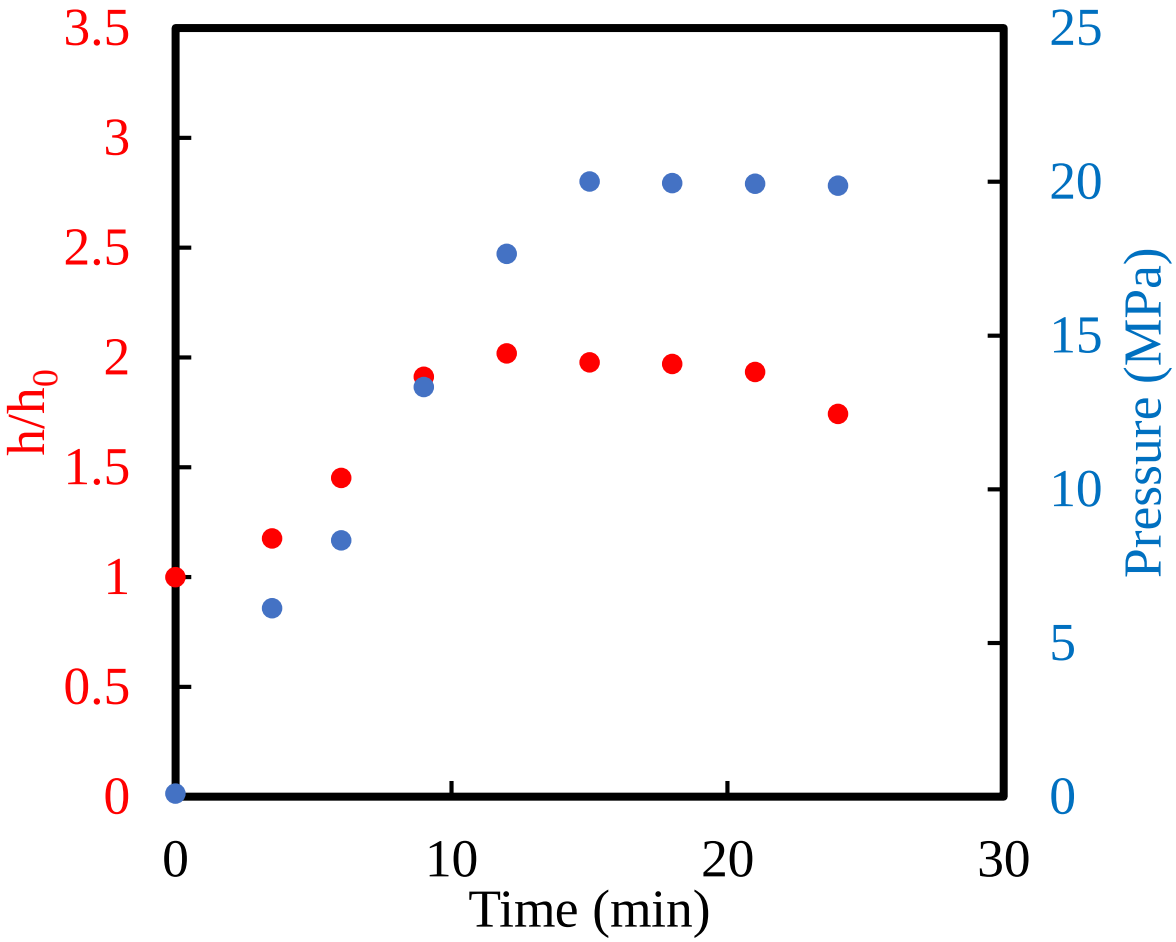

Figure 3.13 Ethanol expansion rate (red) and pressure (blue) against time at 80 ºC

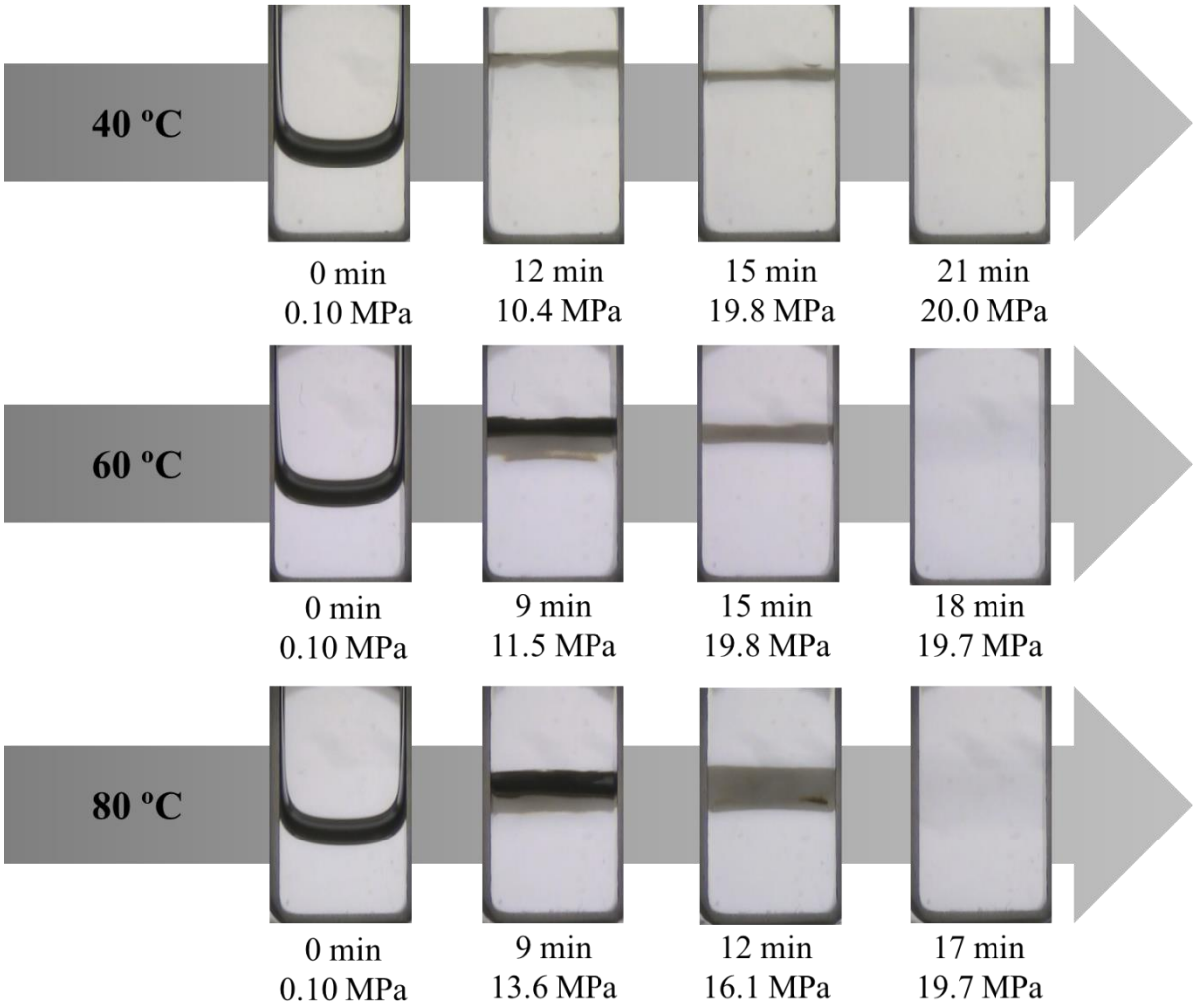

Figure 3.14 Time-lapse images for CO_2 and acetone at different temperatures of 40, 60, and 80 ºC from the beginning of the experiment until the homogenous phase was formed

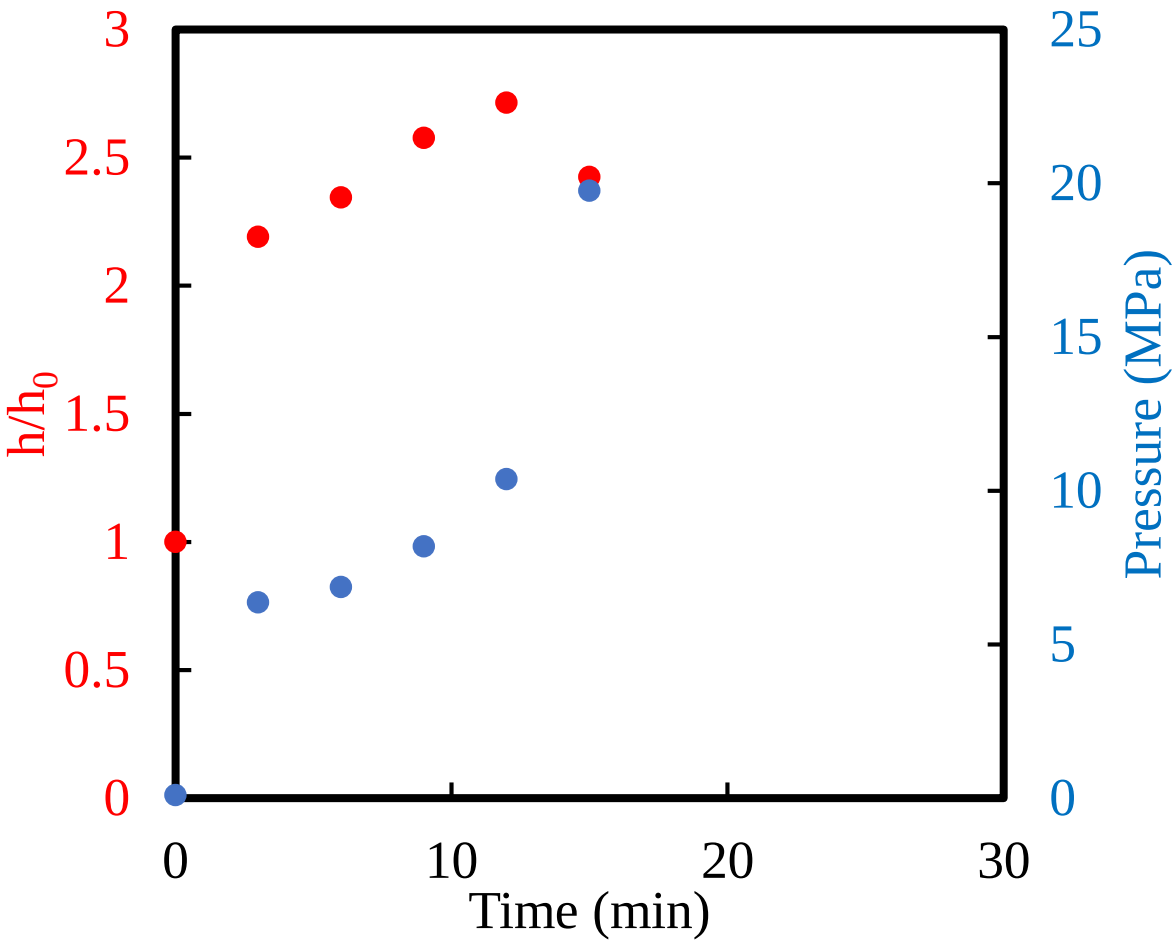

Figure 3.15 Acetone expansion rate (red) and pressure (blue) against time at 40 ºC

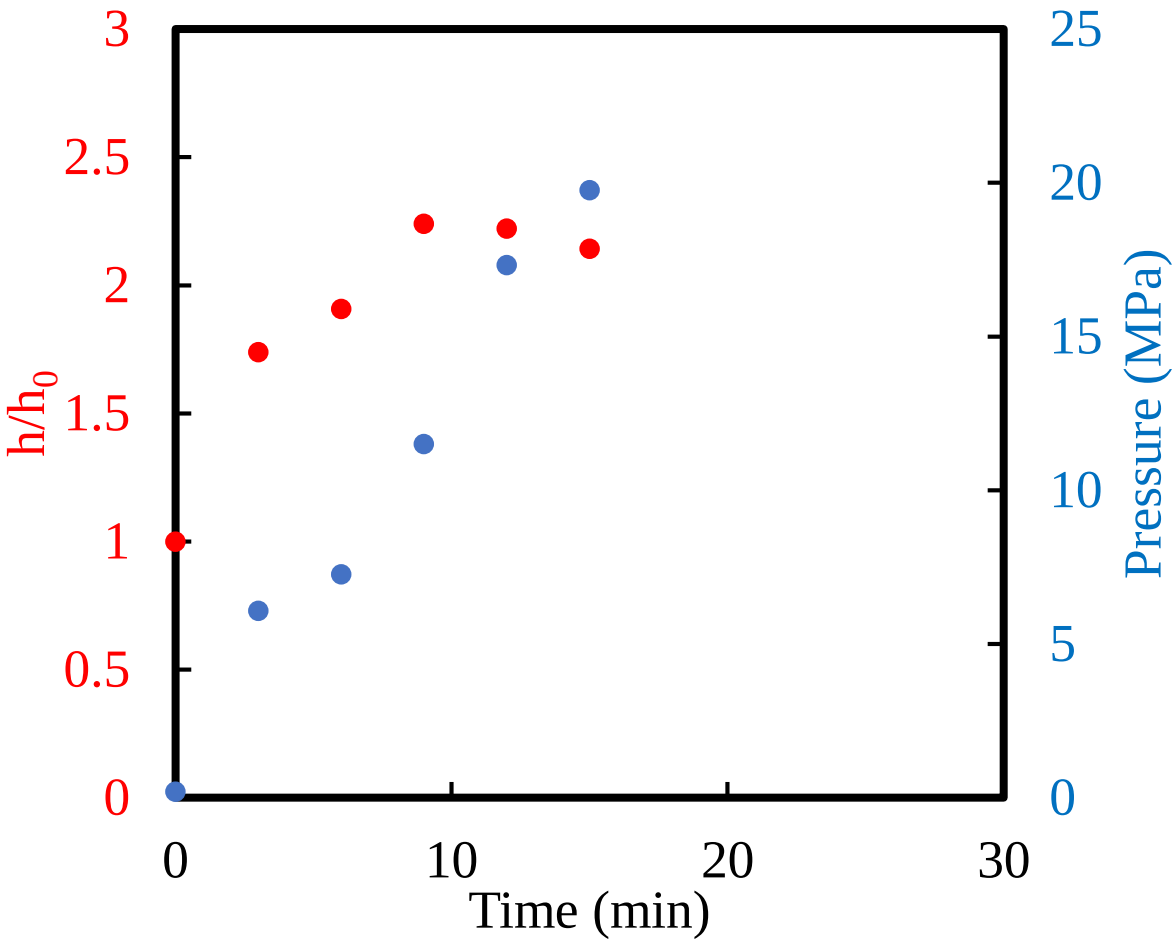

Figure 3.16 Acetone expansion rate (red) and pressure (blue) against time at 60 ºC

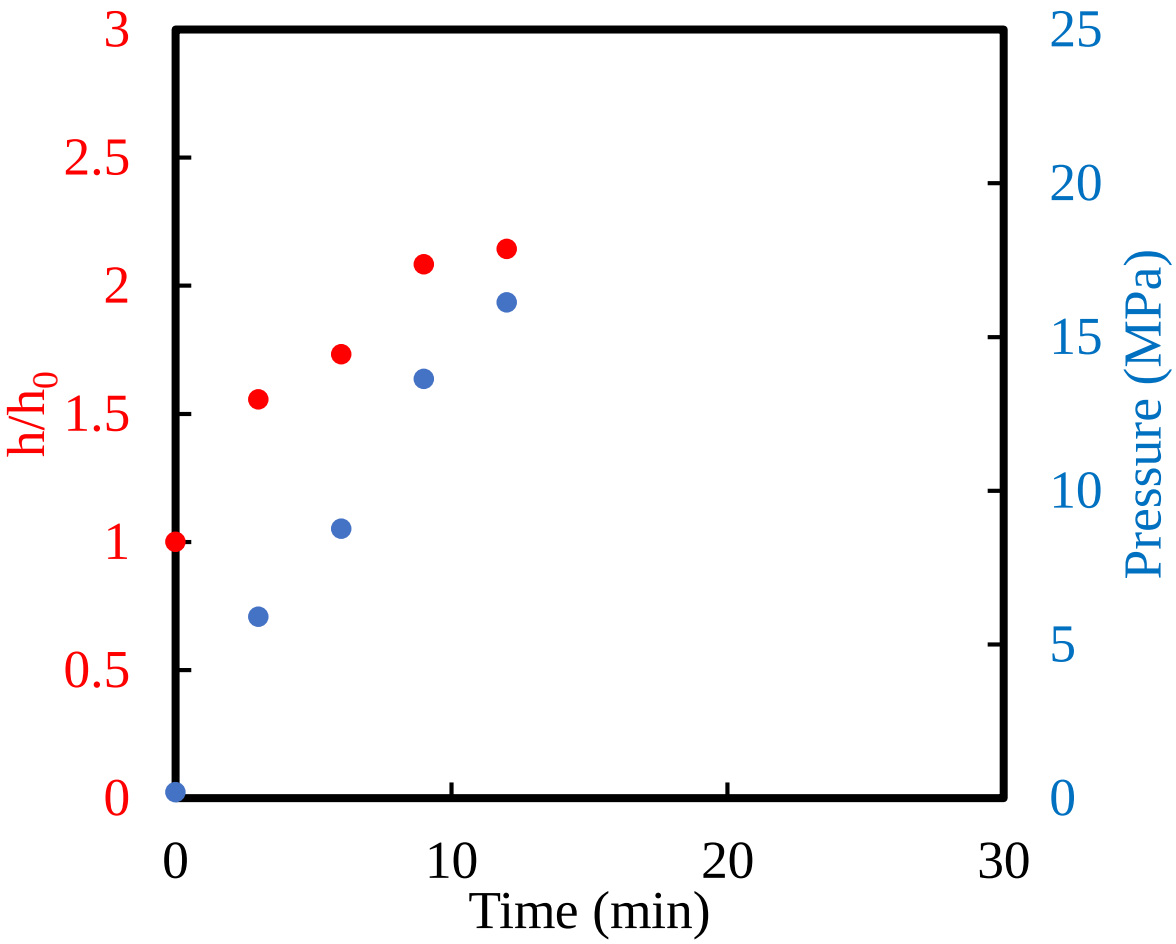

Figure 3.17 Acetone expansion rate (red) and pressure (blue) against time at 80 ºC

Table 3.2 Vapor pressures of NMP, ethanol, and acetone at 40, 60, and 80 ºC

Solvent	Vapor pressure (kPa) at		
	40 ºC	60 ºC	80 ºC
NMP	0.13	0.46	1.34
Ethanol	18.15	47.52	109.76
Acetone	56.93	114.96	215.13

3.3.3 Solvent type parameter

Figure 3.18 depicts images for various solvents and CO_2 from the start of the experiment until a homogeneous phase was established. The steps for reaching the homogeneous phase are similar to the process described in the previous section.

Figure 3.19, Figure 3.20, Figure 3.21, Figure 3.22, Figure 3.23,and Figure 3.24 show plots of the solvent expansion rate and pressure growth against time for NMP, acetone, 1-butanol, ethanol, DMSO, and o-xylene, respectively. According to these graphs, the time required to establish a homogeneous phase varies depending on the solvent. Acetone is the fastest, followed by ethanol, 1-butanol, o-xylene, NMP, and finally, DMSO, where this phenomenon is related to the vapor pressure value. A high vapor pressure causes a faster formation of a homogeneous phase. These solvents' expansion rates vary as well. Acetone, ethanol, 1-butanol, DMSO, NMP, and o-xylene have the highest expansion rates from largest to smallest.

The expansion rate of solvents from the beginning until the end of the experiment can indicate that mass transfer happens between $scCO_2$ and organic solvents. In the first stage of the experiment when the pressure starts increasing, the solvent expands which indicates that CO_2 is dissolved into solvents. While in the end of the stage before solvents and CO_2 become homogenous phase, expansion rate of solvents decreases. This phenomenon indicates that solvents also moves to CO_2 phase.

For the end of stage which indicates solvent movement to CO_2 can be explained by vapor pressure because solvent with higher vapor pressure shows more expansion rate decrease. Then when estimating the relationship between maximum expansion rate with vapor pressure p^0 (kPa), an inverse relationship can be estimated as follows.

$$\frac{h^{max}}{h_0} \propto \frac{1}{p^0} \qquad \text{(Equation 3.2)}$$

Where the highest to lowest vapor pressure shown in Table 3.3 is as follows: NMP < DMSO < o-xylene < 1-buthanol < ethanol < acetone. With only this parameter, maximum expansion rate cannot be explained. Thus, the solubility between CO_2 and organic solvent should also be taken into account. The dielectric constant (ε) is employed in this scenario. The dielectric constant indicates the polarity of a substance, and the greater the dielectric constant, the greater the polarity. Furthermore, when the polarity differences ($\Delta\varepsilon$) between two substances are lower, their solubility increases, and higher CO_2 solubility in solvent equals to a higher solvent expansion rate. This relationship is shown below.

$$\frac{h^{max}}{h_0} \propto \frac{1}{\Delta\varepsilon} \quad \text{(Equation 3.3)}$$

The dielectric constants (ε) for each solvent shown in Table 3.3 [6-9]. Then, Figure 3.25 shows the estimated relationship between vapor pressure and dielectric constant difference of solvents with maximum expansion rate where the estimated relationship equation is as follows.

$$\left(\frac{h^{max}}{h_0}\right) = 1.9386\left(\frac{1}{p^0\Delta\varepsilon}\right)^{-0.09} \quad \text{(Equation 3.4)}$$

Where, h^{max}/h_0 is maximum expansion rate, p^0 (kPa) is vapor pressure of solvent, and $\Delta\varepsilon$ is dielectric constant difference of solvent and CO_2. The R^2 for this estimation is 0.898 which is expected to be able to be improved with more data.

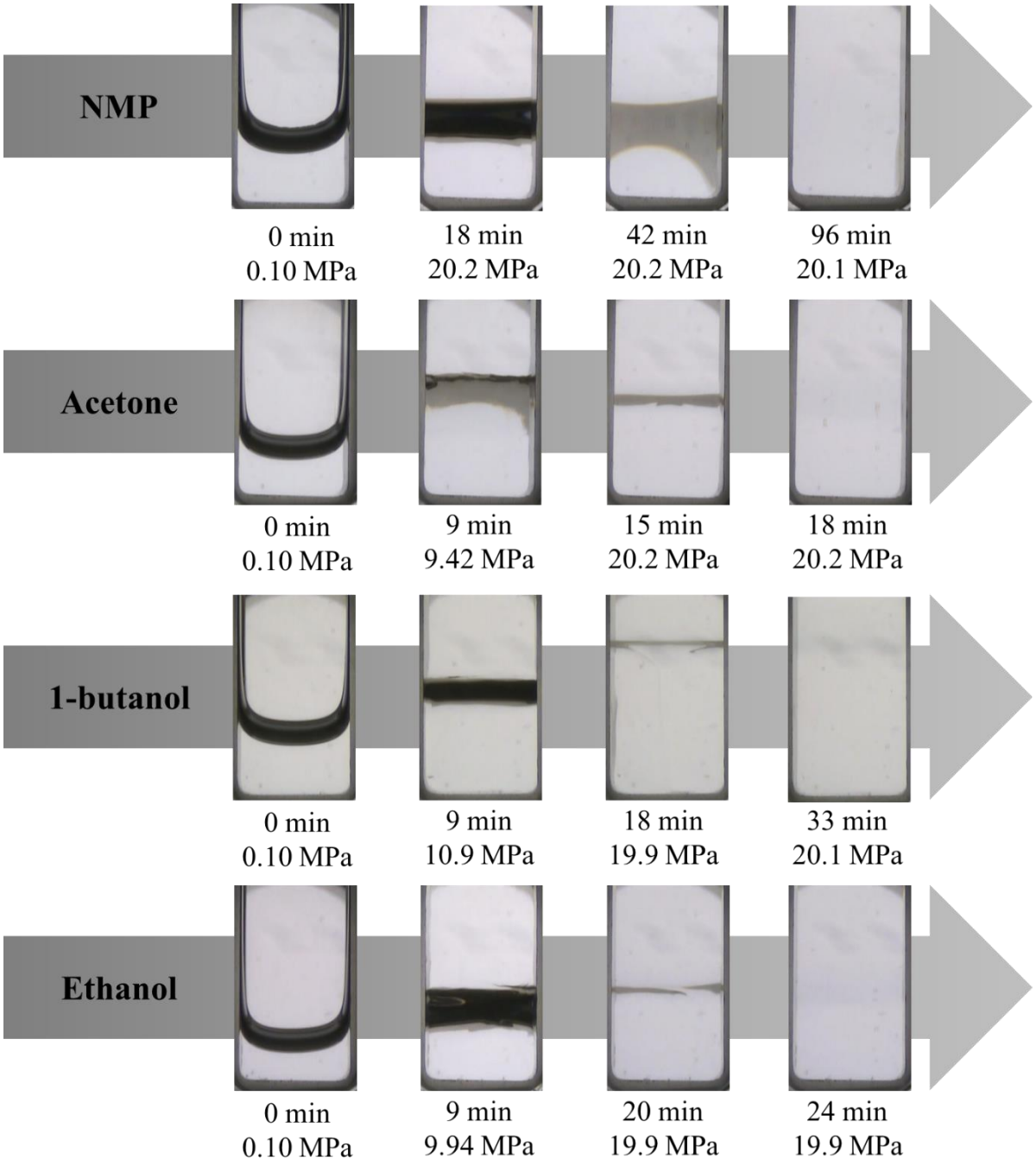

Figure 3.18 Time-lapse images for CO_2 and various solvents from the beginning of the experiment until the homogenous phase was formed

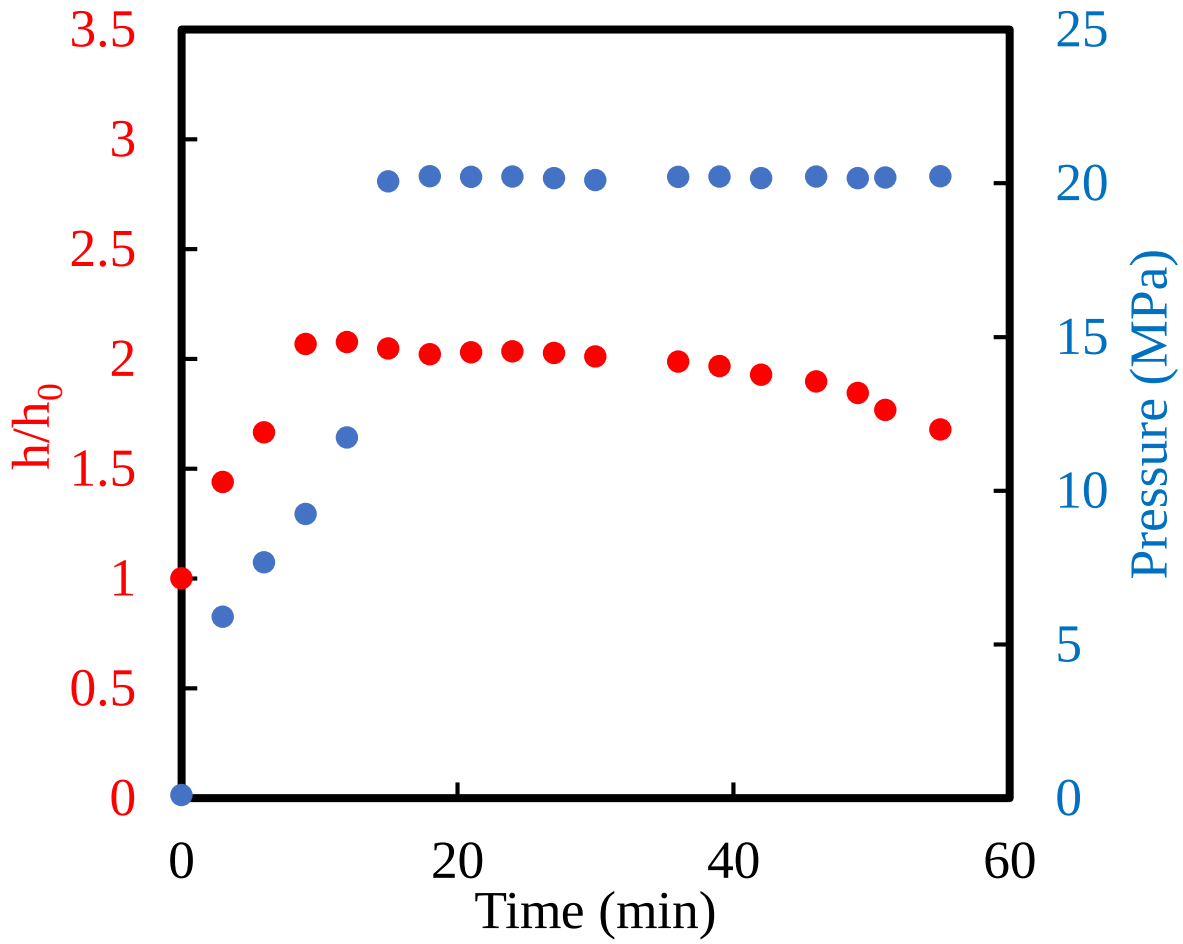

Figure 3.19 NMP expansion rate (red) and pressure (blue) against time

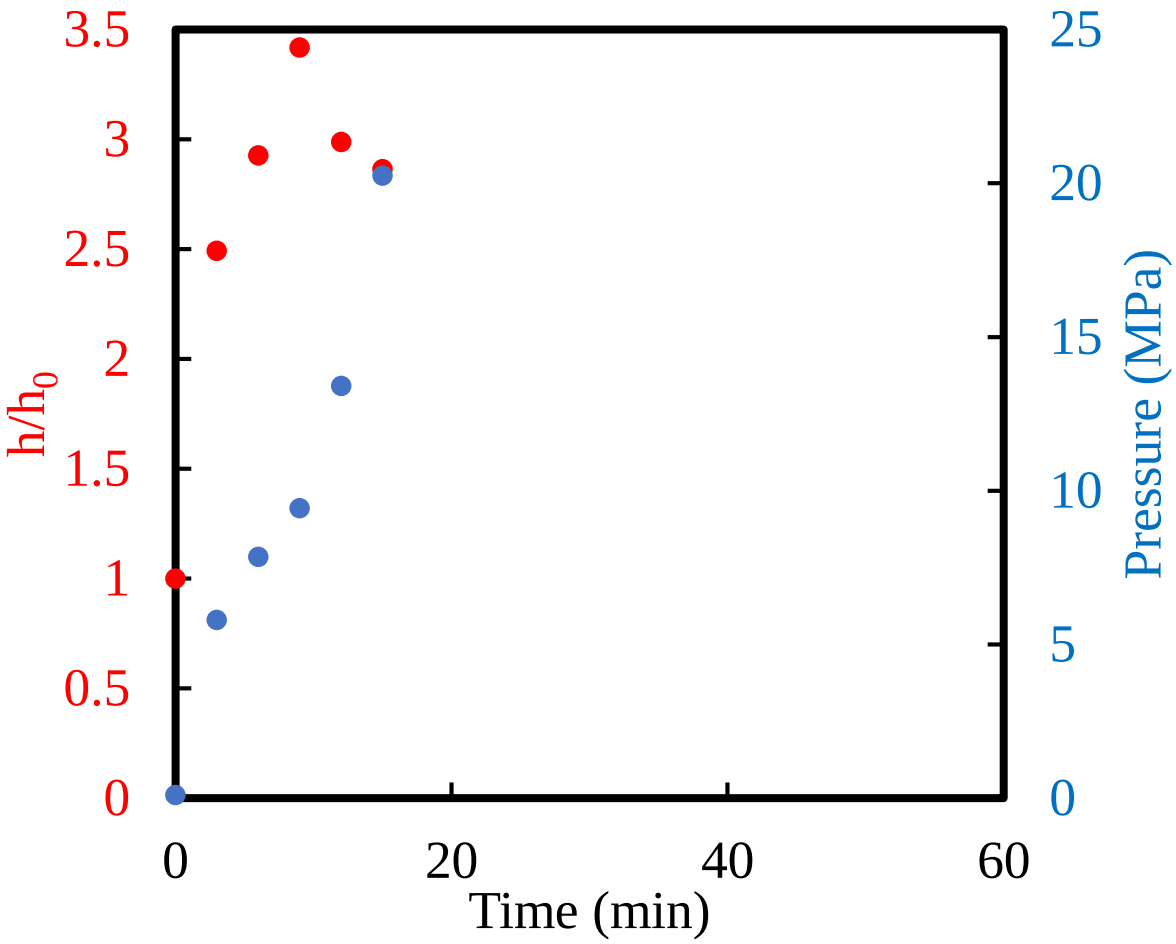

Figure 3.20 Acetone expansion rate (red) and pressure (blue) against time

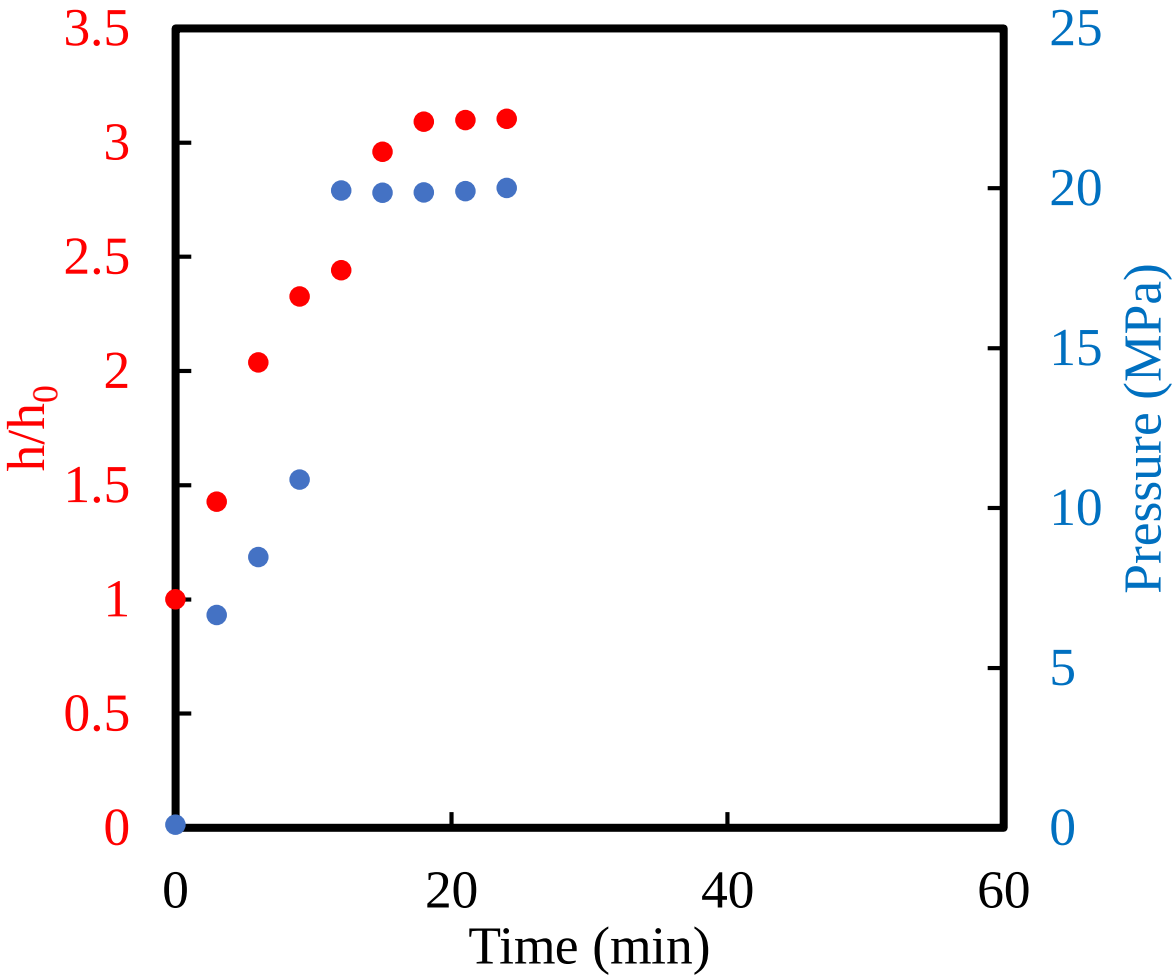

Figure 3.21 1-butanol expansion rate (red) and pressure (blue) against time

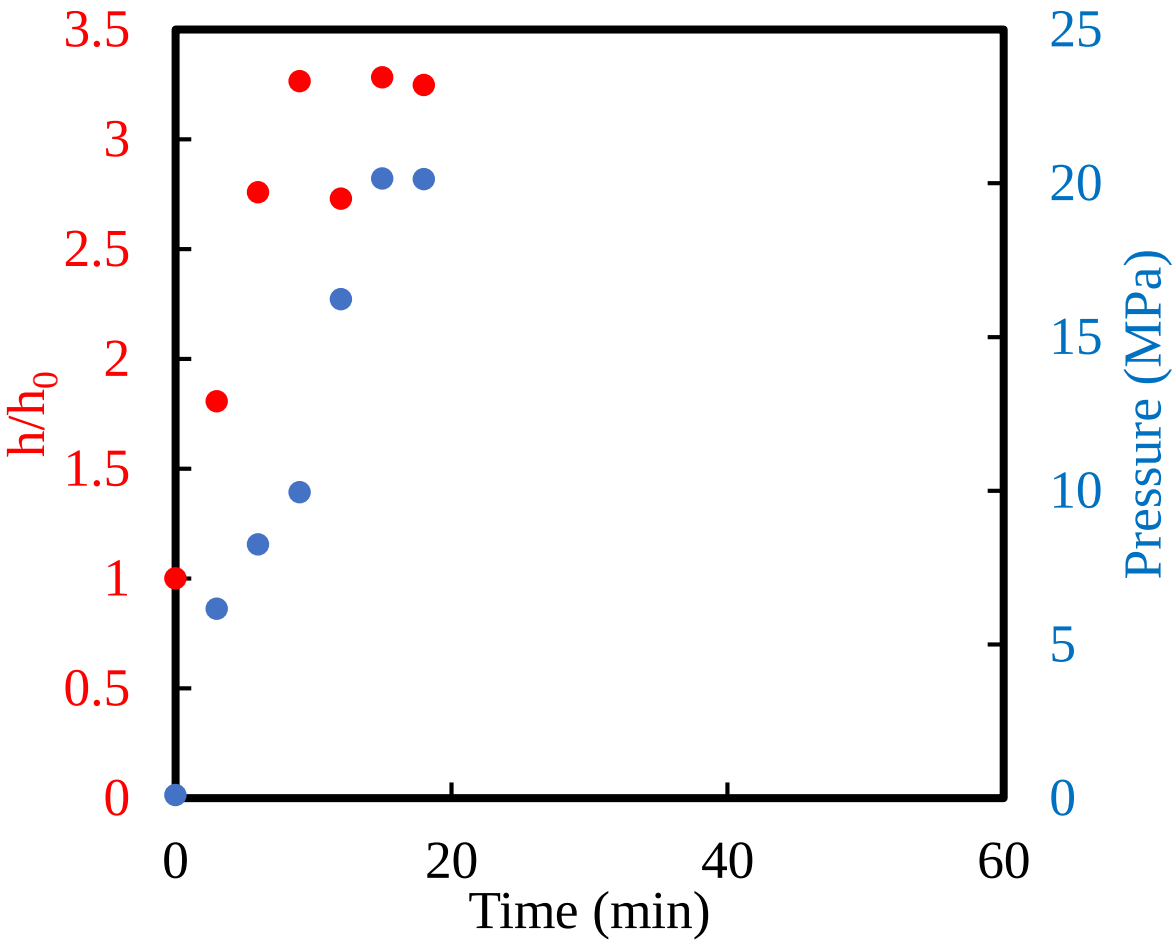

Figure 3.22 Ethanol expansion rate (red) and pressure (blue) against time

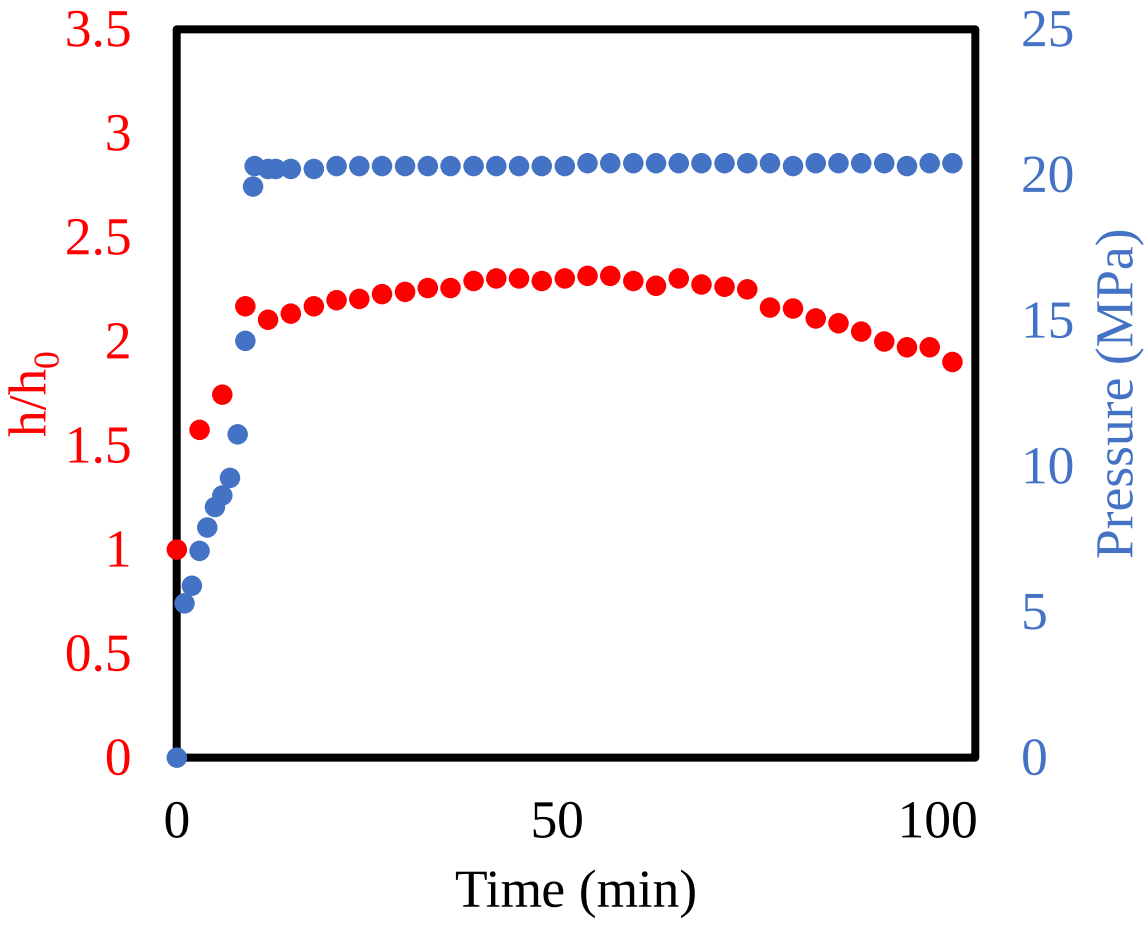

Figure 3.23 DMSO expansion rate (red) and pressure (blue) against time

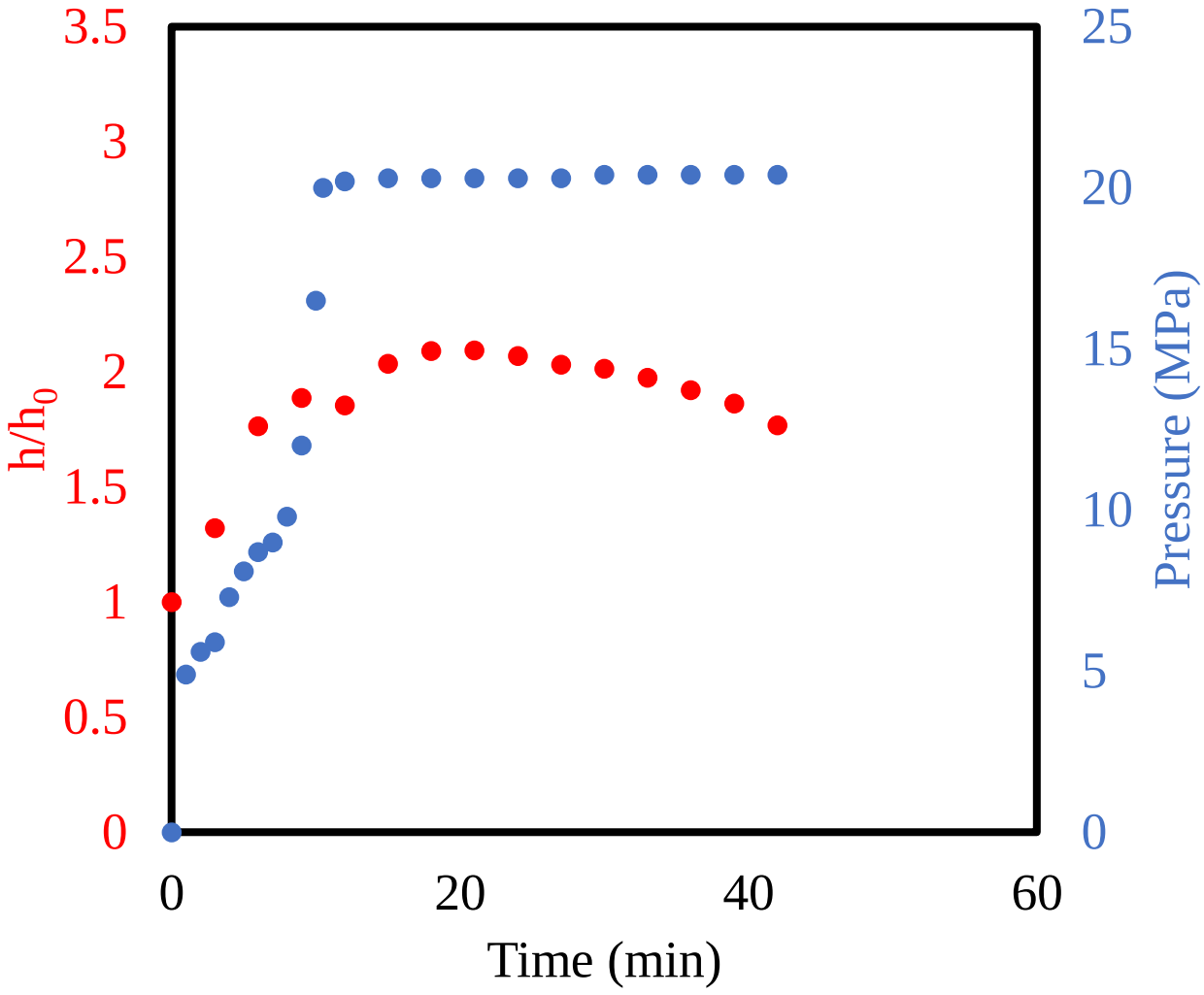

Figure 3.24 o-xylene expansion rate (red) and pressure (blue) against time

Table 3.3 Vapor pressures, dielectric constants of each compound, and maximum expansion rate

Compound	Vapor pressure p^0 (kPa) at 40 ºC	Dielectric constant ε at 40 ºC	$\Delta\varepsilon = \varepsilon - \varepsilon_{CO_2}$	$1/p^0\Delta\varepsilon$	h^{max}/h_0
Acetone	56.93	17.80	17.20	0.0010	3.42
Ethanol	18.15	22.37	20.86	0.0026	3.28
1-butanol	2.53	15.63	14.12	0.0280	3.10
NMP	0.13	28.64	27.13	0.2835	2.08
DMSO	0.22	41	39.49	0.1146	2.31
o-xylene	2.04	3	1.49	0.3288	2.09
CO_2		1.51			

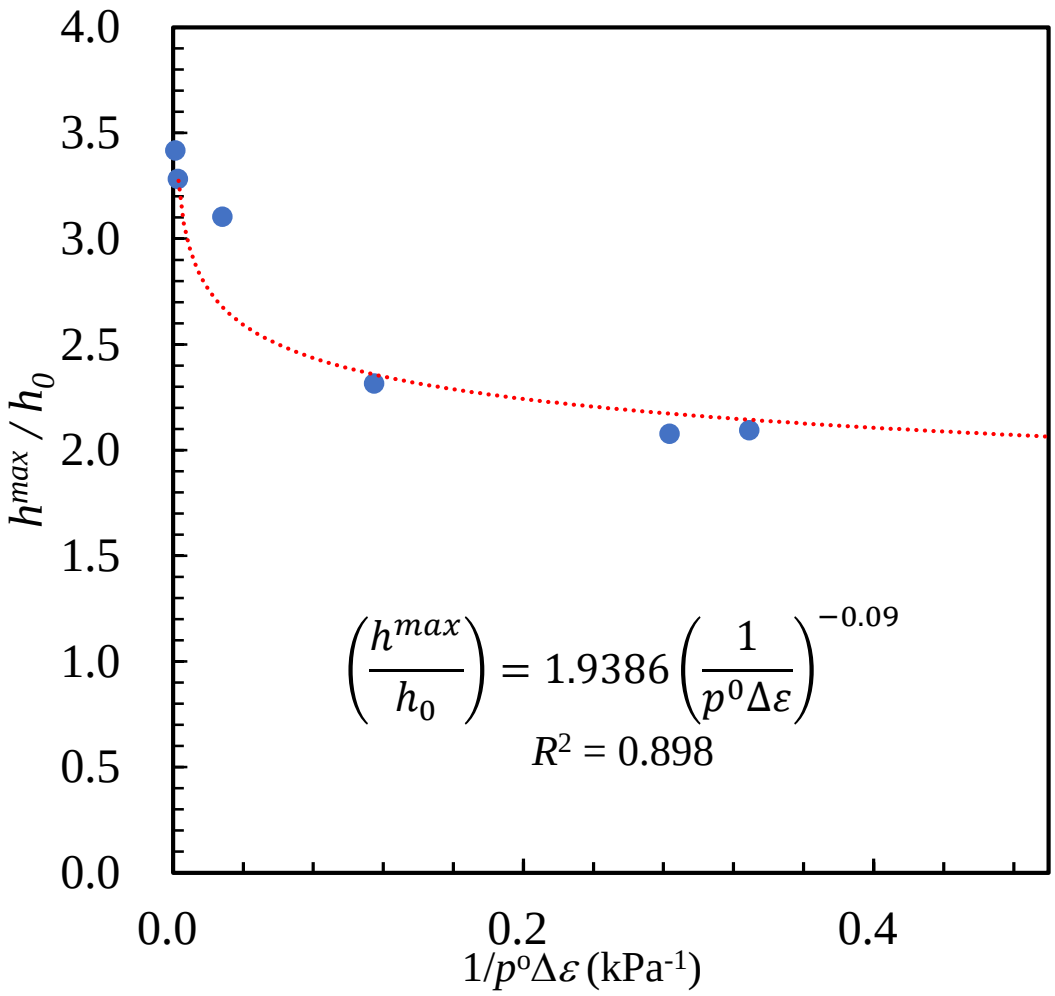

Figure 3.25 Relationship estimation between maximum expansion rate with vapor pressure (P^0) and dielectric constant ($\Delta\varepsilon$)

3.3.4 Solvent amount parameter

A video camera is used to analyze CO_2 and NMP with varying solvent concentrations, and the time-lapse photos are exhibited in Figure 3.26. The procedure for forming a homogeneous phase is the same as described in the preceding section. Figure 3.27, Figure 3.19, Figure 3.6, and Figure 3.28 show graphs of solvent expansion rate and pressure growth against time for various solvent quantities ranging from the smallest to the largest. These graphs depict the time required for each solvent amount to establish a homogeneous phase and the expansion rate. For example, at the smallest amount of solvent, CO_2 and NMP form the homogeneous phase over a more extended period, and the expansion rate is greater than the amount of solvent.

3.3.5 Flow rate parameter

Figure 3.29 depicts time-lapse photos of CO_2 and NMP from the start of the experiment until they form a homogeneous phase with varying flow rates. Regardless of flow rate, the processes to reach the homogeneous phase are the same as in the previous section. Figure 3.6, Figure 3.30, Figure 3.31, and Figure 3.32 depict the experiment results of expansion rate versus time for each sample at various flow rates. These figures show no substantial change in expansion rate or duration to form a homogeneous phase. This phenomenon occurs because a tall glass cell is utilized in this experiment, as shown in the flow picture inside the view-cell setup in Figure 3.33. Since the entrance and exit way for CO_2 is shorter than the tall glass cell, it restricts the CO_2 flow to enter the glass cell. If the container is shorter than CO_2 entrance and exit, CO_2 will transfer to solvent phase faster and affect the homogenous formation time.

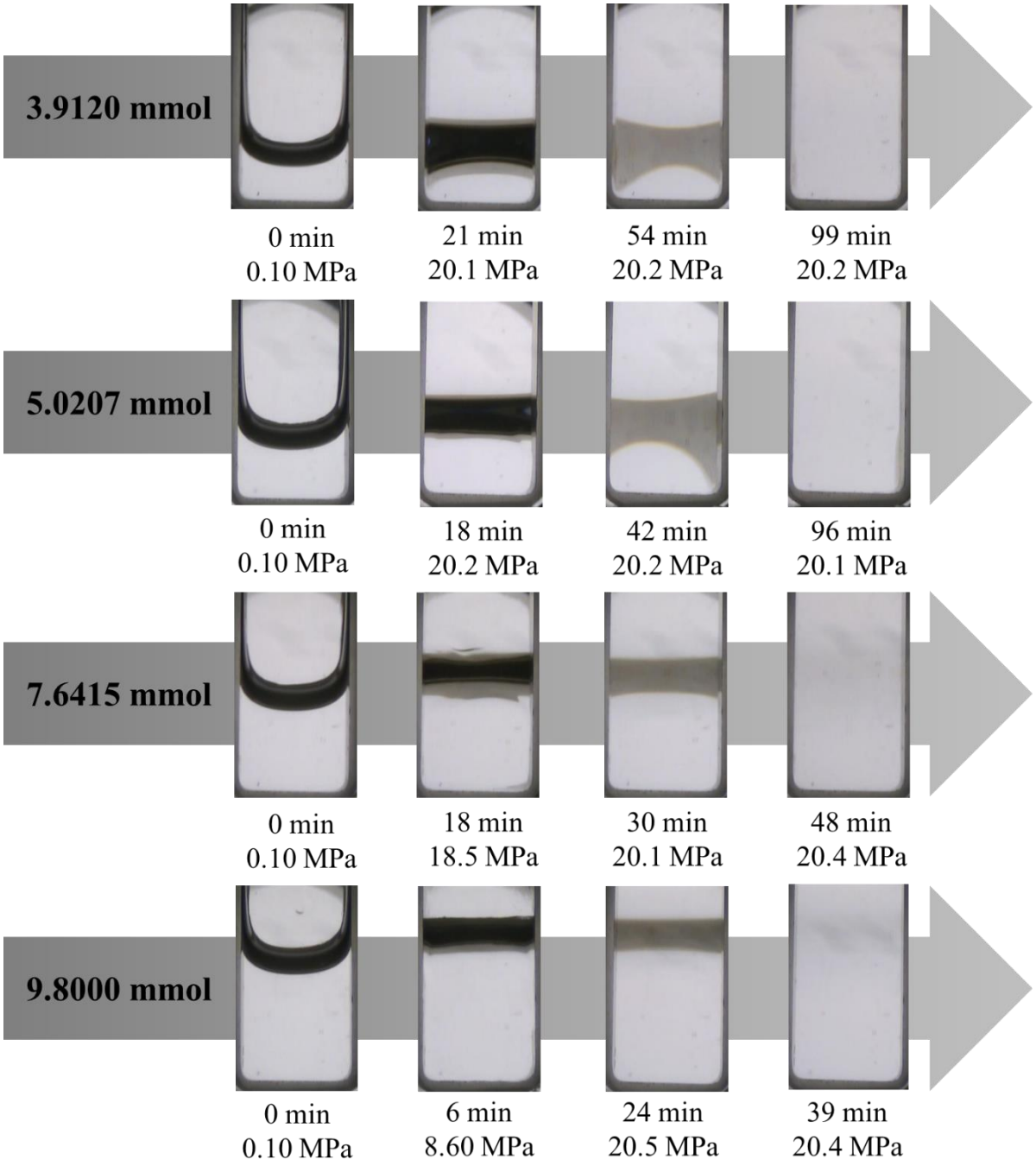

Figure 3.26 Time-lapse images for CO_2 and amount of NMP from the beginning of the experiment until the homogenous phase was formed

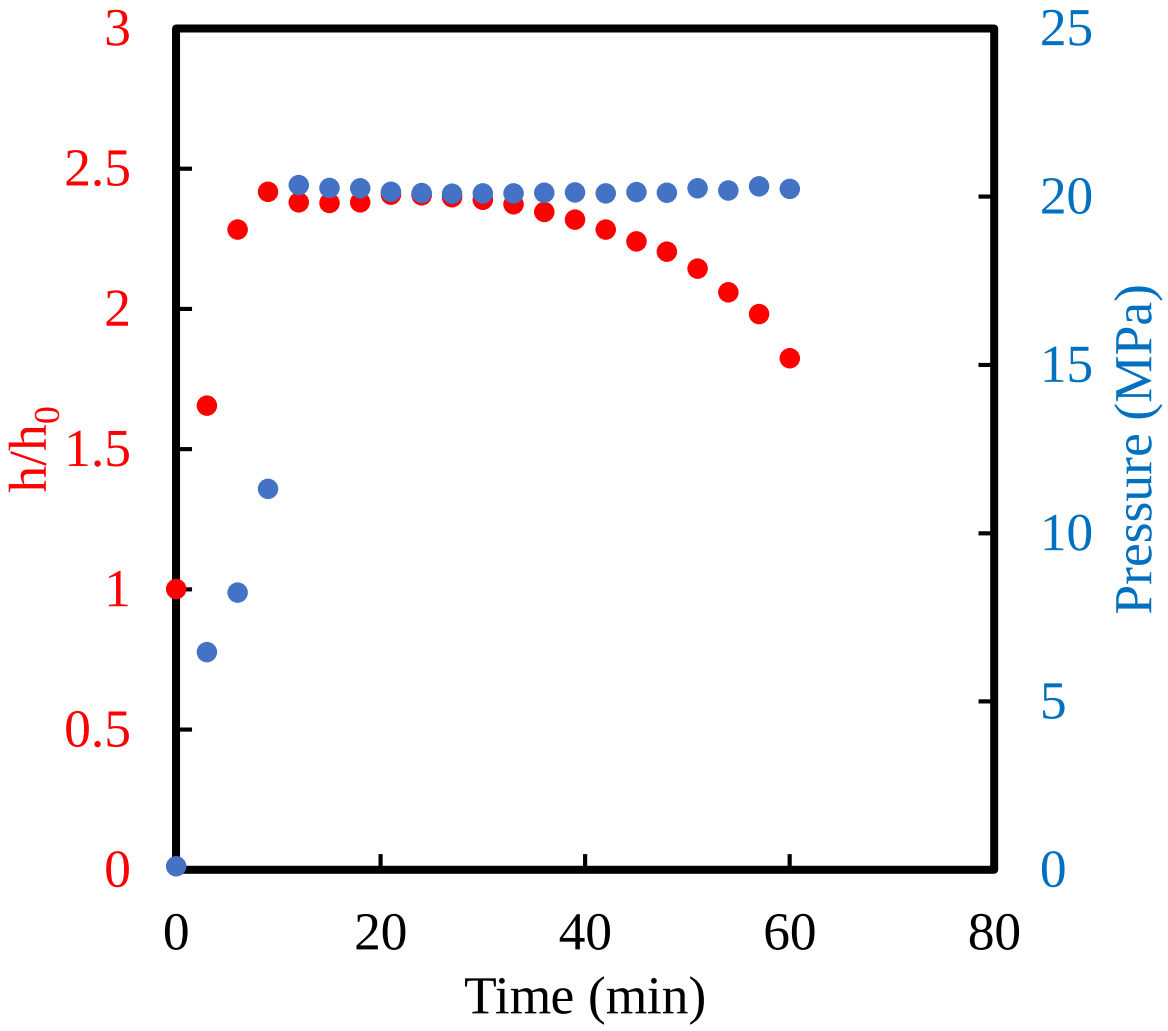

Figure 3.27 NMP expansion rate (red) and pressure (blue) against time with NMP amount of 3.9120 mmol

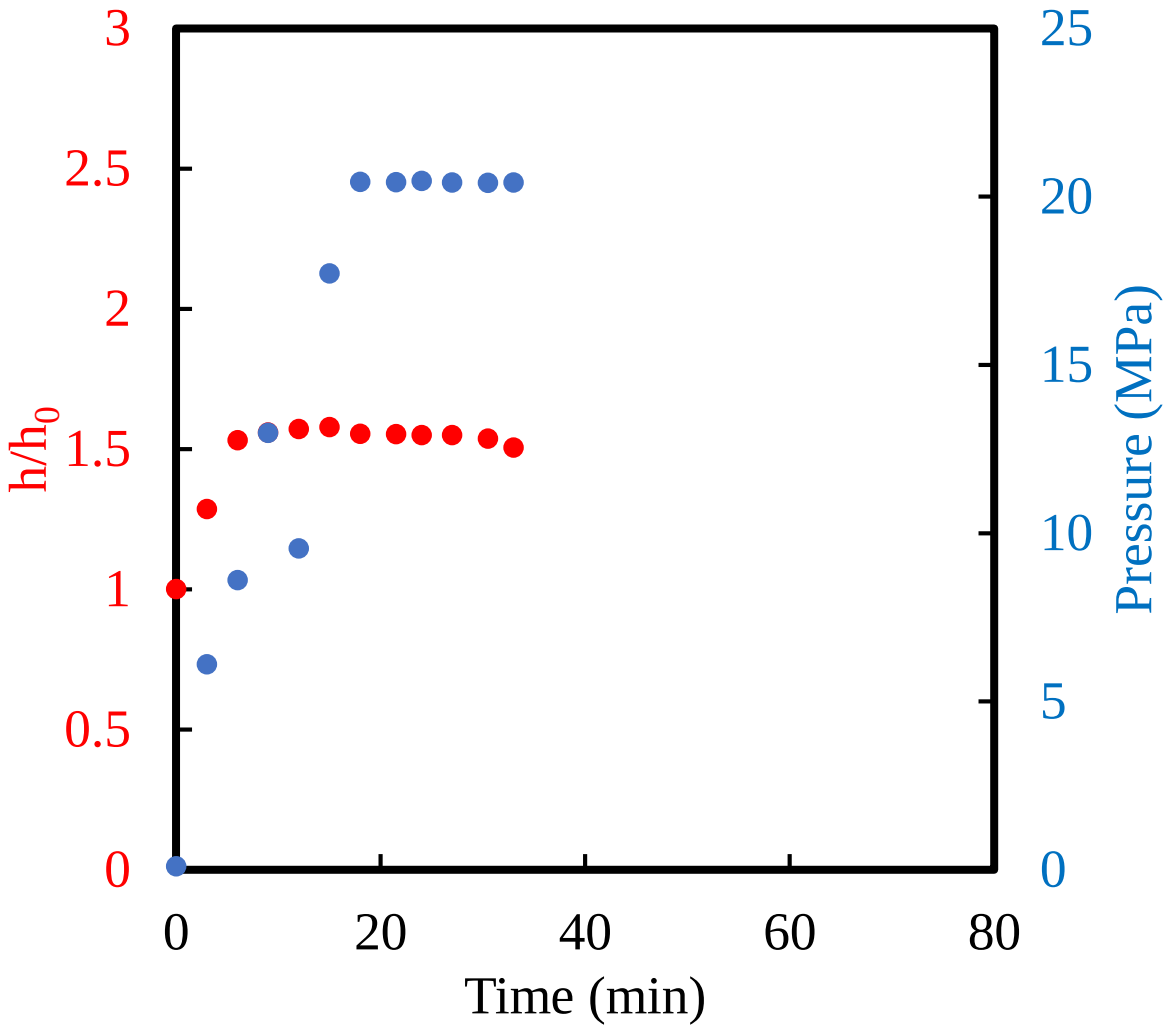

Figure 3.28 NMP expansion rate (red) and pressure (blue) against time with NMP amount of 9.8000 mmol

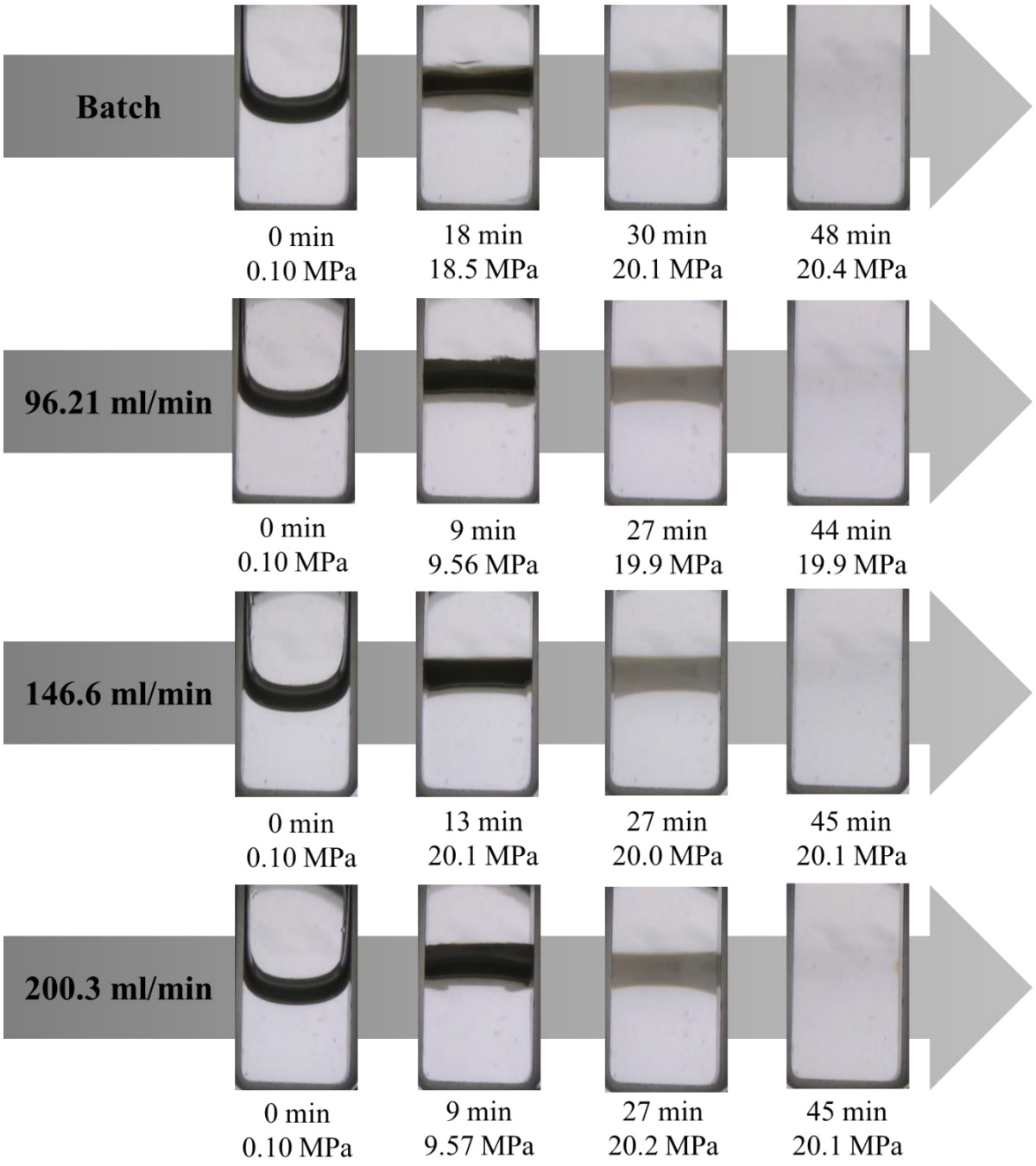

Figure 3.29 Time-lapse images for CO_2 and NMP from the beginning of the experiment until the homogenous phase was formed with a different flow rate

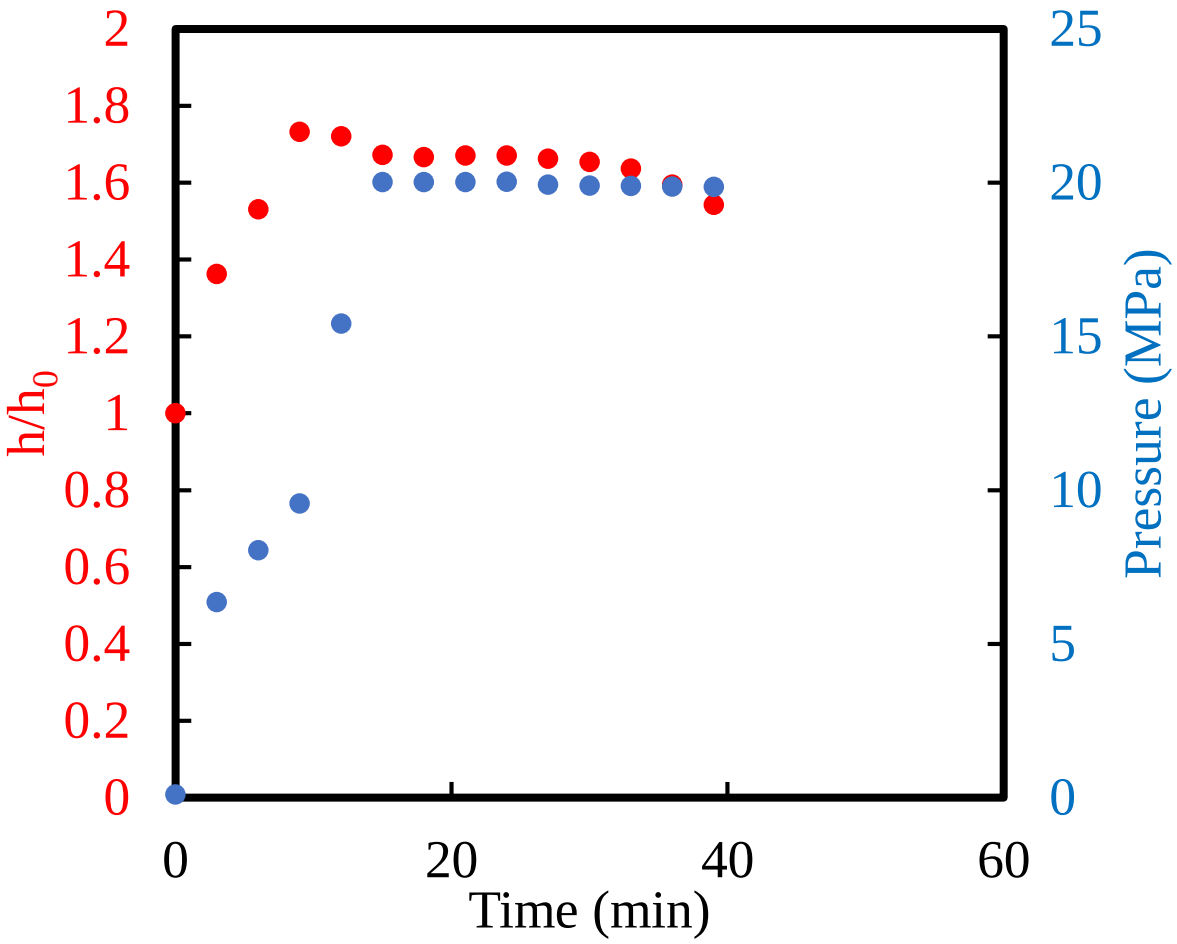

Figure 3.30 NMP expansion rate (red) and pressure (blue) against time with a CO_2 flow rate of 96.21 ml min^{-1}

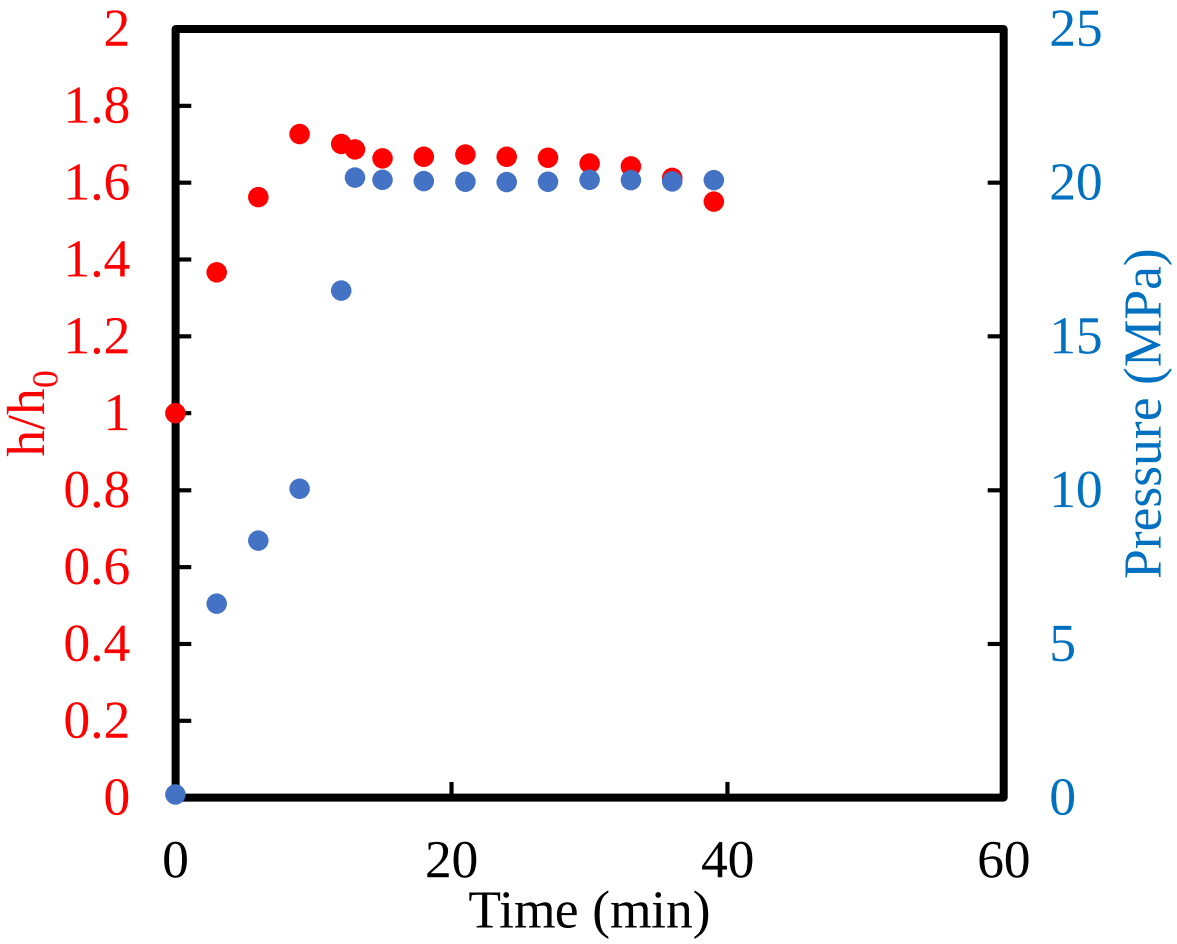

Figure 3.31 NMP expansion rate (red) and pressure (blue) against time with a CO_2 flow rate of 146.6 ml min^{-1}

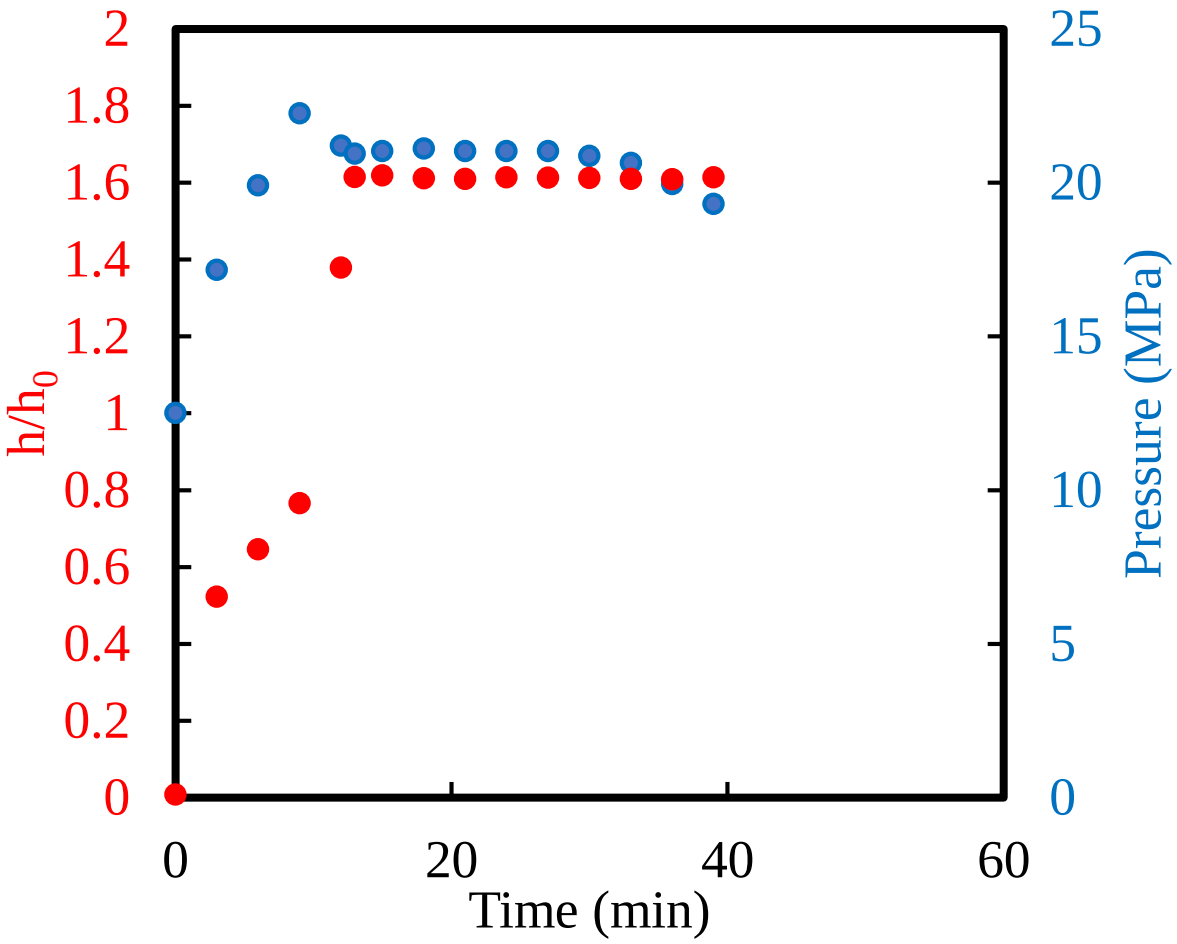

Figure 3.32 NMP expansion rate (red) and pressure (blue) against time with a CO_2 flow rate of 200.3 ml min^{-1}

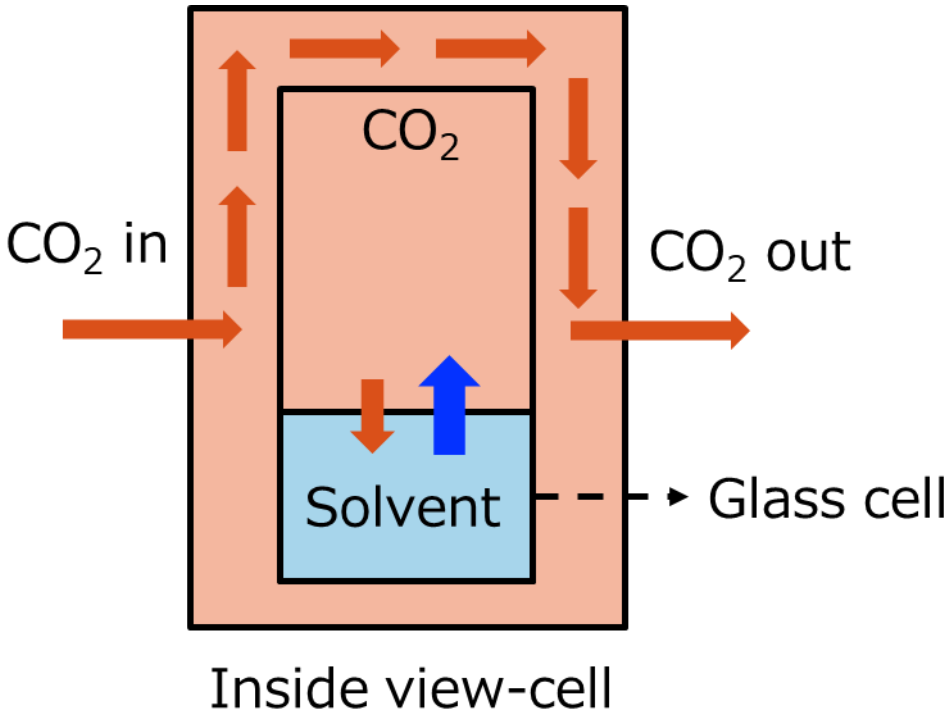

Figure 3.33 CO_2 flow illustration inside view-cell apparatus

3.4 References

[1] Baozhi Pan, Jian Lei, Lihua Zhang, Yuhang Guo, "Research on the physical properties of supercritical CO_2 and the log evaluation of CO_2-bearing volcanic reservoirs", *Journal of Geophysics and Engineering* 14 (2017) 1052-1060

[2] Julian Y. Zuo, Oliver C. Mullins, Denise Freed, and Dan Zhang, "A Simple Relation between Solubility Parameters and Densities for Live Reservoir Fluids", *Journal of Chemical & Engineering Data* 55 (2010) 2964-2969

[3] Marcela Palczewska-Tulińska and Paweł Oracz, "Vapor Pressures of 1-Methyl-2-pyrrolidone, 1-Methyl-azepan-2-one, and 1,2-Epoxy-3-chloropropane", *Journal of Chemical & Engineering Data* 52 (2007) 2468-2471

[4] D. Ambrose, C.H.S. Sprake, "Vapour pressures and normal boiling temperatures of aliphatic alcohols", *The Journal of Chemical Thermodynamics* 2 (1970) 631-645

[5] D. Ambrose, C.H.S. Sprake and R. Townsend, "Thermodynamic properties of organic oxygen compounds XXXIII. The vapour pressure of acetone", *The Journal of Chemical Thermodynamics* 6 (1974) 693-700

[6] Gosta Akerlof, "Dielectric constant of some organic solvent-water mixtures at various temperatures", *The Journal of the American Chemical Society* 54 (1932) 4125-4139

[7] Granzhan V.A., Kirillova O.G., "Physico-chemical study of N-methyl-2-pyrrolidone-methanol system", *Zh.Prikl.Khim* 43 (1970) 1875-1877

[8] Walter Dannhauser and Lowell W. Bahe, "Dielectric Constant of Hydrogen Bonded Liquids. III. Superheated Alcohols", *The Journal of Chemical Physics* 40 (1964) 3058-3066

[9] Hourri, J. M. St-Arnaud, and T. K. Bose, " Solubility of solids in supercritical fluids from the measurements of the dielectric constant: Application to CO_2–naphthalene", *Review of Scientific Instruments* 69 (1998) 2732-2737

Chapter 4 Development of carbon electrode by supercritical drying and its application in Li-air battery

4.1 Statement of problems and objectives

As stated in Chapter 1, in addition to the fundamental experiment about organic solvent expansion under the presence of $scCO_2$, the fabrication of electrodes using this method is vital to understanding how supercritical drying parameters affect the electrodes' structure. Moreover, increasing the mechanical strength of the electrode should be considered to improve electrode cyclability. Therefore, in this chapter, carbon nanofiber is utilized to strengthen the mechanical strength of an electrode. Finally, carbon nanofiber electrodes are applied to Li-air batteries to investigate its benefit. This chapter was published in the *Journal of Chemical Engineering of Japan* [1].

4.2 Experimental

4.2.1 Materials

This chapter divided the experiment into two parts; fabricating the electrode and applying the electrode to a CO_2/O_2 battery. For the first part of the experiment, acetylene carbon black (CB, purity 99.99 %) and carbon nanofiber (CNF, purity 98 %) were bought from Strem Chemicals and Pyrograf Products, Inc, and used as conductive materials. Then, poly(vinylidene fluoride) or PVDF was purchased from Fluorochem and used as a binder to bind the carbon particles together. After that, 1-Methyl-2-pyrrolidone (NMP, purity higher than 99.0 %) was supplied from Wako and used as a solvent. The pictures of CB and CNF, and the molecular structure of PVDF are shown in Figure 4.1, while NMP molecular structure is shown in Figure 3.1.

The experiment's second part is applying the fabricated electrodes to CO_2/O_2 batteries. For building the battery, Lithium bis(trifluoromethylsulfonyl) imide (LiTSFI) was purchased from Wako Pure Chemical Ind. Ltd. and used as Li-salt in the electrolyte. Moreover, the electrolyte was dimethyl sulfoxide (DMSO), purchased from Wako Pure Chemical Ind. Ltd. For the supercritical drying process, carbon dioxide was purchased from Fujii-Bussan with a purity of 99.5 % mass for fabricating the electrode under supercritical conditions and for CO_2/O_2 batteries.

4.2.2 Fabrication of electrodes

4.2.2.1 Preparing black slurry

This thesis mentions the solution containing CB or CNF with a binder (PVDF) and a solvent (NMP) as a black slurry.

Here are the steps to fabricate a black slurry. First, a binder was added into a solvent in a vial and ultra-sonicated under 60 °C until it was completely dissolved. Then, CB or CNF was added to it. Some of the samples also contained both CB and CNF. Next, this solution was ultra-sonicated for an hour and stirred with a magnetic stirrer for a night to homogenize CB or CNF in the solution. The solvent amount was also varied to investigate the effect of a solvent amount on the aerogel. The summary of the black slurry compositions is shown in Table 4.1.

4.2.2.2 Drying black slurry

1 gram of homogenized black slurry is placed into a petri dish with an inner diameter of 34 mm. Then the slurry is dried by two drying methods: evaporation and supercritical drying. Evaporation or thermal drying is when materials are dried by constant heating under atmospheric pressure until the solvent in the material is wholly evaporated, and the products are usually called xerogel [2]. In this research, for evaporation drying, the slurry is dried in a thermostat at 80 °C for 24 hours to ensure no solvent remains.

The other method is supercritical drying, which is conducted under pressure and at a temperature higher than the critical point of a fluid [2]. The fluid used for supercritical drying is CO_2. For this method, the black slurry is dried with supercritical drying equipment, which is shown in Figure 4.2. The critical point of CO_2 is 31.1 °C and 7.38 MPa [3]. Consequently, the experiment should be conducted under higher pressure and temperature than those specified. This research experiment was held at 20 MPa and 40 °C. However, the experiment was also held at 60 and 80 °C to observe the effect of drying temperature on aerogel. The steps to dry black slurry with supercritical drying are mentioned below.

First, a petri dish containing black slurry was placed in a high-pressure cell and tightly closed in order to avoid fluid leakage during the experiment. Immediately, the cell was put into a thermostat with a temperature set to the desired temperature and connected to a stainless steel pipe. The connectors between the cell and the line were tightly closed to prevent the fluid from

leaking. Finally, the experiment was conducted under 20 MPa. Thus, the back pressure to control the pressure was set to 20 MPa.

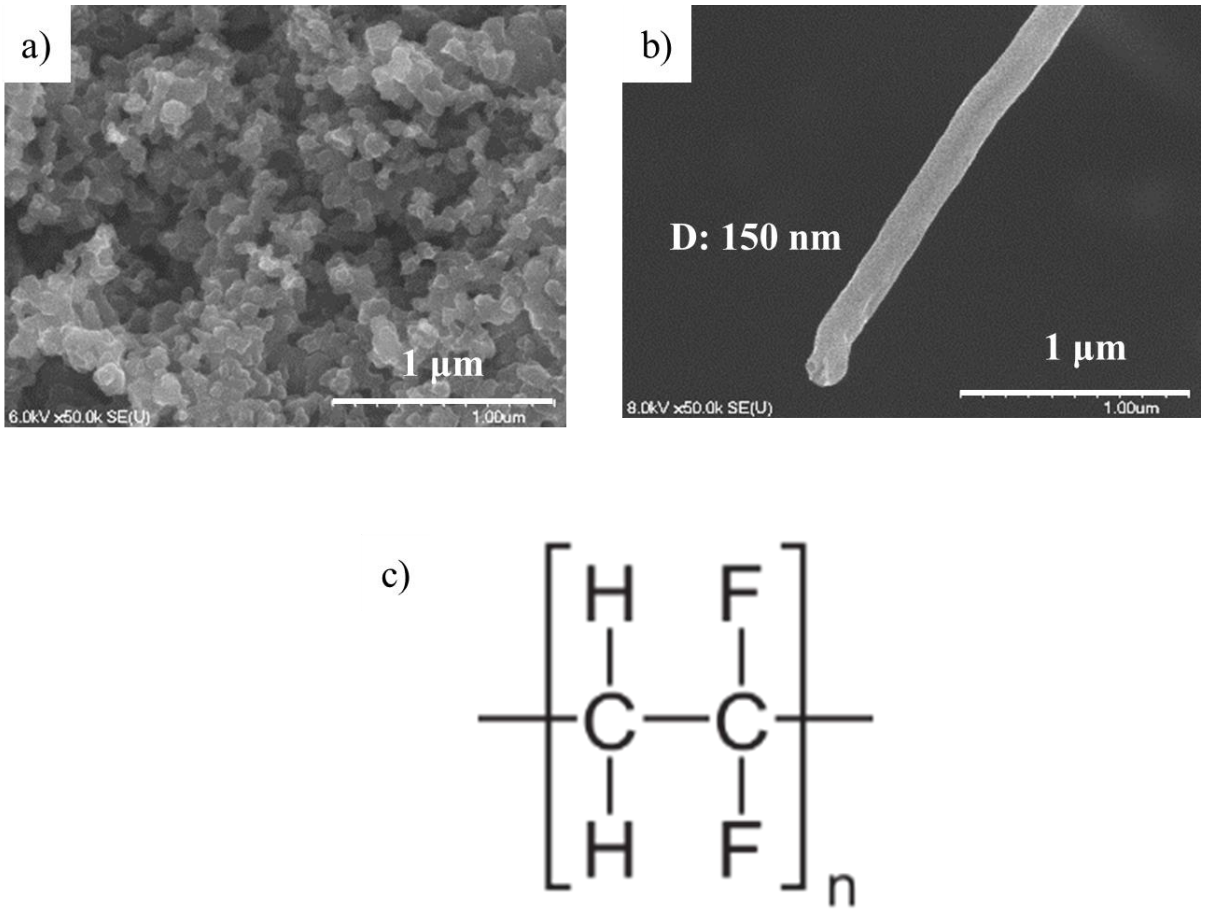

Figure 4.1 Images of a) carbon black (CB), b) carbon nanofiber (CNF), and c) molecular structure of poly(vinylidene fluoride) (PVDF)

Table 4.1 Summary of the electrode

Electrode No.	CB : CNF : PVDF : NMP (g/g/g/g)	Drying condition		
		Method	Temperature (°C)	Pressure (MPa)
C-1	1.0 : 0 : 1.0 : 27	Evaporation	80	0.1
C-2	1.0 : 0 : 1.0 : 16	Supercritical drying	40	20.0
C-3	1.0 : 0 : 1.0 : 20			
C-4	1.0 : 0 : 1.0 : 27			
C-5	1.0 : 0 : 1.0 : 32			
C-6	1.5 : 0 : 1.0 : 25	Evaporation	80	0.1
C-7	1.5 : 0 : 1.0 : 25	Supercritical drying	40	20.0
C-8			60	
C-9			80	
C-10	0 : 1.0 : 1.0 : 32	Evaporation	80	0.1
C-11	0.91 : 0.09 : 1.0 : 32	Supercritical drying	40	20.0
C-12	0.5 : 0.5 : 1.0 : 32			
C-13	0 : 1.0 : 1.0 : 32			

Before the experiment started, the valves were confirmed to be closed. Then, a CO_2 cylinder was opened at the beginning of the equipment, followed by the opening of the V1, V2, V4, and V5 valves. However, V4 was opened slowly to prevent sudden pressure change inside the high-pressure cell. After CO_2 filled the high-pressure cell and the pressure shown in the pressure meter was constant, the pump was turned ON so the pressure would increase to 20 MPa. Later, valve V6 was opened, followed by slowly opening the control valve or needle valve at the equipment's end. Then, the flow rate of CO_2 was controlled by adjusting the control valve while observing the wet gas meter. The CO_2 flow rate was adjusted to around 150 mL min^{-1}. A solvent trap was placed between the control valve and the wet gas meter to trap the solvent, which was flowing together with CO_2, to minimize the possibility of solvent flowing into the wet gas meter.

After 6 hours of drying, the pump was turned OFF and the CO_2 cylinder was closed. Then, the high-pressure cell was depressurized by letting the CO_2 flow out until the pressure shown in the pressure meter returned to atmospheric pressure. The flow rate of CO_2 was controlled at around 200 mL min^{-1} by adjusting the control valve while observing the wet gas meter. Next, the high-pressure cell was opened and the petri dish containing aerogel (dried black slurry) was brought out.

4.2.2.3 Preparing Li-O_2/CO_2 battery coin cell

The aerogel was cut into a round electrode with a diameter of 13.0 mm. Then, the weight of the electrode was measured with a balance. Before assembling the battery, LiTSFI was dissolved in DMSO to make 1 M LiTFSI/DMSO electrolyte. Then, a coin cell case, lithium metal, spacers, electrolyte, Whatman glass fiber, electrode, and gas diffusion layer (carbon fiber) were brought into a glove box. Next, the air in the glove box was removed until the humidity in the glove box was below 5 %. Humidity should be as low as possible to prevent lithium metal from reacting with water vapor in the air. Soon after, argon gas was filled into the glove box. Finally, the battery was assembled with the order of coin cell case, lithium metal, LiTFSI/DMSO electrolyte on Whatman glass fiber, electrode, spacers, and coin cell case inside the glove box, as illustrated in Figure 4.3. Soon, the assembled battery was brought to a crimping machine to close the battery. Then, it was brought out from the glove box.

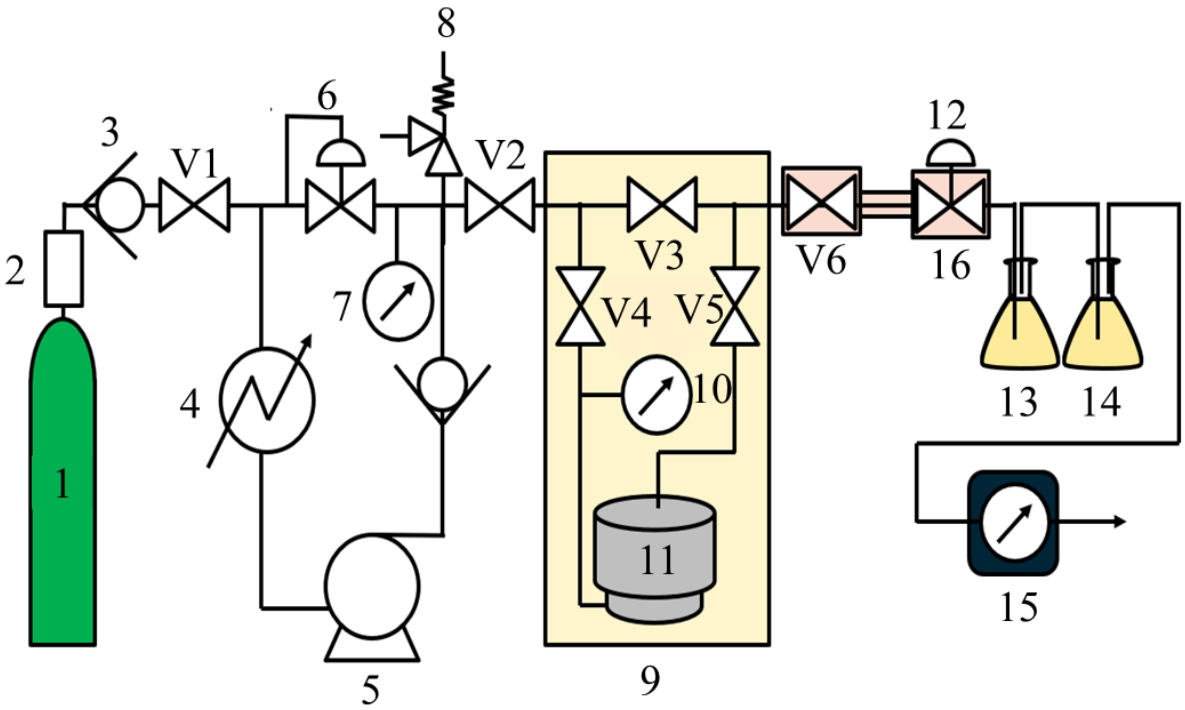

1. Liquefied carbon dioxide
2. Dehydrator
3. Check valve
4. Condenser
5. Pump
6. Back pressure valve
7. Pressure meter
8. Safety valve
9. Thermostat
10. Digital pressure meter
11. Drying cell
12. Control valve
13. Solvent trap
14. Water trap
15. Wet gas meter
16. Ribbon heater

V1-6 Stop valve

Figure 4.2 Supercritical drying apparatus

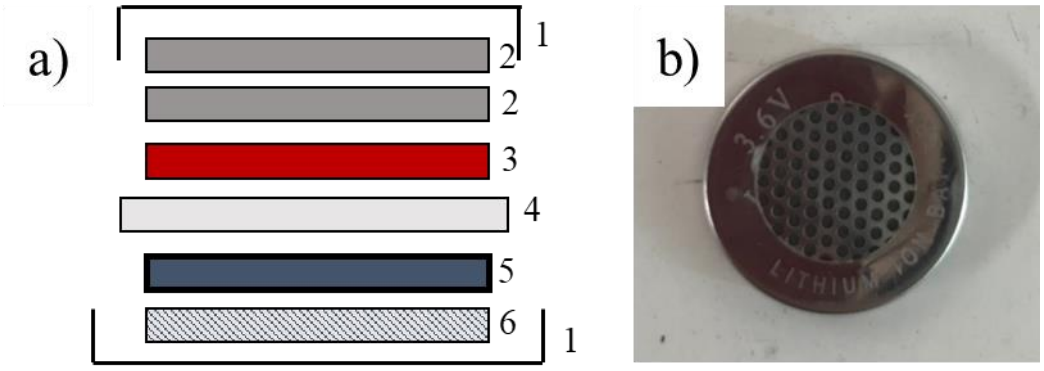

1. Coin cell case
2. Spacers
3. Lithium metal
4. Separator (electrolyte)
5. Electrode
6. Gas diffusion layer

Figure 4.3 Coin cell: a) schematic diagram and b) top image

4.2.3 Analysis

4.2.3.1 Morphology investigation

The carbon electrode morphology was investigated using Scanning Electron Microscope (SEM) (JSM-6000 Plus, JEOL). The objects studied were the top surface and the electrode cross-section.

4.2.3.2 Porosity measurement

Porosity measurement was conducted to determine the differences in aerogel for different cases. To obtain the porosity value, first, the total volume of the aerogel was calculated by multiplying the top area and thickness of the aerogel. The equation of this calculation is as follows.

$$V_{total} = A_{top} \times t \qquad \text{(Equation 4.1)}$$

Where, V_{total} (cm^3), A_{top} (cm^2), and t (cm) are the total volume, the top area, and the thickness of an aerogel, respectively. The top area and thickness of the aerogel were obtained using an image analysis software named ImageJ. A bird-eye view picture of the aerogel was taken for the top area. Then, it was opened in ImageJ software. The image was converted to 8-bit and its threshold was adjusted to obtain a black-and-white image. Afterward, the top area was determined using particle analysis in the software. The thickness was determined by calculating the average of the aerogel thickness from approximately 200 points of 20 cross-section SEM images of an aerogel using ImageJ.

Furthermore, the void volume of the aerogel was obtained by subtracting the total volume from the bulk volume of the aerogel from Equation 4.2. This bulk volume was obtained by dividing the weight of solids (black slurry without solvents) and those densities. The densities of the solids are shown in Table 4.2. Finally, the porosity was calculated from the ratio of void volume and total volume of an aerogel (Equation 4.3).

$$V_{total} = V_{void} + \sum \frac{W_{solid}}{\rho_{solid}} \qquad \text{(Equation 4.2)}$$

$$Porosity = \frac{V_{void}}{V_{total}} \qquad \text{(Equation 4.3)}$$

Where, V_{void} (cm^3), W_{solids} (g), and ρ_{solid} $(g \cdot cm^{-3})$ are the void volume of aerogel, the solids' weight, and the solids' density.

Table 4.2 Density of Acetylene carbon black and PVDF

Substance	Density (g cm^{-3})	Ref.
Carbon black	2.0233	[6]
Carbon nanofiber	1.9	*)
PVDF	1.6482	[6]

*) product specification

4.2.3.3 Sheet conductivity measurement

A four-point probe method was used to measure electrical conductivity. Figure 4.4 depicts the schematized four-point probe measurement, and Equation 4.4 calculates sheet conductivity [4, 5].

$$\sigma = \frac{\ln 2}{\pi t R \cdot F(t/s)} \qquad \text{(Equation 4.4)}$$

Where t is thickness, R is resistance, and s is the distance between probes, which was fixed at 0.5 cm. In this experiment, t 's value is less than 0.2; as a result, the value of $F(t/s)$ is approximately 1. The resistance R value was determined from a slope value of a linear relationship between potential V and electric current I. The linear scan voltammetry function determined potential and electric current at 0.1 V s^{-1} scan rate conducted with Potentiostat/Galvanostat (VersaSTAT3-200, Princeton Applied Research).

4.2.3.4 Capacity and ten cycles measurement

The coin cell put together in section 4.2.2.3 was inserted into a coin cell holder in an aluminum cell box, which was then linked to the potentiostat and galvanostat. The temperature within the cell box was kept at 25 °C. Next, a mixture of oxygen and carbon dioxide was pumped inside at a flow ratio of 1. At atmospheric pressure, the total flow rate of the mixed gases was regulated at 100 mL min^{-1}. The Potentiostat/potentiometry Galvanostat's function was used to determine the electrode's capacity. The battery was discharged and discharged ten times throughout the 10-cycle experiment, and the measurement range was then adjusted to 0 to 0.5 mA h cm^{-2}. The electric current was constant for both tests at 0.1 mA (0.0750 mA cm^{-2} cathode). The schematized apparatus for this experiment is displayed in Figure 4.5.

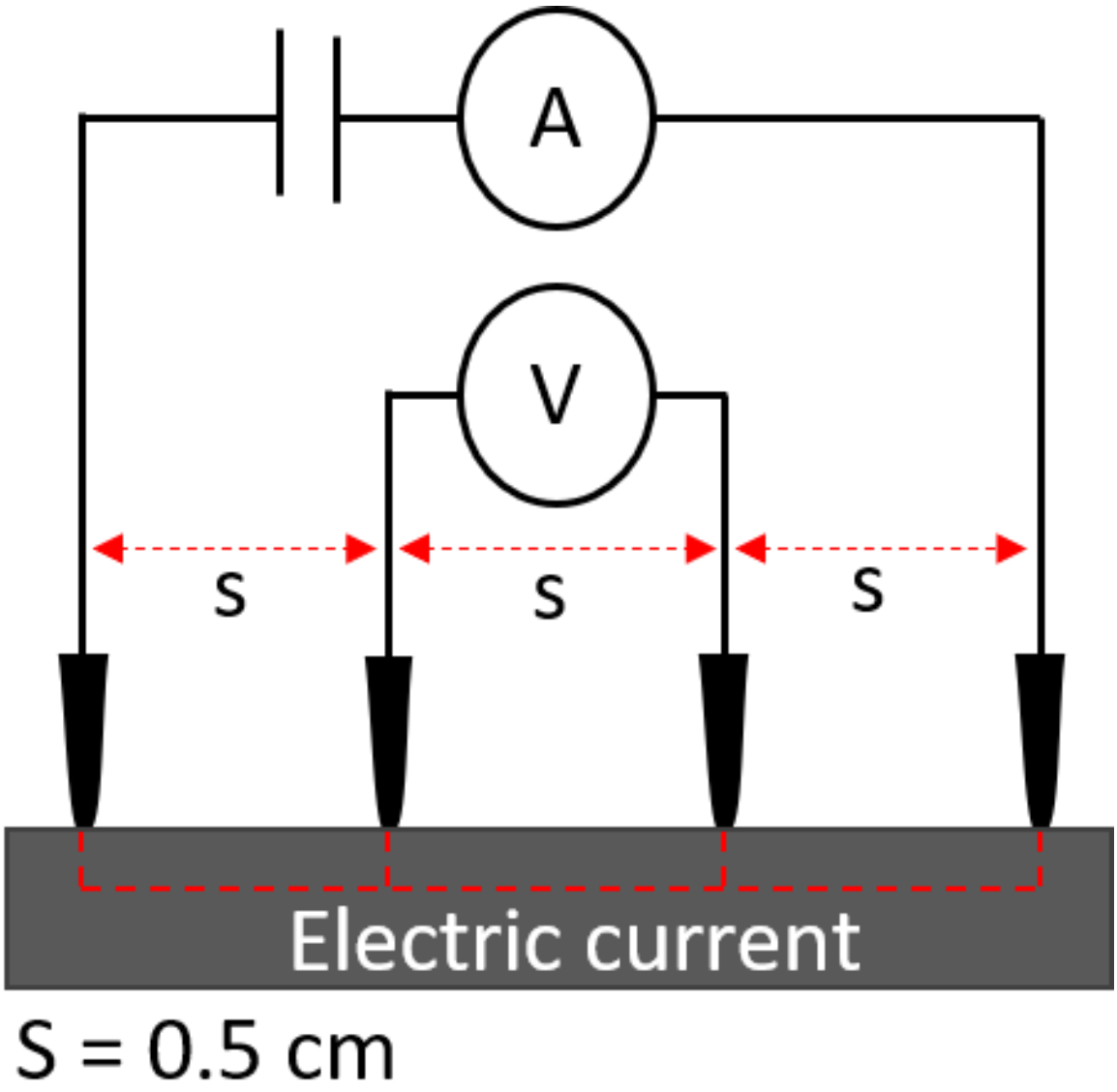

Figure 4.4 Four-point probe method

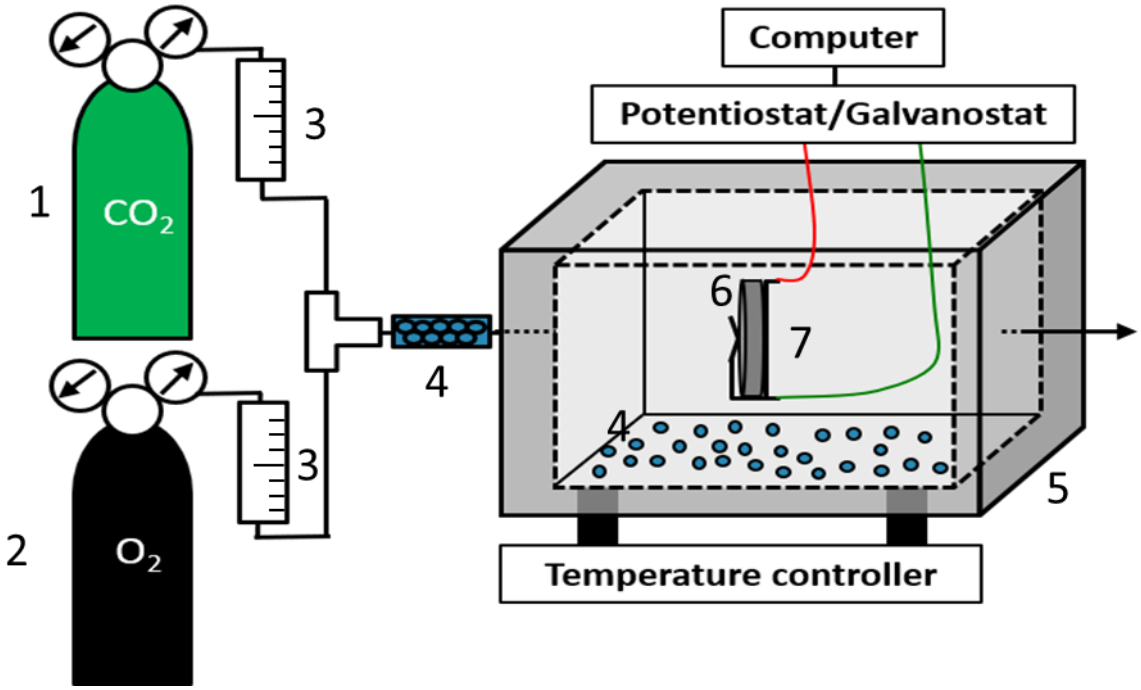

1. CO_2 cylinder
2. O_2 cylinder
3. Flowmeter
4. Silica gel
5. Aluminum cell box
6. Coin cell battery
7. Coin cell holder

Figure 4.5 Battery test apparatus

4.3 Result and discussion

4.3.1 Solvent amount in the black slurry

In the experiment section, the solvent amount (NMP) in the black slurry was varied to investigate the effect of a solvent amount on the fabricated aerogel. Black slurry components are summarized in Table 4.3. In this experiment, the amount of CB, PVDF, and drying conditions were fixed to minimalize other effect factors. C-1 is CB electrode made by evaporation drying at 80 °C and atmospheric pressure when CB:PVDF:NMP=1:1:32. C-2 to C-5 are electrodes made by supercritical drying at 20 MPa and 40 °C with the composition ratio of CB:PVDF:NMP were 1:1:16, 1:1:20, 1:1:27, and 1:1:32, respectively.

Top view, surface SEM, and cross-section SEM images of aerogel made by the evaporation method are shown in Figure 4.6. The top view image shows that the aerogel fabricated with the evaporation method developed cracks. Moreover, the surface of the aerogel is very dense, as shown in the SEM image, while the cross-section SEM image shows a very thin aerogel.

Top view, surface SEM, and cross-section SEM images of aerogel made by supercritical method are shown in Figure 4.6 to Figure 4.10. Unlike the aerogel made by evaporation drying, all aerogels fabricated with supercritical drying show no crack in top view images (Figure 4.7 to Figure 4.10 section a). Moreover, the availability of pores can be confirmed from surface SEM images of each aerogel (Figure 4.7 to Figure 4.10 section b). Furthermore, the thicknesses shown in Figure 4.7 to Figure 4.10 section c are much more significant than aerogel made by evaporation drying (Figure 4.6 section c). This phenomenon happens due to the presence of surface tension and capillary stress in evaporation drying that makes pores in the aerogel collapse [7].

The calculation of the porosity of these aerogels is shown in Table 4.4. Porosity was determined by the percentage of void volume and total volume, calculated from the aerogels' thickness and surface area, as explained in section 4.2.3. The porosity was plotted in Figure 4.11. The graph shows that more solvent in the black slurry mixture gives a more significant porosity value. This result was parallel to the aerogel thickness in Figure 4.12.

The sheet conductivity of fabricated electrodes was measured, and the result was plotted into a graph shown in Figure 4.13. However, the sheet conductivity of the electrode made by the evaporation method was not measured due to its defect. The value of sheet conductivity for

electrodes fabricated by supercritical drying is smaller with a more significant amount of solvent. Moreover, the electrode with less solvent shows more considerable sheet conductivity. In the case of C-5, it has a high pore volume that makes the resistivity value significant. Consequently, because sheet conductivity has a perpendicular relationship with resistance value, its value became lowest compared to other electrodes. This kind of result also can be confirmed in the literature [8].

Table 4.3 Summary of black slurry using different amounts of solvent

Electrode No.	CB : PVDF : NMP (g/g/g)	Drying condition		
		Method	Temperature (°C)	Pressure (MPa)
C-1	1.0 : 1.0 : 32	Evaporation	80	0.1
C-2	1.0 : 1.0 : 16	Supercritical drying	40	20.0
C-3	1.0 : 1.0 : 20			
C-4	1.0 : 1.0 : 27			
C-5	1.0 : 1.0 : 32			

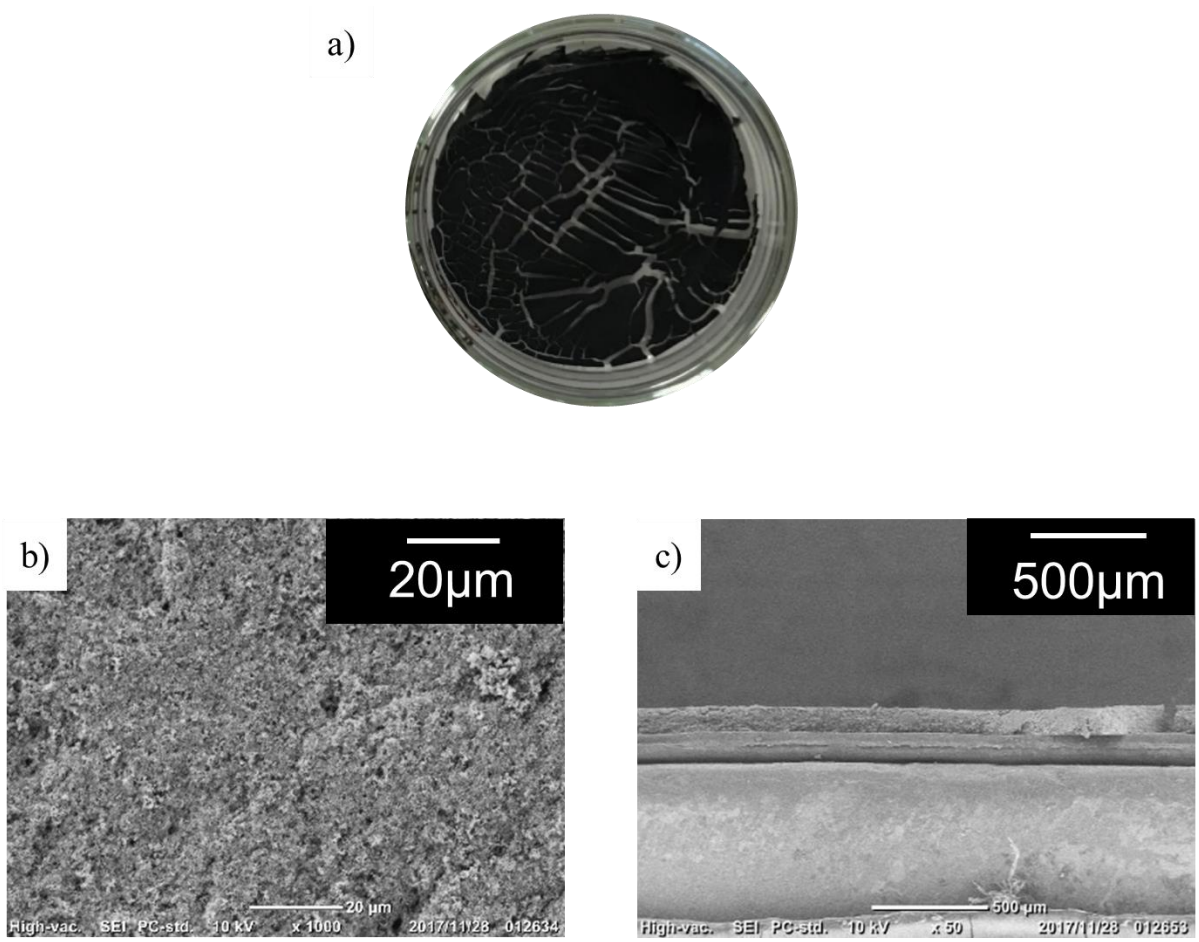

Figure 4.6 CB electrode made by an evaporation method (C-1): a) Top view, b) surface SEM, and c) cross-section SEM images

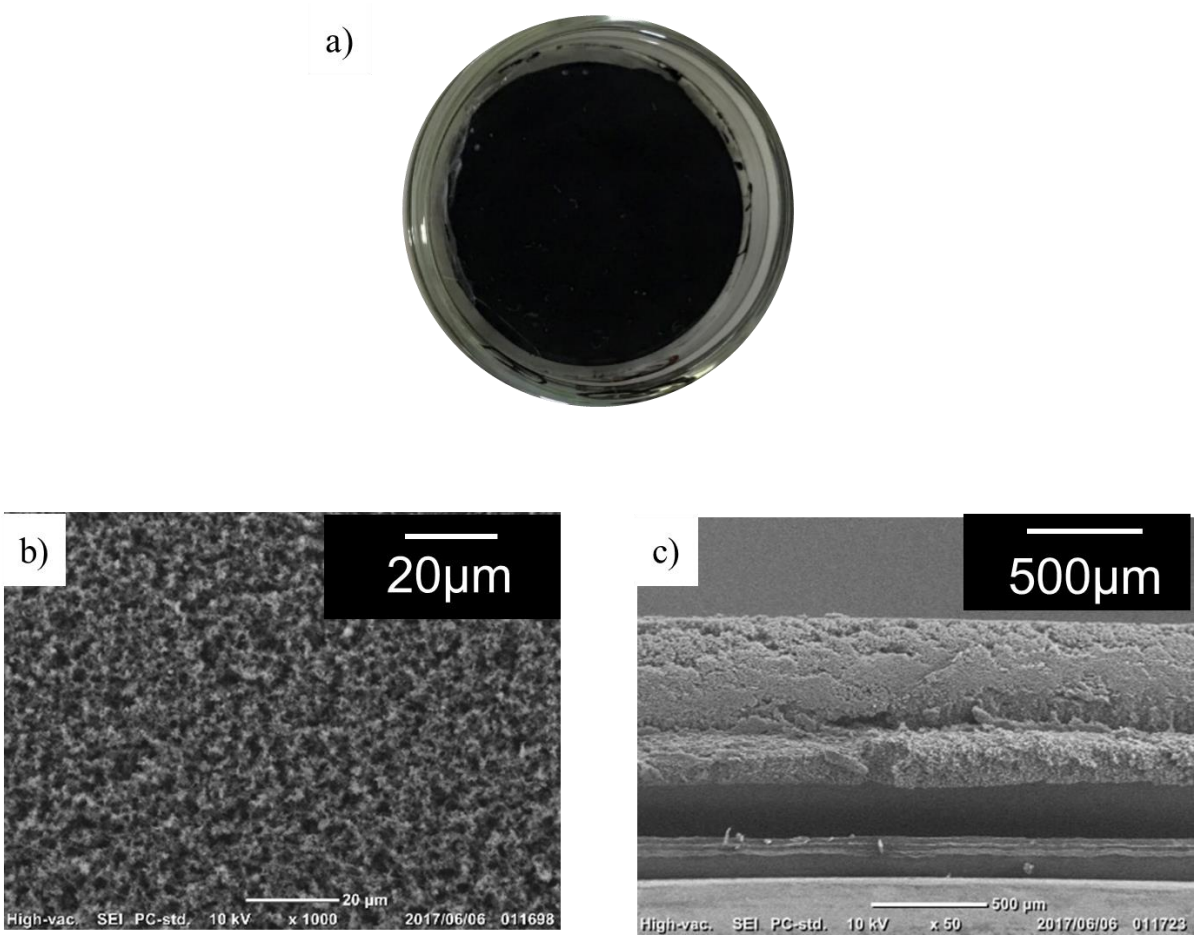

Figure 4.7 CB electrode made by supercritical method (C-2): a) Top view, b) surface SEM, and c) cross-section SEM images

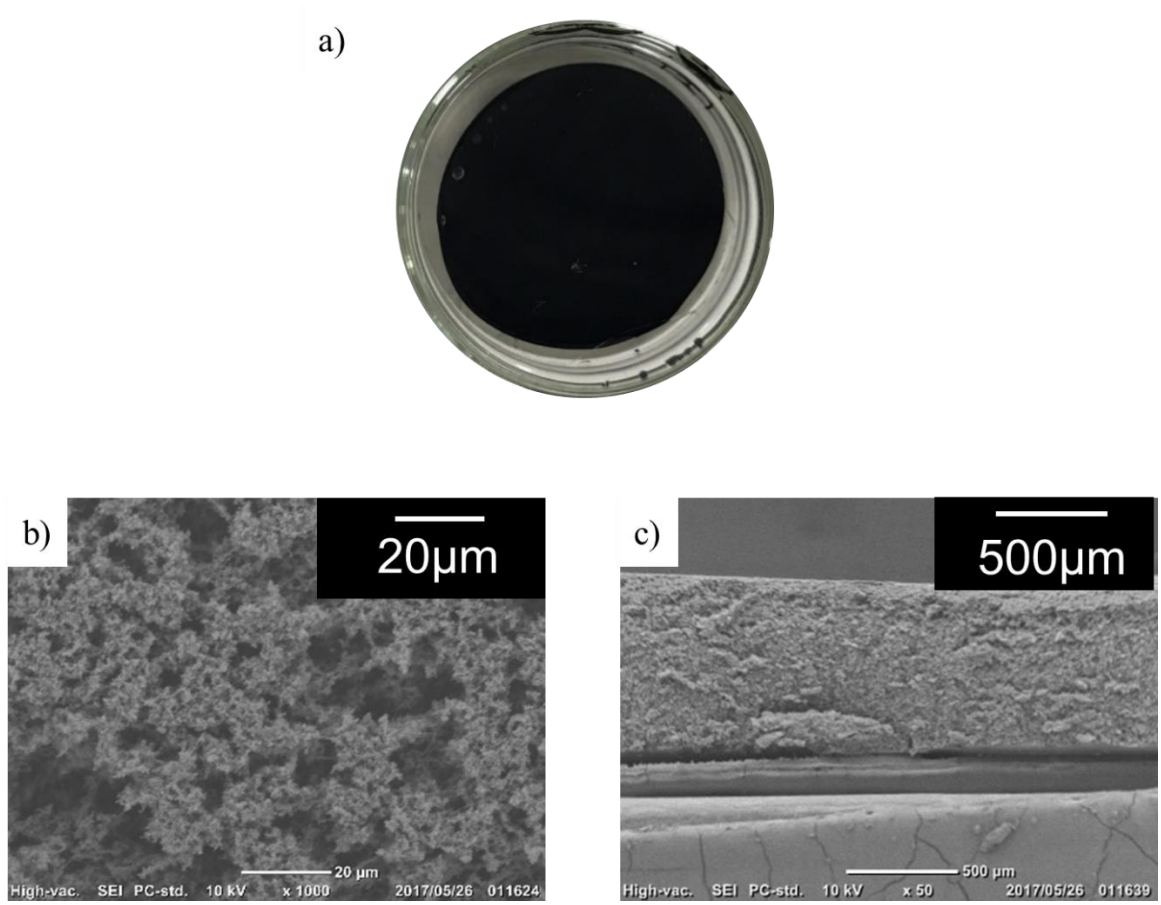

Figure 4.8 CB electrode made by supercritical method (C-3): a) Top view, b) surface SEM, and c) cross-section SEM images

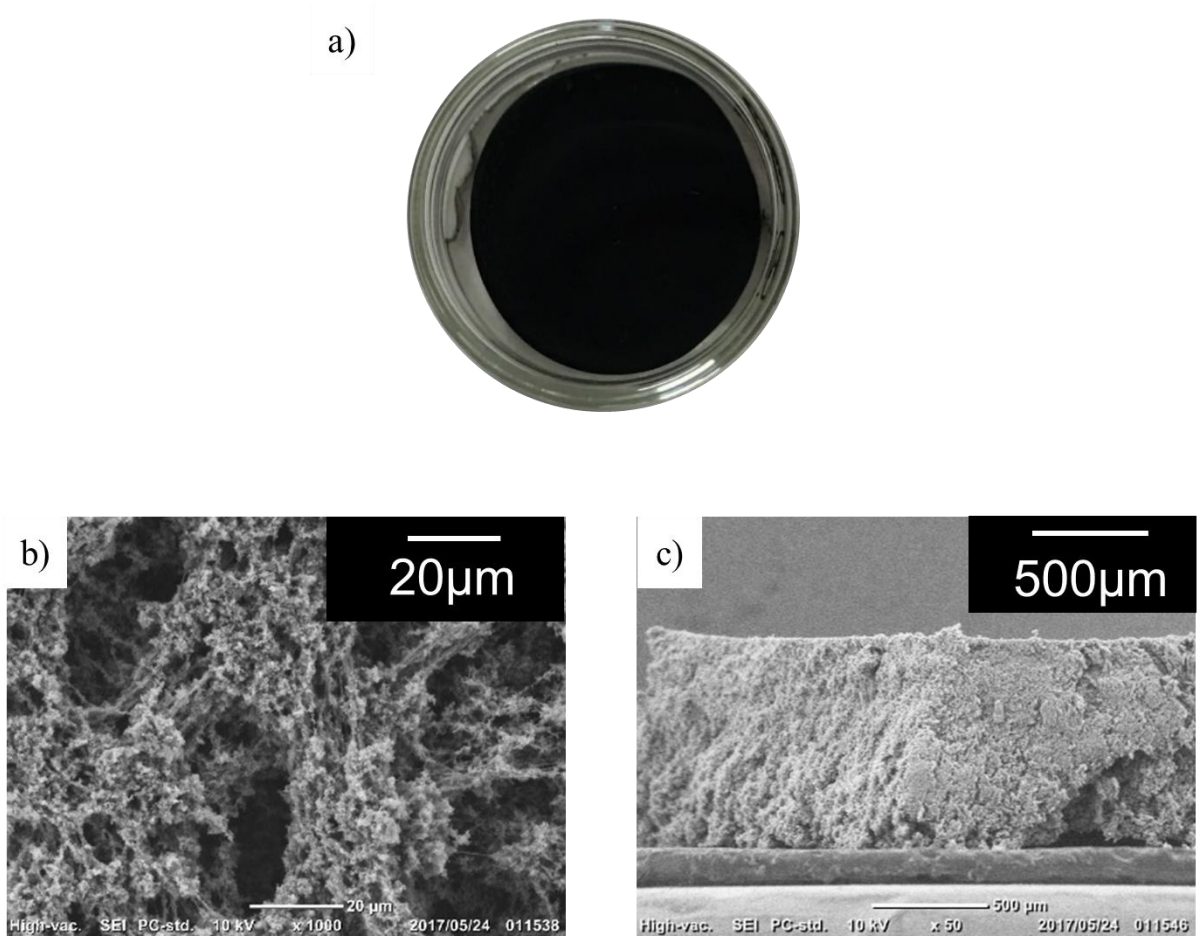

Figure 4.9 CB electrode made by supercritical method (C-4): a) Top view, b) surface SEM, and c) cross-section SEM images

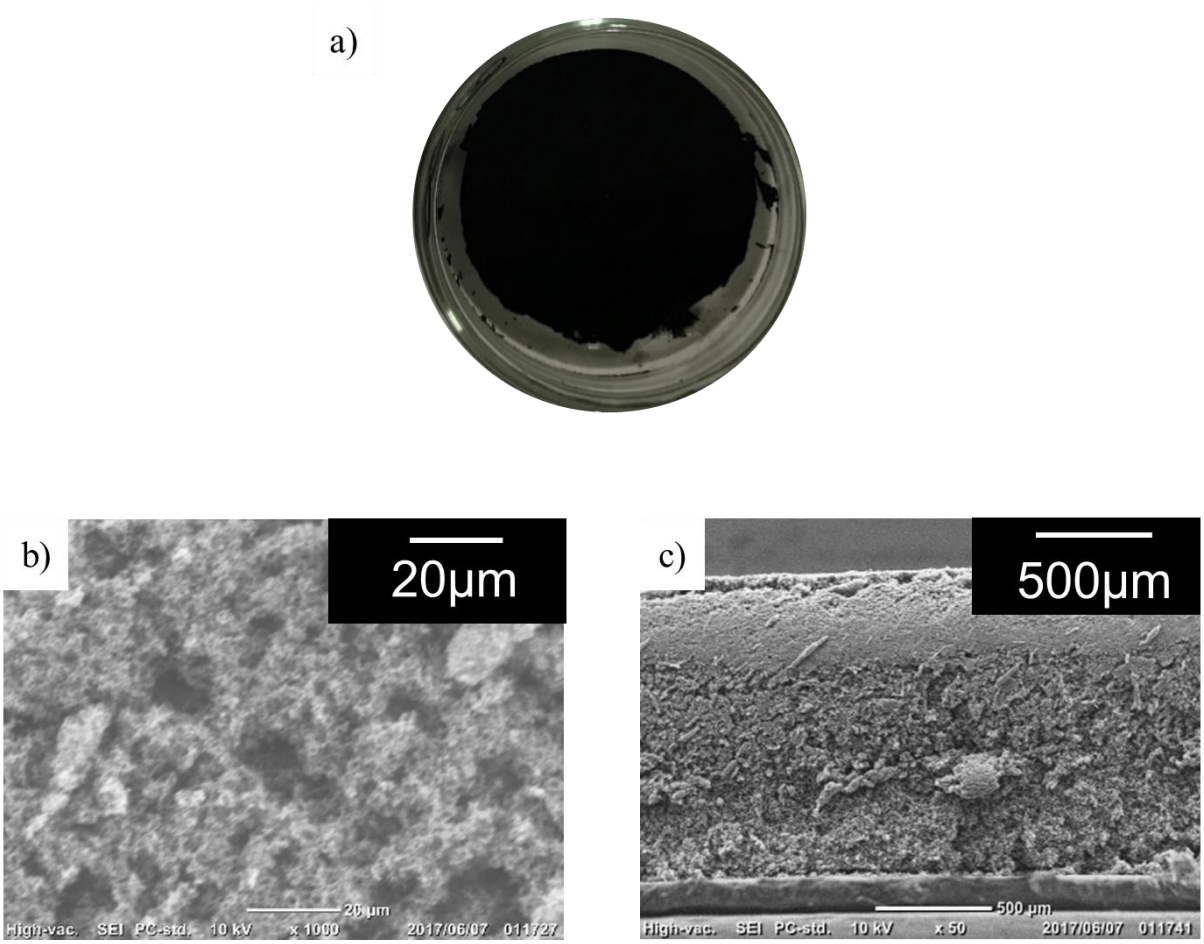

Figure 4.10 CB electrode made by supercritical method (C-5): a) Top view, b) surface SEM, and c) cross-section SEM images

Table 4.4 Porosity calculation of each electrode when CNF : PVDF : solvent = 1 : 1 : 32

Sample No.	Mass (g)	Top area (cm^2)	Thickness (mm)	Total volume (cm^3)	Density (g cm^{-3})	Void volume (cm^3)	Porosity
C-1	0.069	6.400	1.055	0.068	1.024	0.029	0.436
C-2	0.111	6.833	6.885	0.471	0.237	0.409	0.870
C-3	0.092	6.982	8.057	0.563	0.164	0.512	0.910
C-4	0.069	7.635	8.421	0.643	0.108	0.605	0.941
C-5	0.059	6.838	10.028	0.686	0.009	0.654	0.953

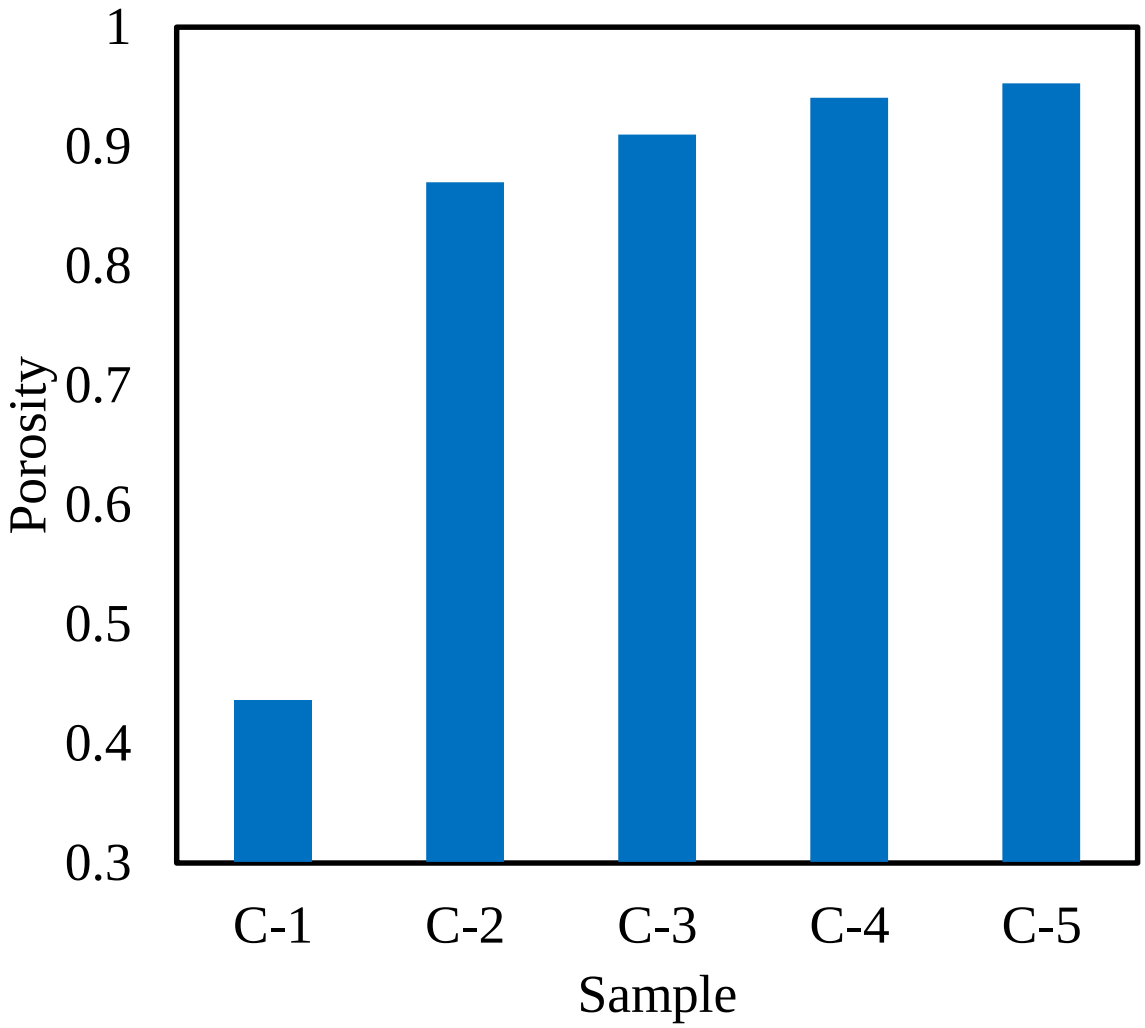

Figure 4.11 Porosity of CB electrode with various amounts of solvent

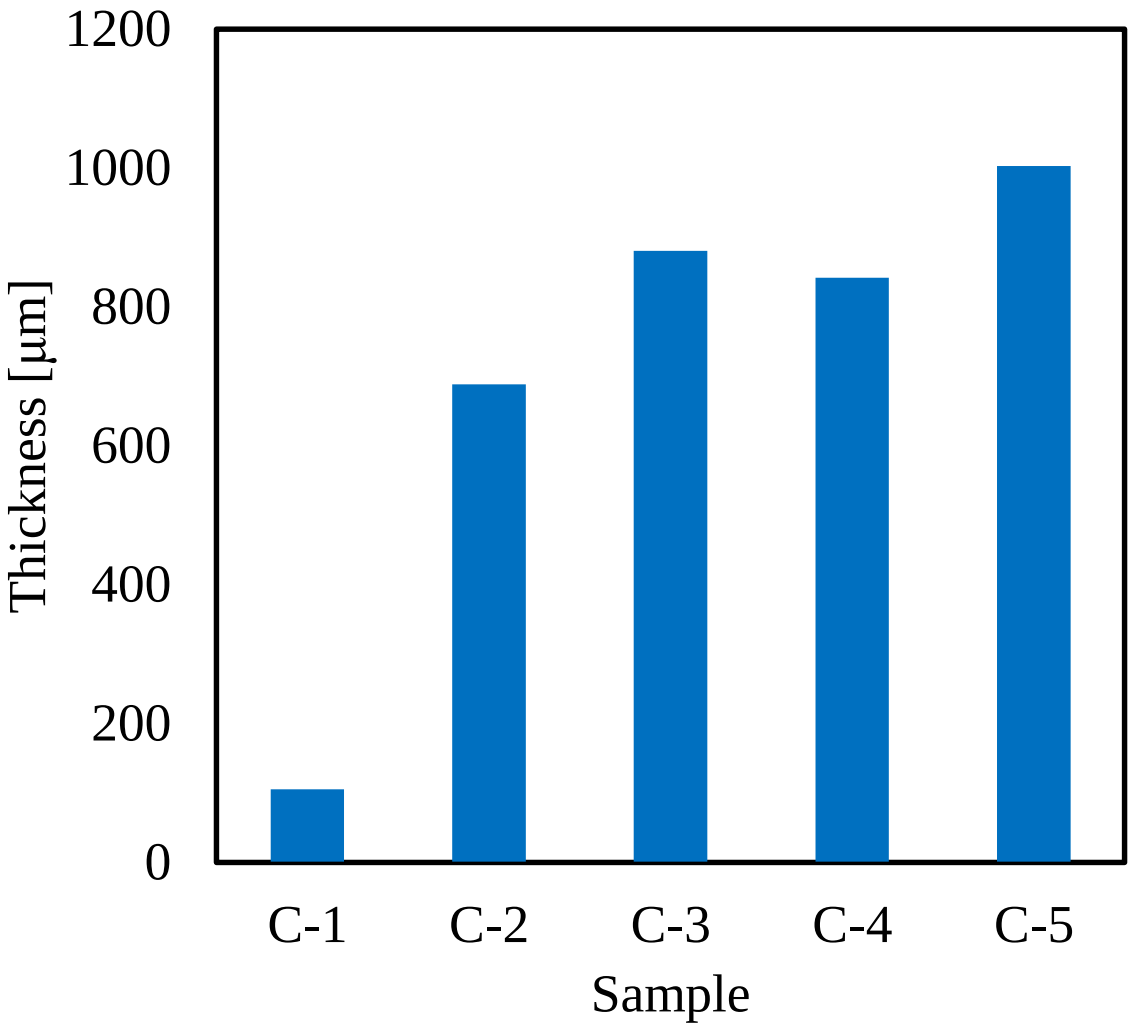

Figure 4.12 Thickness of CB electrode with various amounts of solvent

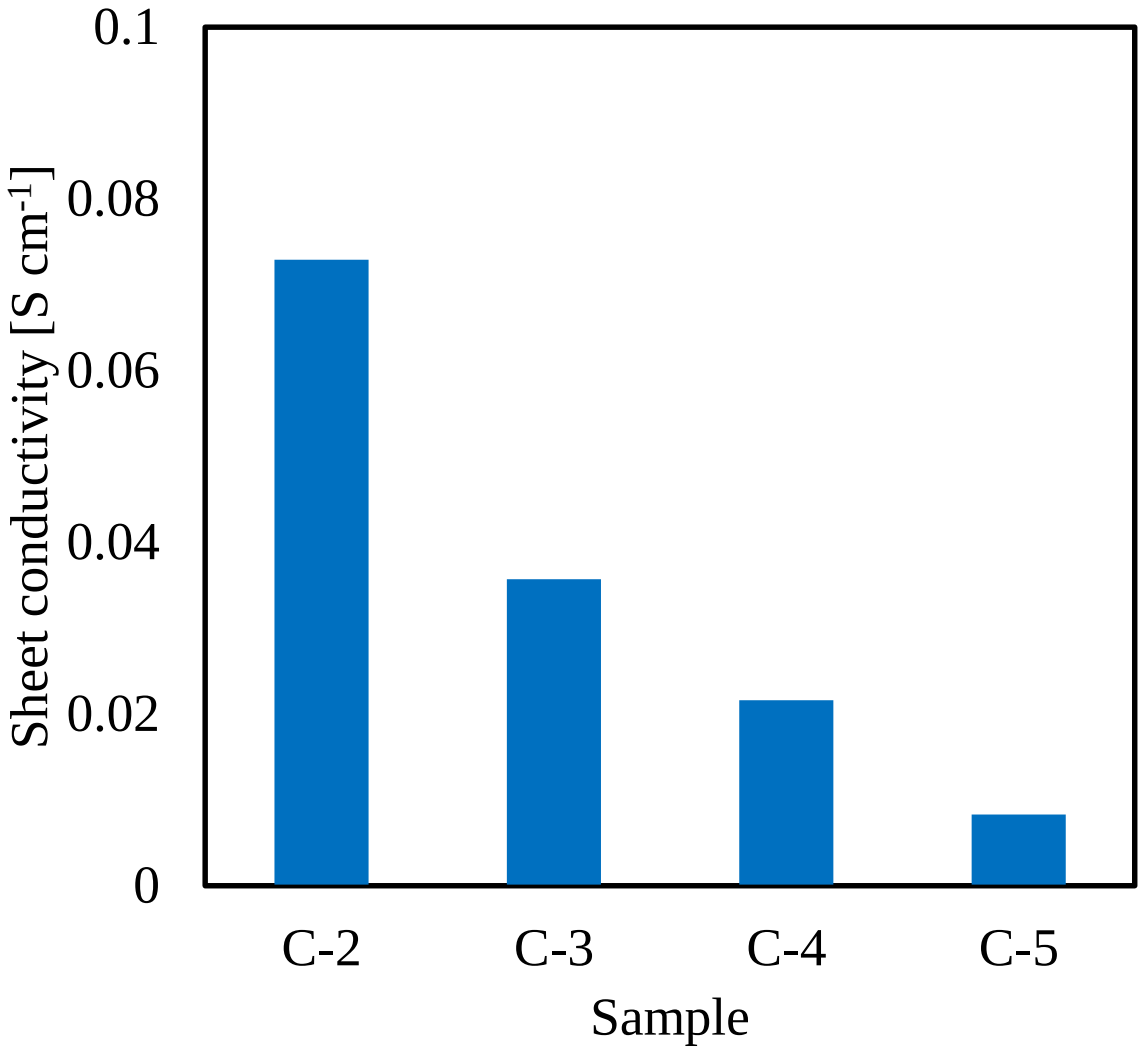

Figure 4.13 Sheet conductivity of CB electrode with various amounts of solvent

4.3.2 Drying temperature

In this section, electrodes are fabricated at various temperatures using the supercritical drying method to investigate the drying temperature's effect on the electrodes' structure. A summary of the electrodes made by evaporation drying and supercritical drying at various temperatures is displayed in Table 4.5. In this section, the composition ratio of the electrodes was fixed at CB:PVDF:NMP=1.5:1:25 to minimize error. C-6 is an electrode fabricated by evaporation drying at atmospheric pressure and 80 °C. C-7 to C-9 are electrodes fabricated by supercritical drying at 20 MPa, while the drying temperature was 40, 60, and 80 °C, respectively.

Followed by the table for composition summary, the top view images, cross-section SEM images, and surface SEM images for electrodes C-6 to C-9 are shown in Figure 4.14, Figure 4.15, Figure 4.16, and Figure 4.17. Figure 4.14 for C-6, made by evaporation drying, shows a similar result to C-1 in the previous section (Figure 4.6), which was also fabricated by evaporation drying. In addition, the top view image shows cracks because of pore collapse due to surface tension and capillary stress during the drying process.

Figure 4.15 to Figure 4.17 show the top view, cross-section, and surface SEM images for electrodes made by supercritical drying at various temperatures; 40, 60, and 80 °C, respectively. Top view images show that electrodes dried at 40 and 60 °C have similar characteristics where no crack can be found on the surface. However, C-9, dried at 80 °C, has cracks from the outer part. When drying at 80 °C, from the first step of supercritical drying, the temperature was already 80 °C while the pressure was gradually increased until it reached the critical pressure point and finally 20 MPa. The initial high temperature caused the electrode to start drying like evaporation drying before it became a homogenous phase. However, because the pressure increased gradually after the pressure reached critical pressure, supercritical drying also took part in the drying, which prevented further cracks from forming. Compared to electrode C-6, electrodes C-7 to C-9 have large porous because C-7 to C-9 were dried by supercritical drying; thus, pore collapse did not occur.

The porosity calculation for this section is displayed in Table 4.6, and the porosity and thickness graphs are shown in Figure 4.18 and Figure 4.19. From the porosity calculation and graph, the conclusion shows that there is no significant difference under different drying temperatures. This phenomenon might happen because NMP has a high boiling point [9]. Thus, even though the temperature was varied, the effect of drying temperature on the electrode

porosity is insignificant. In the previous section, when the thickness of the electrode is larger, the porosity is also more significant. However, in this section, the porosity values are similar, while the thickness in Figure 4.19 is different for each electrode.

Then, the sheet conductivity was measured and plotted in Figure 4.20. In this figure, the highest sheet conductivity is C-8 when the drying temperature is 60 °C. Conversely, the lowest sheet conductivity is C-7 when drying is 40 °C. In theory, PVDF crystalline has the ability as a conductive to bring electricity. Moreover, higher temperatures will increase the PVDF β-crystalline and produce higher sheet electrical conductivity [10]. However, in this case, even though the sheet conductivity of C-8 is higher than C-7, C-9 shows lower sheet conductivity. This result is because C-9 has cracks that cut off the electricity between the open cracks. These cracks made the electrode's resistance more significant, and because resistance and sheet conductivity have a perpendicular relationship, the sheet conductivity will become small when the resistance is enormous. The relationship between sheet conductivity can be seen in Equation 4.4.

Table 4.5 Summary of electrodes fabricated in various temperature

Electrode No.	CB : PVDF : NMP (g/g/g)	Drying condition		
		Method	Temperature (°C)	Pressure (MPa)
C-6	1.5 : 1.0 : 25	Evaporation	80	0.1
C-7			40	
C-8	1.5 : 1.0 : 25	Supercritical drying	60	20.0
C-9			80	

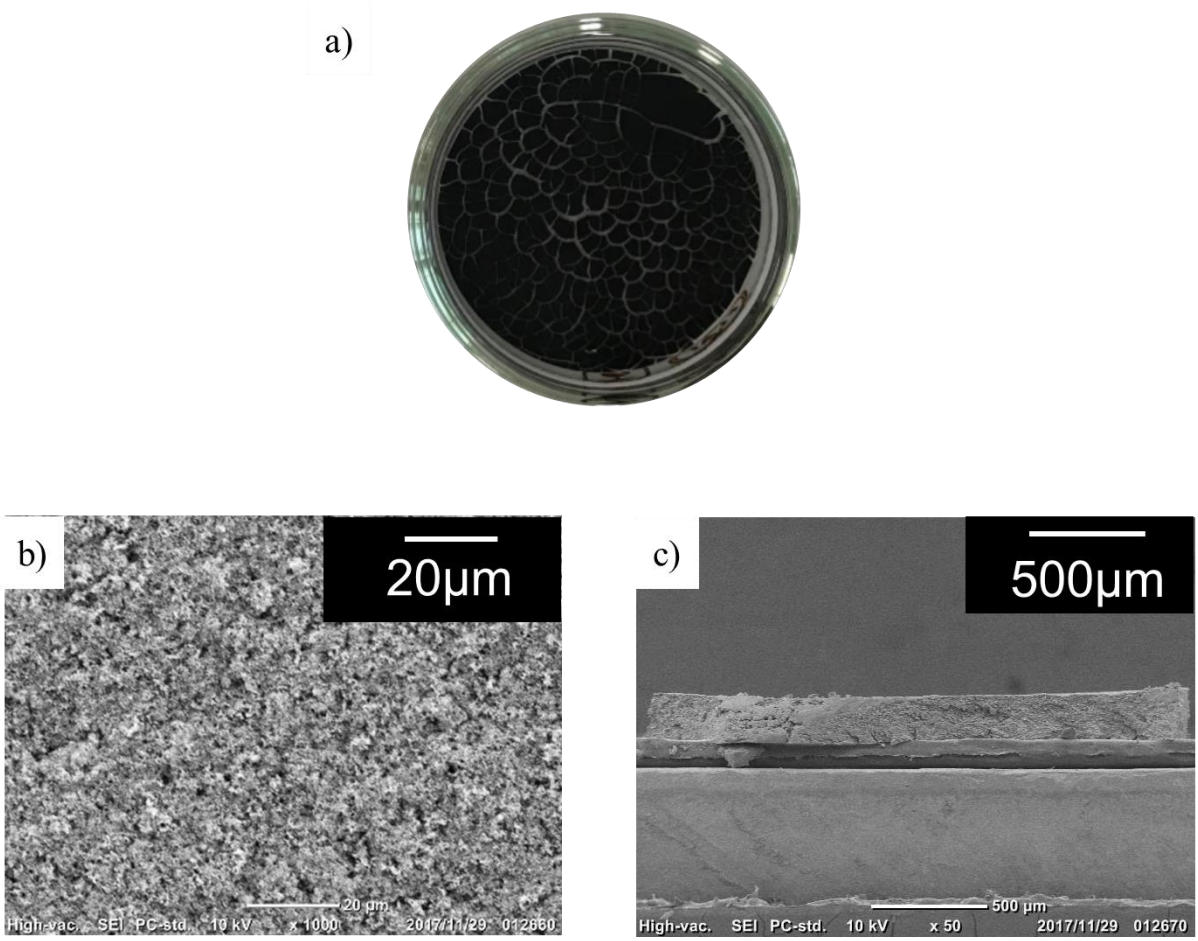

Figure 4.14 CB electrode made by an evaporation method (C-6): a) Top view, b) surface SEM, and c) cross-section SEM images

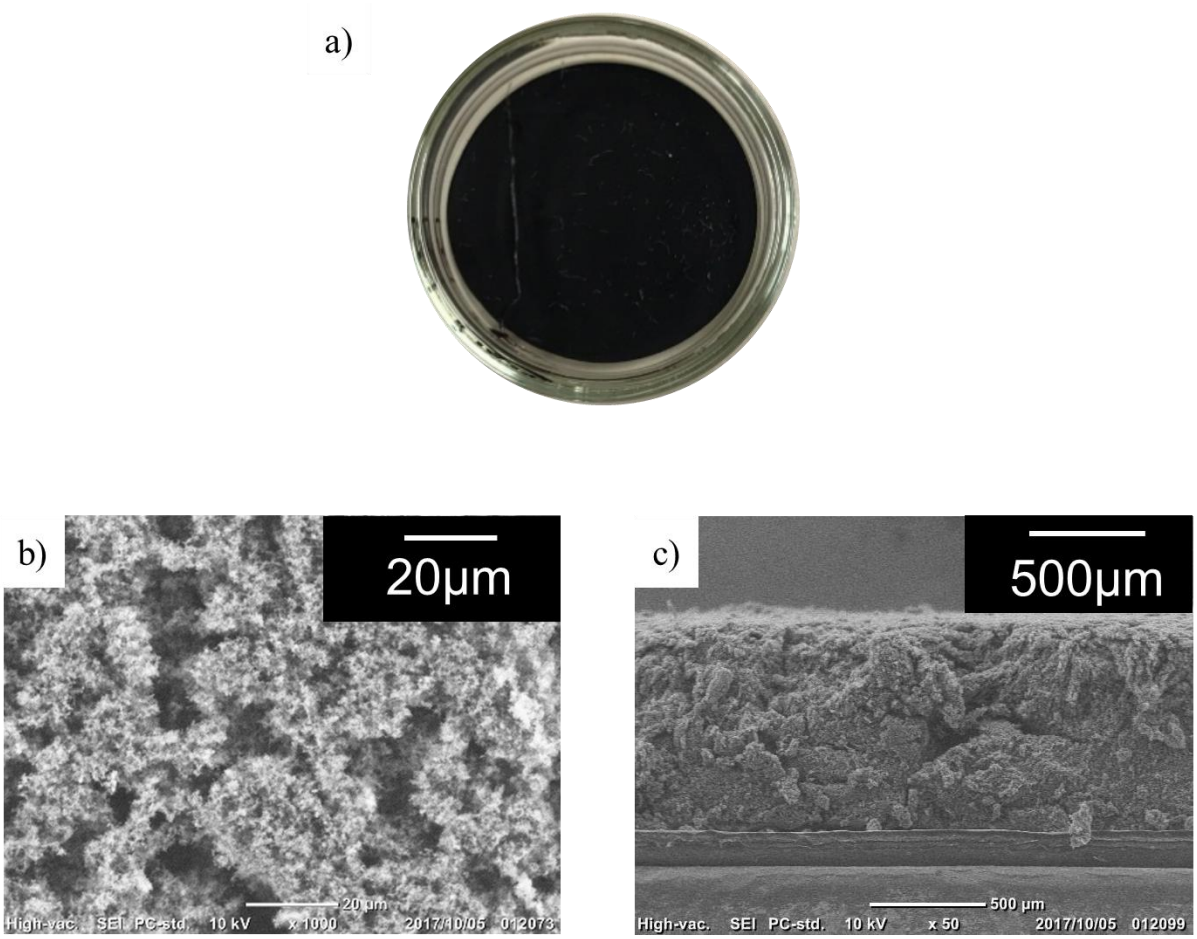

Figure 4.15 CB electrode fabricated by supercritical method at 40 °C (C-7): a) Top view, b) surface SEM, and c) cross-section SEM images

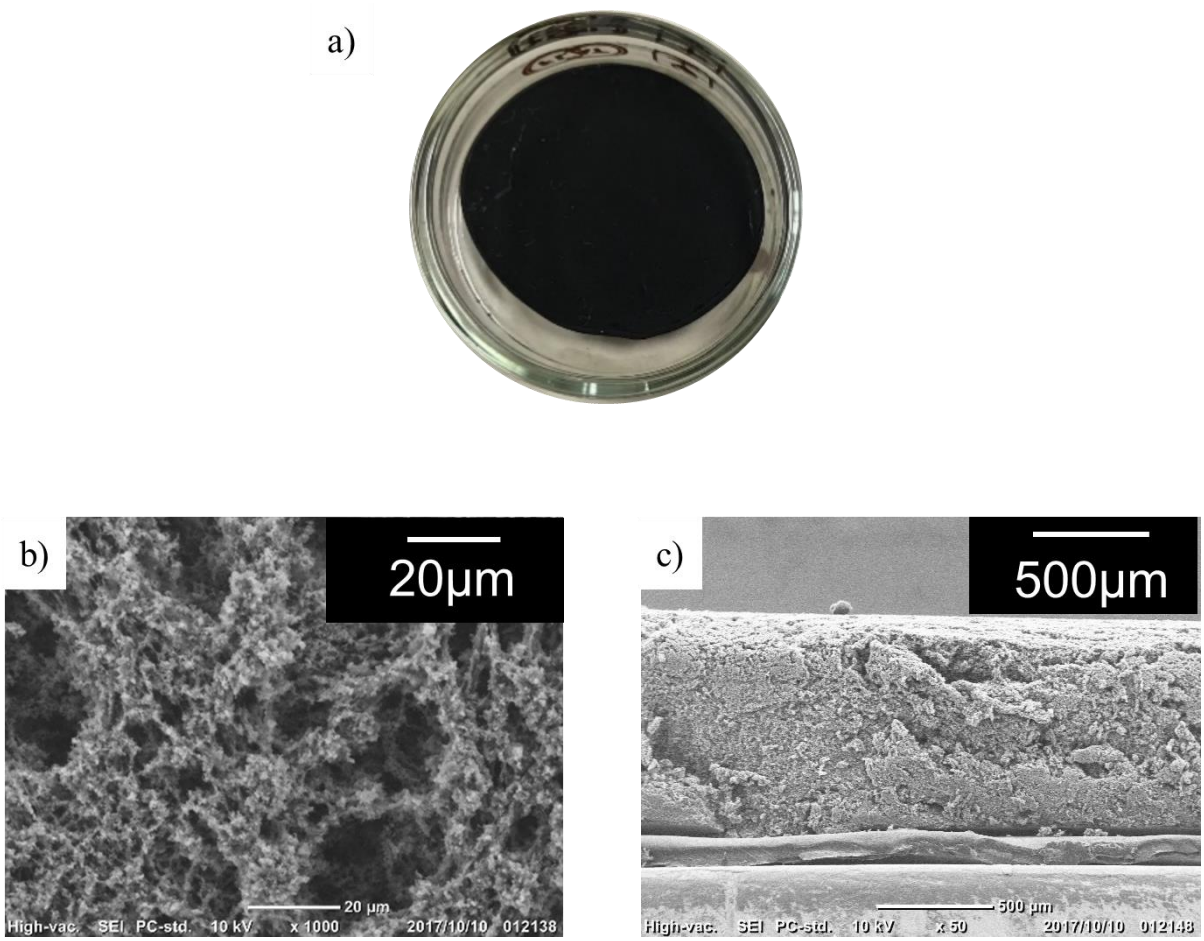

Figure 4.16 CB electrode fabricated by supercritical method at 60 °C (C-8): a) Top view, b) surface SEM, and c) cross-section SEM images

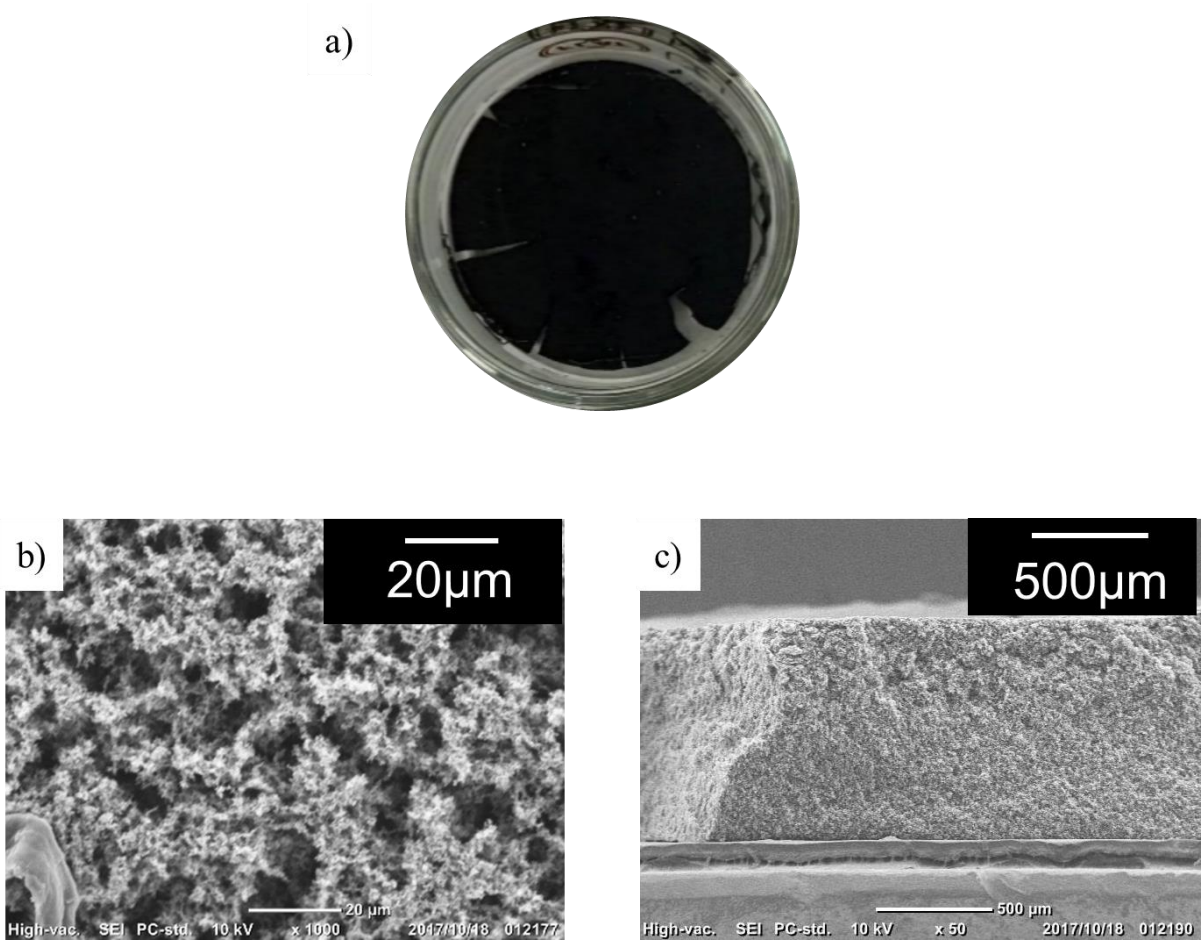

Figure 4.17 CB electrode fabricated by supercritical method at 80 °C (C-9): a) Top view, b) surface SEM, and c) cross-section SEM images

Table 4.6 Porosity calculation of each electrode fabricated in various temperature

Sample No.	Mass (g)	Top area (cm^2)	Thickness (mm)	Total volume (cm^3)	Density (g cm^{-3})	Void volume (cm^3)	Porosity
C-6	0.091	7.020	1.989	0.140	0.655	0.090	0.647
C-7	0.091	7.587	9.267	0.703	0.130	0.654	0.930
C-8	0.091	7.169	8.802	0.631	0.145	0.582	0.922
C-9	0.092	7.210	9.510	0.686	0.134	0.636	0.928

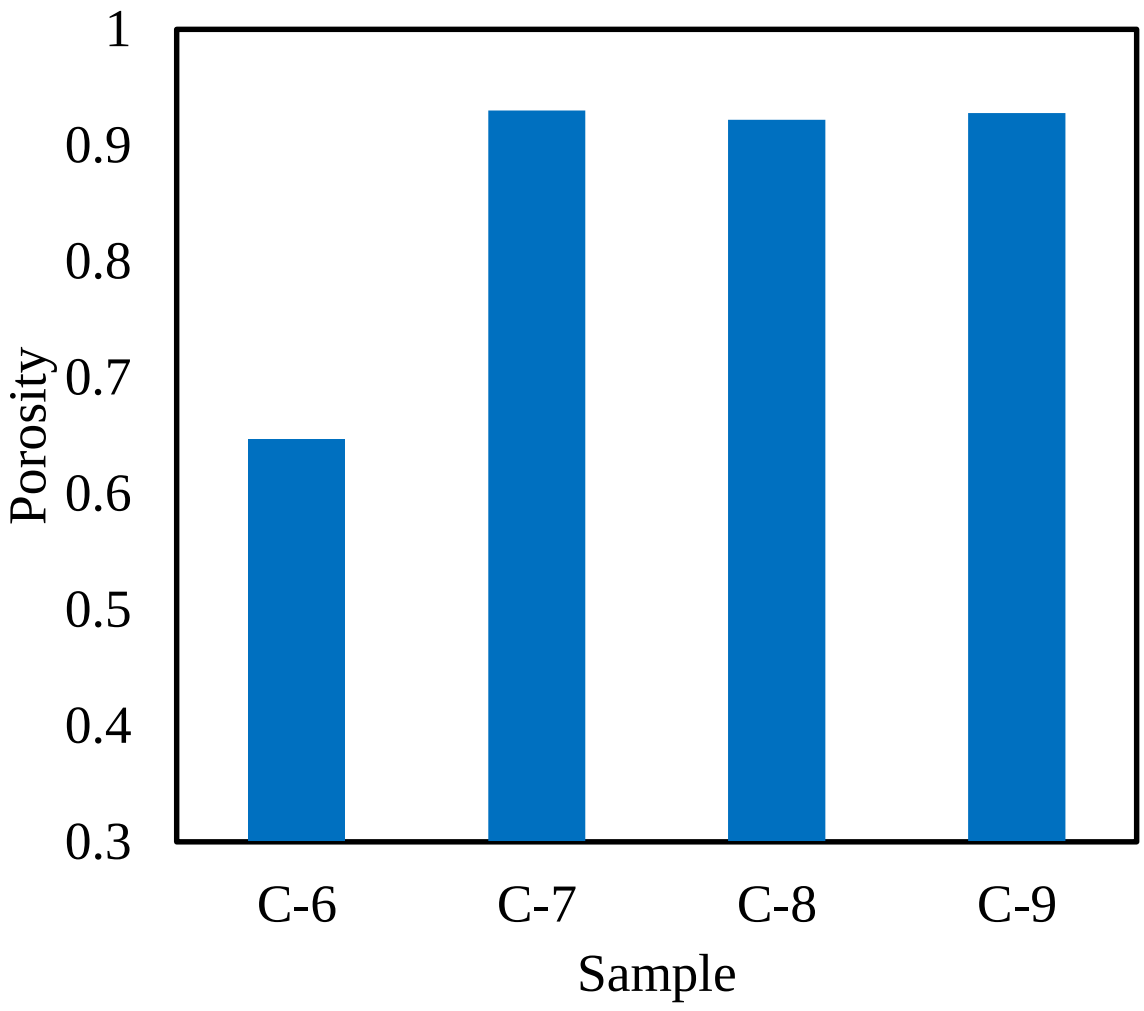

Figure 4.18 Porosity of CB electrode fabricated at various temperatures

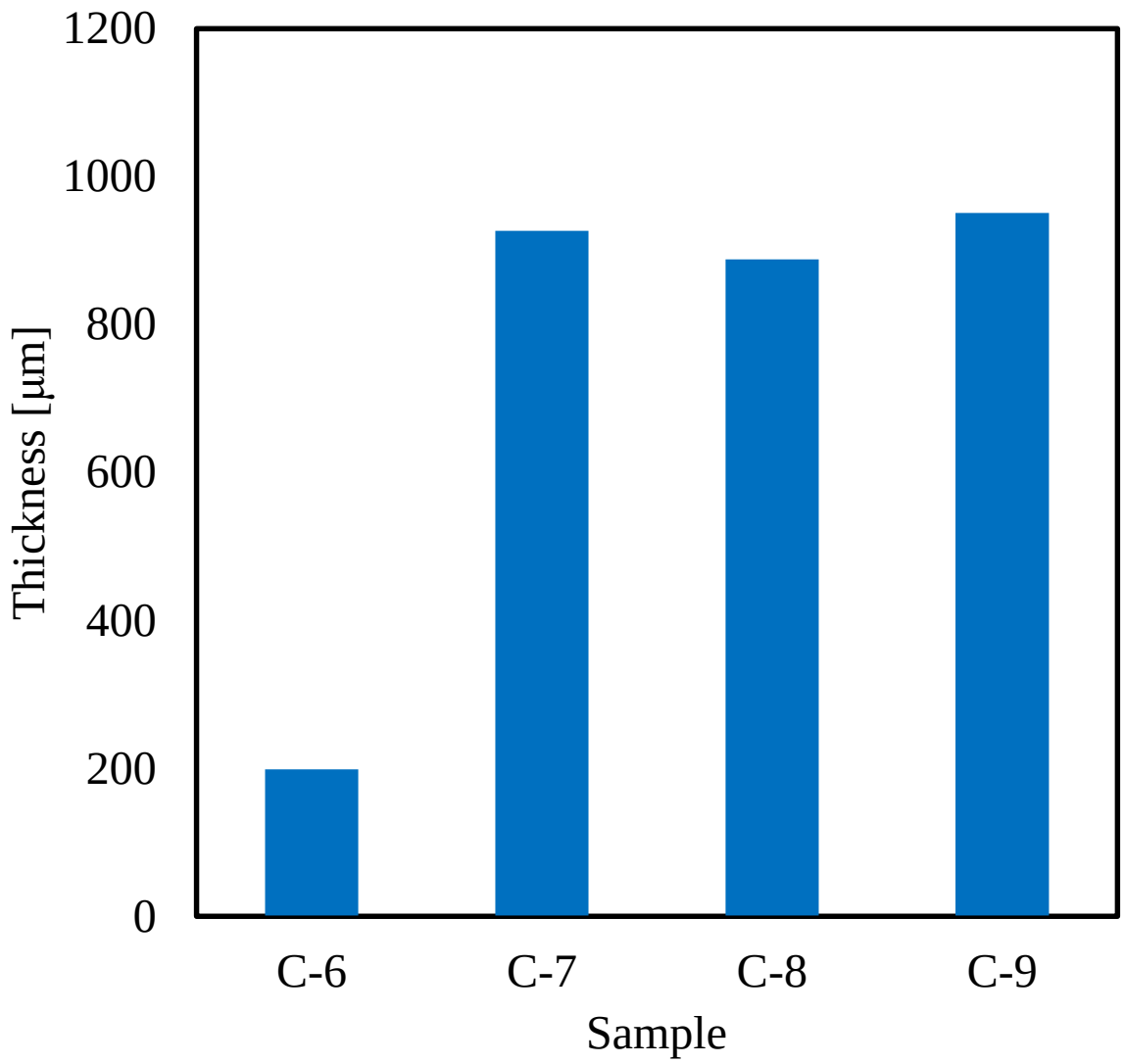

Figure 4.19 Thickness of CB electrode fabricated at various temperatures

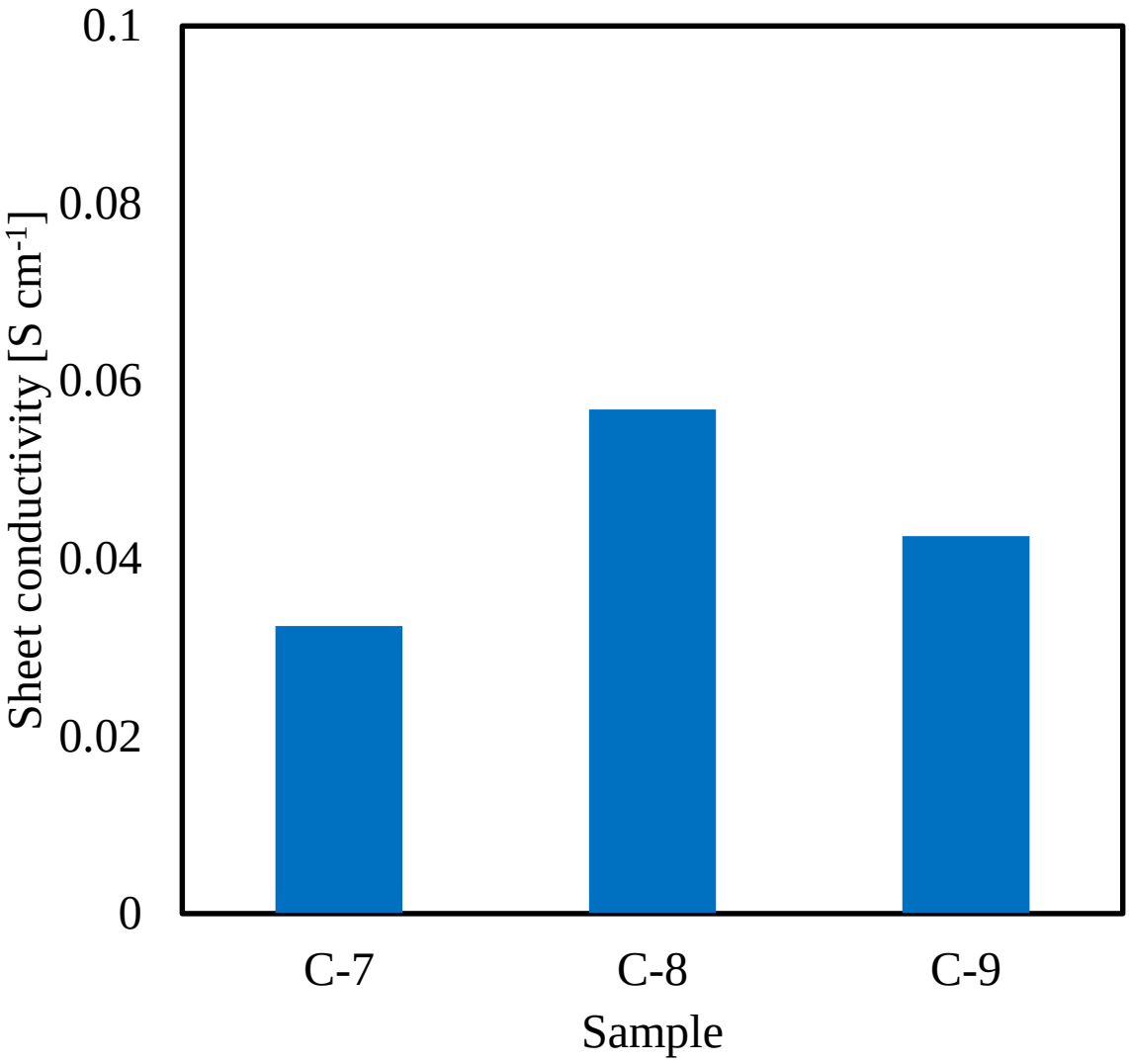

Figure 4.20 Sheet conductivity of CB electrode fabricated at various temperatures

4.3.3 CNF and CB electrode comparison

In this section, electrodes using two kinds of conductive materials were used to understand the effect of material structure on an electrode. In this section, the powder type was represented by CB, and CNF represented the long (fiber) type. The summary of electrode compositions is shown in Table 4.7. The table shows that the electrode consists of only CB, a mixture of CB with CNF, and only CNF. C-10 is a CNF electrode dried by evaporation drying. C-5 is the CB electrode which was already shown in section 4.3.1. C-11 and C-12 consist of both CB and CNF with different ratios. Finally, C-13 is a CNF electrode. In section 4.3.1, the highest porosity is when the ratio of CB:PVDF:NMP is 1:1:32. In section 4.3.2, the temperature does not significantly affect porosity. Thus, in this section, the ratio of conductive materials (CB/CNF), PVDF, and NMP were kept for 1:1:32. Furthermore, C-5, C-10, C-11, C-12, and C-13 were dried by supercritical drying at 40 °C and 20 MPa.

Next, the top view, cross-section, and surface SEM images of the electrodes are shown in Figure 4.21, Figure 4.10, Figure 4.22, Figure 4.23, and Figure 4.24. The top view image of CNF electrode C-10 (Figure 4.21) dried by evaporation shows different characteristics with CB electrode C-1 and C-6 (Figure 4.6 and Figure 4.14), where the CNF electrode is not damaged by the evaporation drying method because CNF which structure is fiber entangled together and this can prevent the electrode from being broken. This behavior proves CNF is superior to CB in strength [12]. However, from cross-section SEM images, it is clear that the CNF electrode made by evaporation drying (C-10) is significantly thinner than the other electrodes made by supercritical drying. Furthermore, from the surface SEM image of C-10 in Figure 4.21, aggregation was found, while no aggregation was found in other electrodes (C-5, C-11 to C-13).

From the top view images of Figure 4.22, Figure 4.23, and Figure 4.24, the surface area is more significant when the electrode contains more CNF because CB black slurry has a gel-like solution while CNF black slurry is a sol-like solution. From the surface SEM images of C-11 to C-13 (Figure 4.22 to Figure 4.24), a fiber-like structure is evident in electrodes containing CNF, even for a small amount. While Figure 4.10 for C-5 does not contain any CNF, a fiber-like structure cannot be observed.

The porosity calculation of CB/CNF electrodes and the graph are shown in

Table 4.8 and Figure 4.25, respectively. From the table and graph, each electrode has quite similar porosity except for CNF electrode C-10, which is made by evaporation drying, where this electrode has the lowest porosity. This low porosity is identical to the previous section, where evaporation drying has surface tension and capillary stress, making the pores inside the electrode collapse during drying. Figure 4.26 shows the thickness of the CB/CNF electrode where the thickness is smaller with more CNF contained inside the electrode. However, regardless of its thinner structure, the CNF electrode still has high porosity similar to the CB electrode. Because despite CNF electrode is thin, it has a larger surface area than the CB electrode. This complimentary thickness and surface area make the porosity stay large.

Now, the sheet conductivity of CB/CNF is shown in Figure 4.27. Again, high sheet conductivity is measured for C-11 and C-12 electrodes containing both CB and CNF, while the electrode containing either CB or CNF has small sheet conductivity, and electrode C-13 containing only CNF has the smallest value. This result is because an electrode containing only CNF has a fiber-like structure, and when combined with a binder, these fibers will form a net-like structure. Because of this net-like structure, the contact points between fibers are limited; thus, the electric conductivity is low. However, by combining the fiber-like structure of CNF with the powder-like structure of CB, the powder-like structure can fill in the space in the net structure. As a result, a higher sheet conductivity can be achieved.

Table 4.7 Summary of electrode using CB and/or CNF as conductive materials

Electrode No.	CB : CNF : PVDF : NMP (g/g/g/g)	Drying condition		
		Method	Temperature (°C)	Pressure (MPa)
C-10	0 : 1.0 : 1.0 : 32	Evaporation	80	0.1
C-5	1.0 : 0 : 1.0 : 32	Supercritical drying	40	20.0
C-11	0.91 : 0.09 : 1.0 : 32			
C-12	0.5 : 0.5 : 1.0 : 32			
C-13	0 : 1.0 : 1.0 : 32			

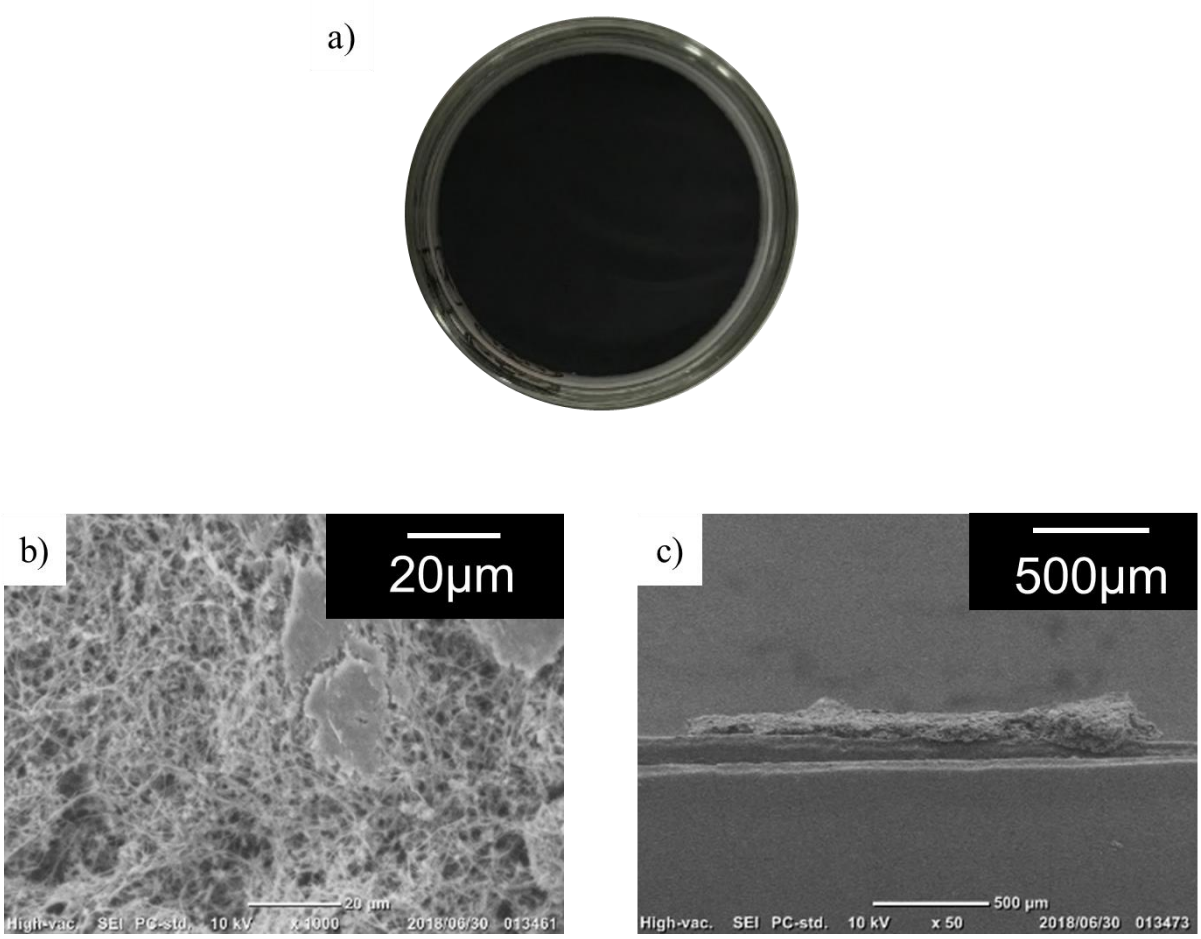

Figure 4.21 CNF electrode fabricated by evaporation drying (C-10): a) Top view images, b) surface SEM images, and c) cross-section SEM images

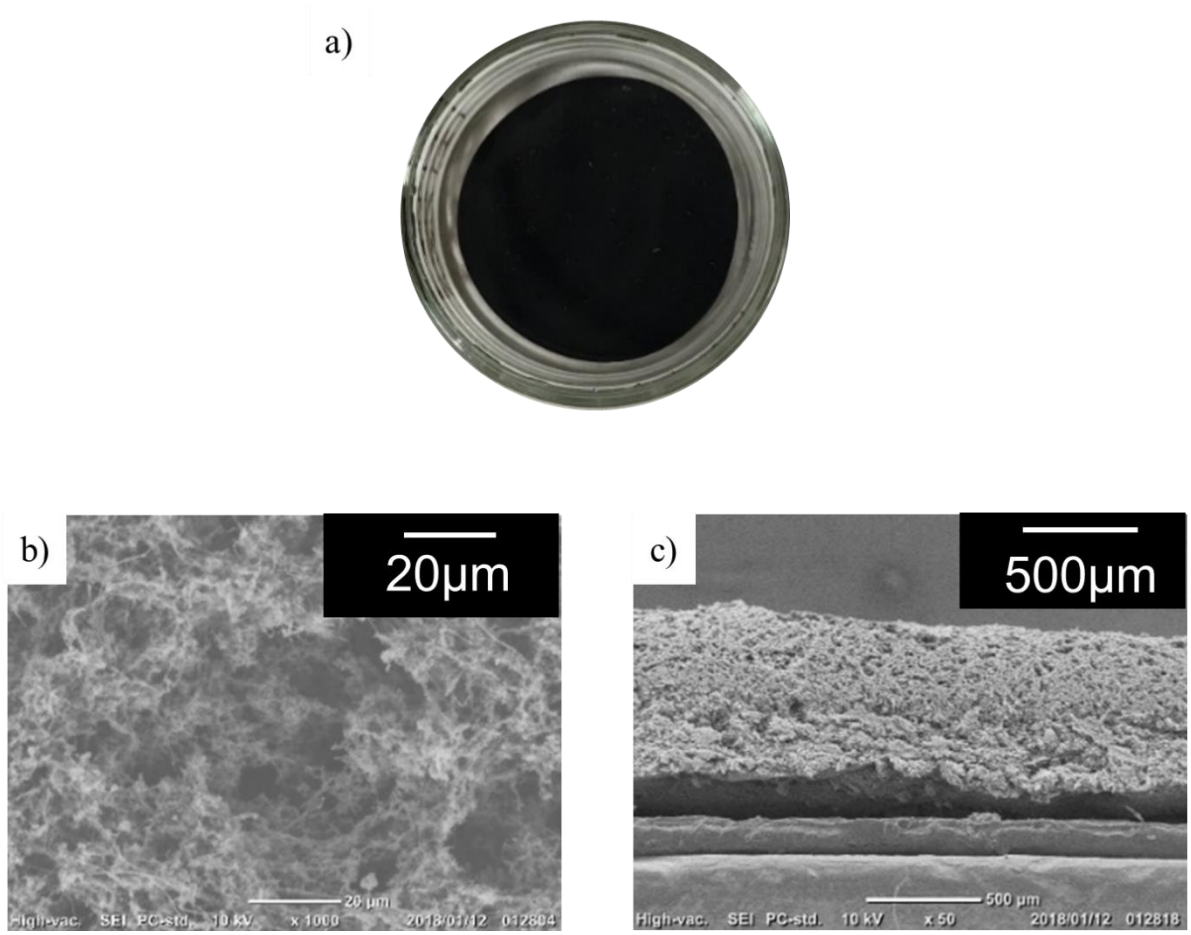

Figure 4.22 CB/CNF electrode fabricated by supercritical drying (C-11): a) Top view images, b) surface SEM images, and c) cross-section SEM images

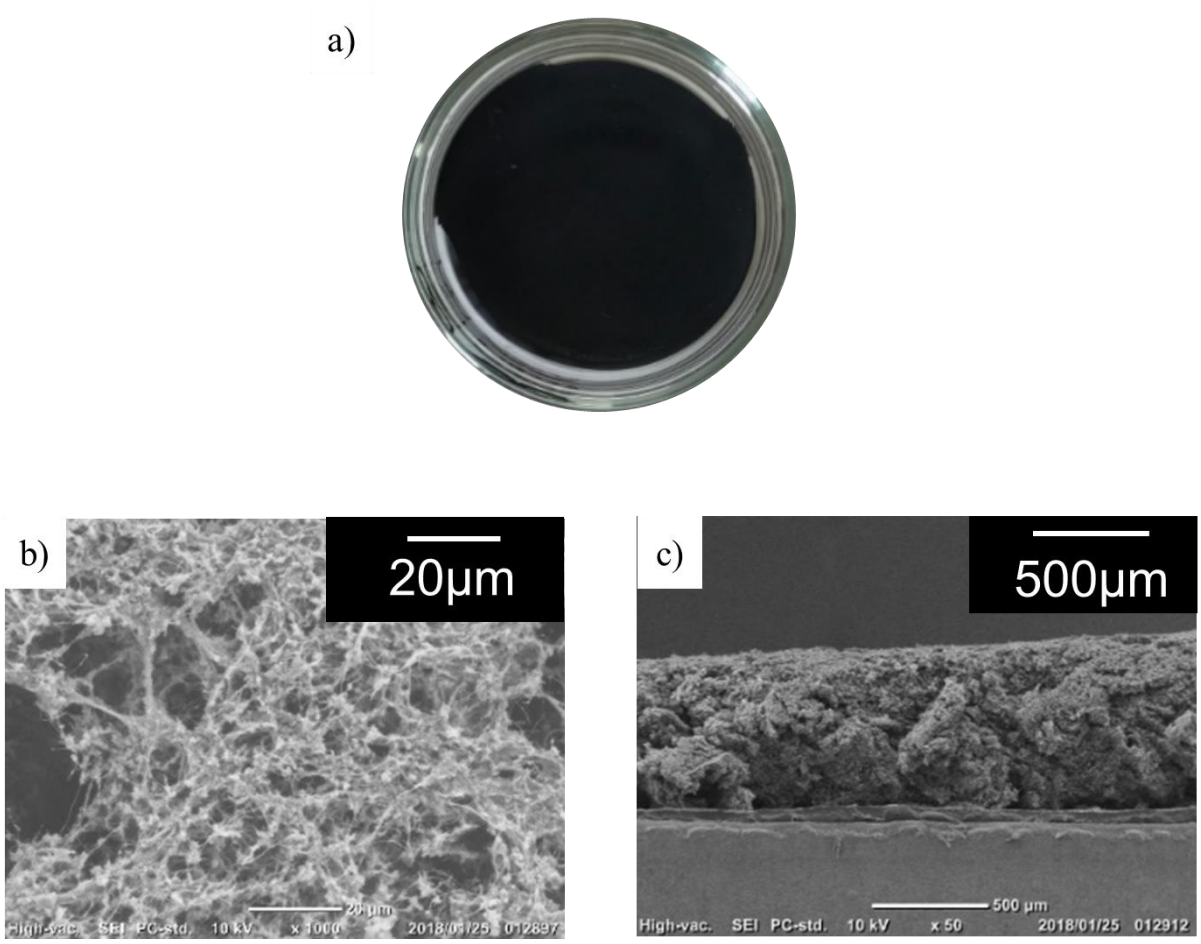

Figure 4.23 CB/CNF electrode fabricated by supercritical drying (C-12): a) Top view images, b) surface SEM images, and c) cross-section SEM images

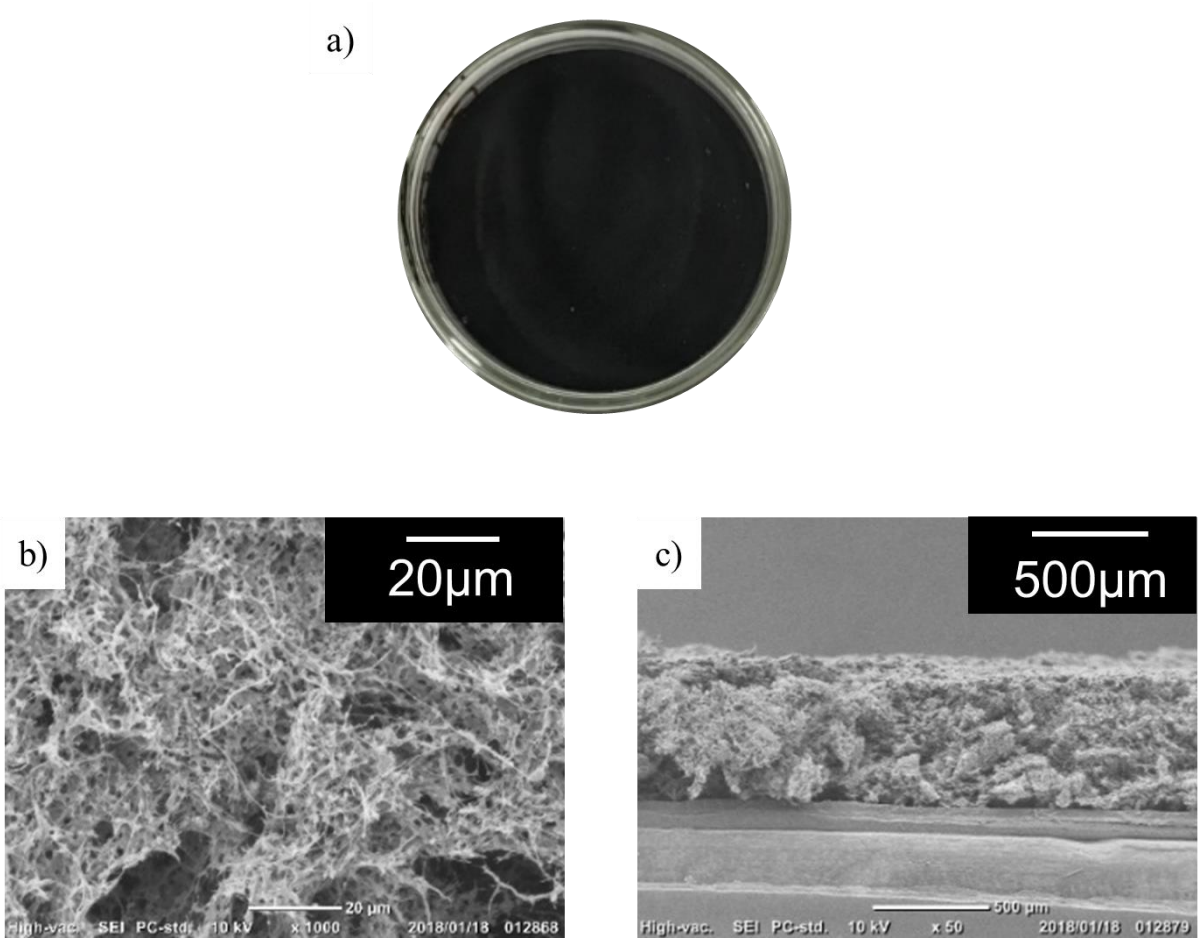

Figure 4.24 CNF electrode fabricated by supercritical drying (C-13): a) Top view images, b) surface SEM images, and c) cross-section SEM images

Table 4.8 Porosity calculation of CB/CNF electrodes

Sample No.	Mass (g)	Top area (cm^2)	Thickness (mm)	Total volume (cm^3)	Density ($g\ cm^{-3}$)	Void volume (cm^3)	Porosity
C-10	0.059	8.978	1.267	0.114	0.520	0.080	0.705
C-5	0.059	6.838	10.028	0.686	0.086	0.654	0.953
C-11	0.059	6.574	7.989	0.525	0.112	0.493	0.938
C-12	0.059	8.288	7.787	0.645	0.092	0.613	0.950
C-13	0.059	8.710	5.919	0.516	0.115	0.483	0.937

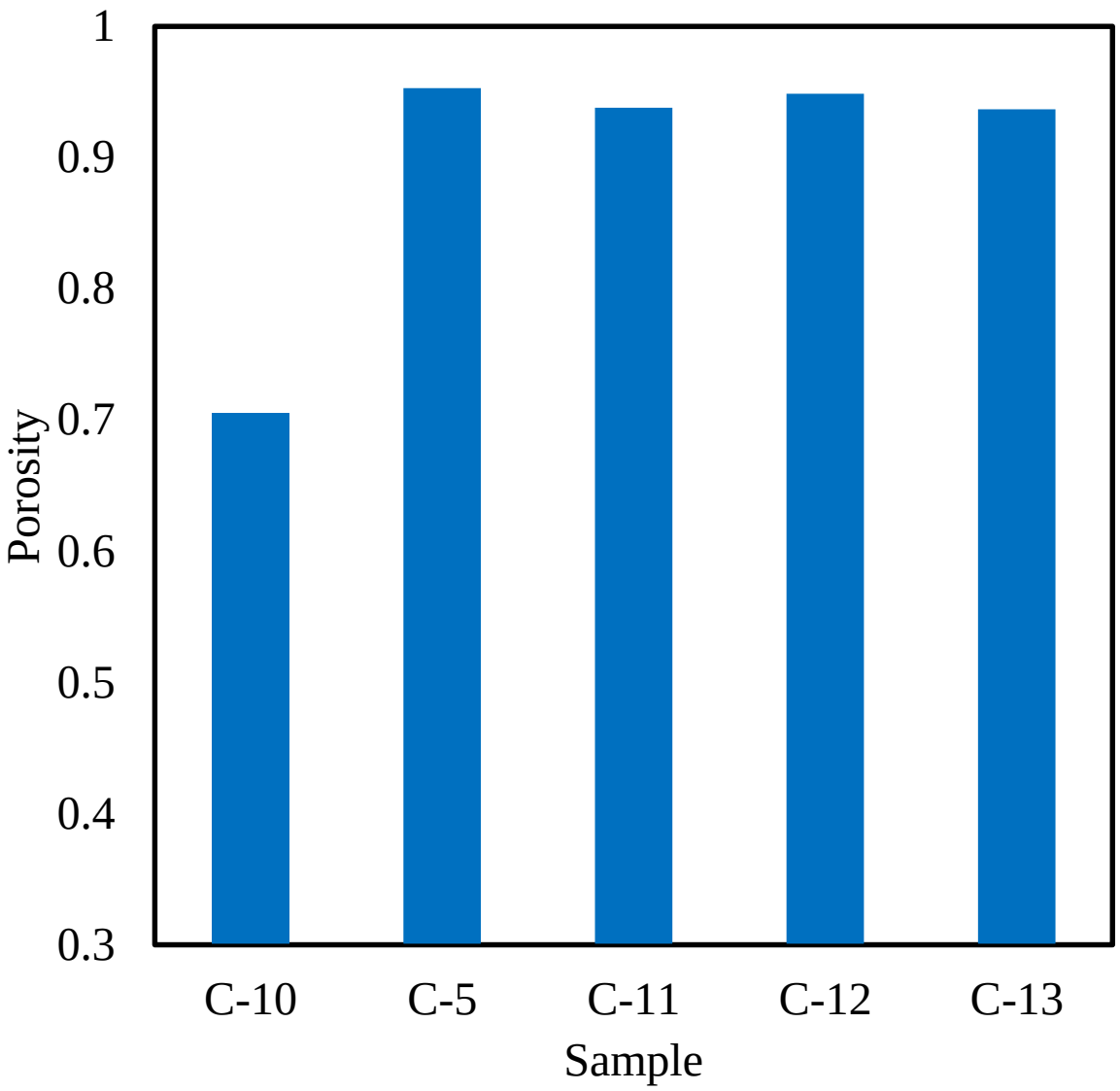

Figure 4.25 Porosity of CB/CNF electrode fabricated with different CB and CNF composition

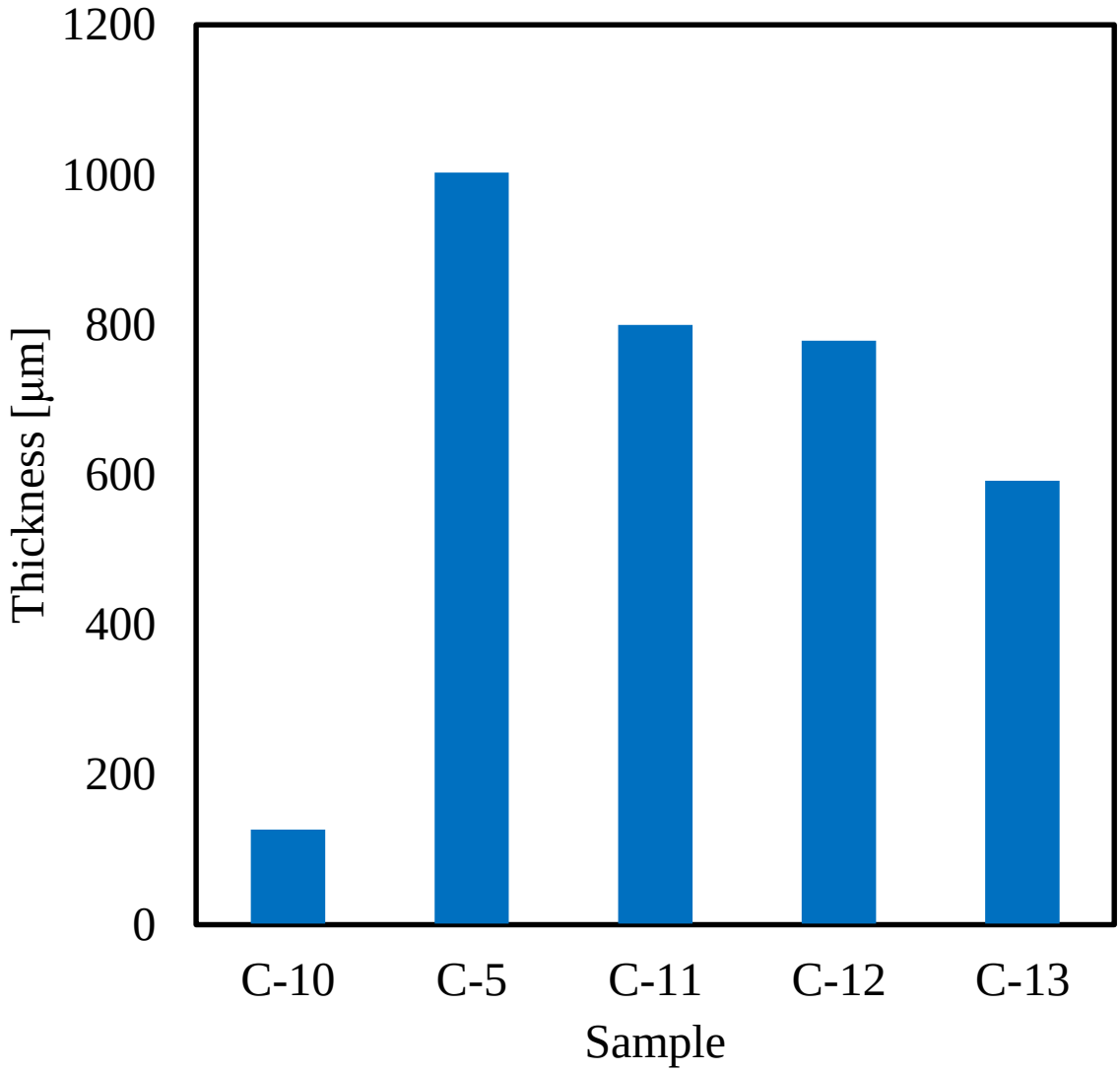

Figure 4.26 Thickness of CB/CNF electrode fabricated with different CB and CNF composition

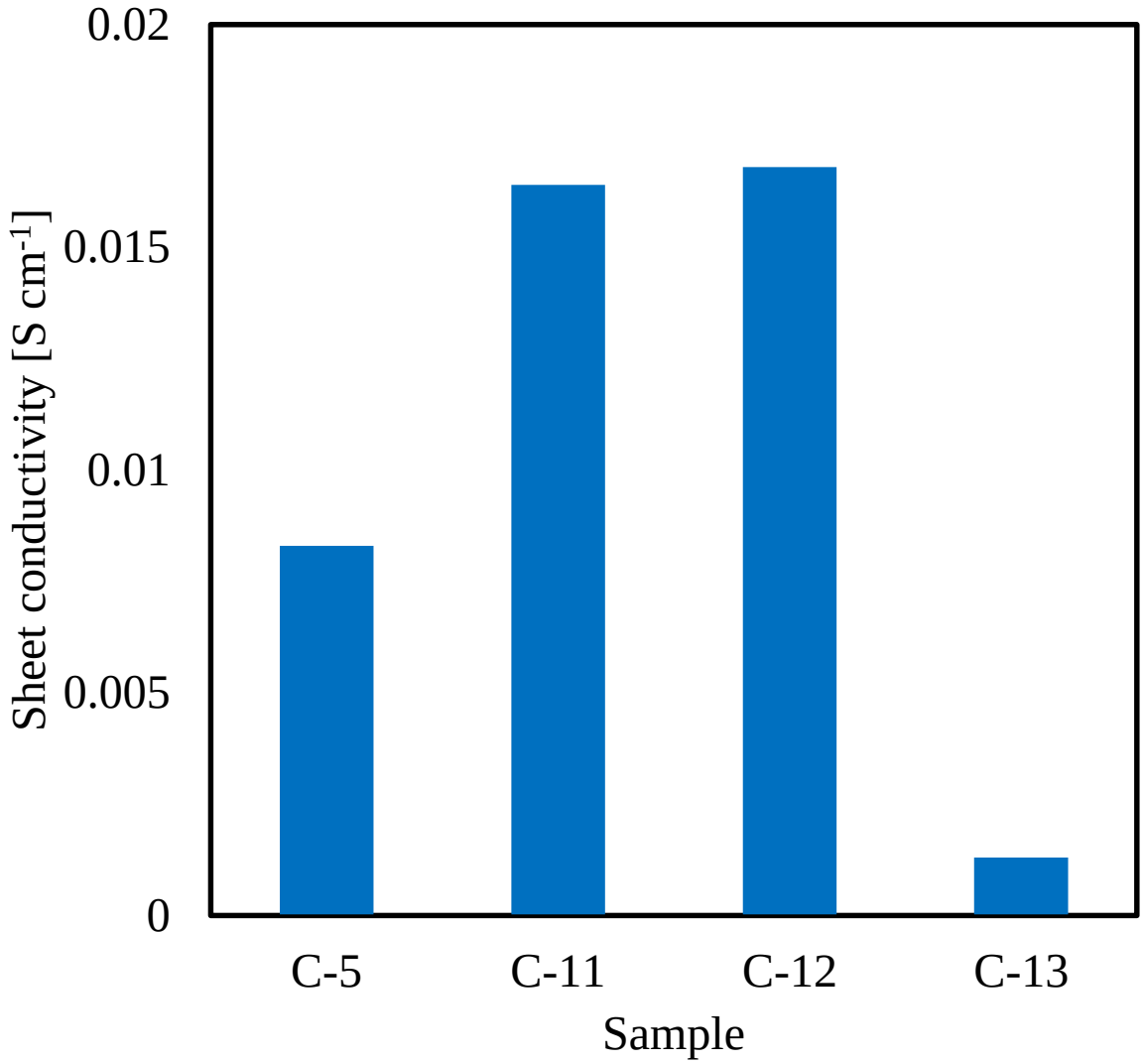

Figure 4.27 Sheet conductivity of CB/CNF electrode fabricated with different CB and CNF composition

The following experiment is battery testing using carbon aerogels as carbon electrodes. In this case, specific capacity and battery cycle were investigated. Figure 4.10 shows the specific capacity of the battery using the CNF electrode (green) compared to the CB/CNF electrode (blue) and CB electrode (red). Battery using CNF electrode presents the most superior specific capacity with the value of 7.75 mA h cm^{-2} than the other batteries, which is approximately 2.6 times compared to the battery using CB electrode. While the electrode with CB and CNF mixed gives a specific capacity value between batteries using CB and CNF electrodes. Initially, the CB shape is like particles for the CB electrode, while CNF has a shape like fiber or thread. The SEM images of the CB and CNF surface are shown in Figure 4.11 a and b. When CB particles were bonded with PVDF, PVDF covered the surface of CB to stick the particles. This structure makes O_2 and CO_2 gases and Li-ion to be more challenging to reach the CB surface to react. On the other hand, while PVDF bonded CNF fibers, many fiber surfaces are still exposed, which makes gases and Li-ion easier to react on the surface of the electrode. This mechanism is illustrated in Figures 4.11 c and b.

Battery with CNF electrode was discharged and charged ten times where the measurement range was 0 - 0.5 mA h cm^{-2} and the electric current was 0.1 mA (0.0750 mA cm^{-2} cathode). As a result, this battery could withstand ten cycles, while the battery with the CB electrode fell after five cycles, as shown in Figure 4.12. This result means that CNF is superior to CB as an electrode.

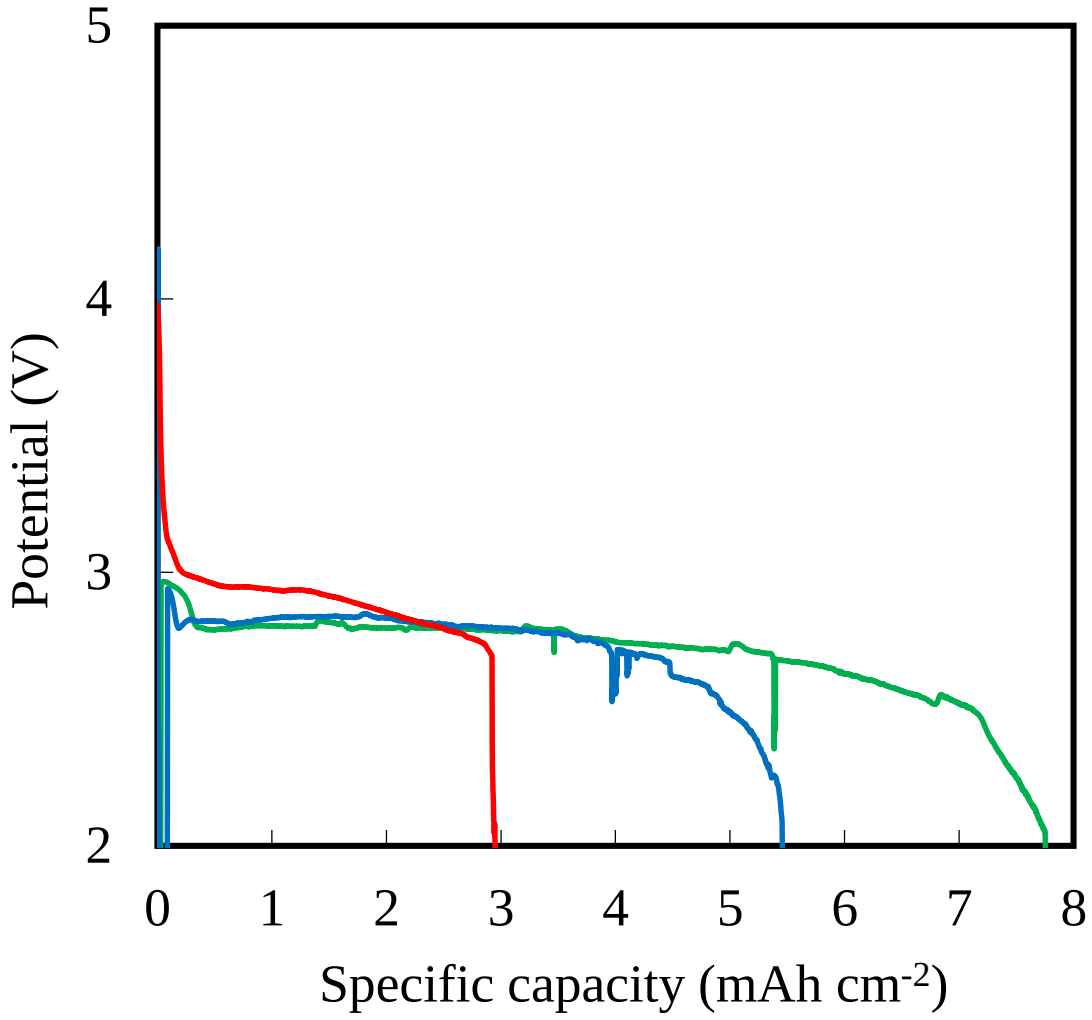

Figure 4.28 Specific capacity of carbon nanofiber electrode (green) compared to carbon black/carbon nanofiber (blue) and carbon black electrode (red)

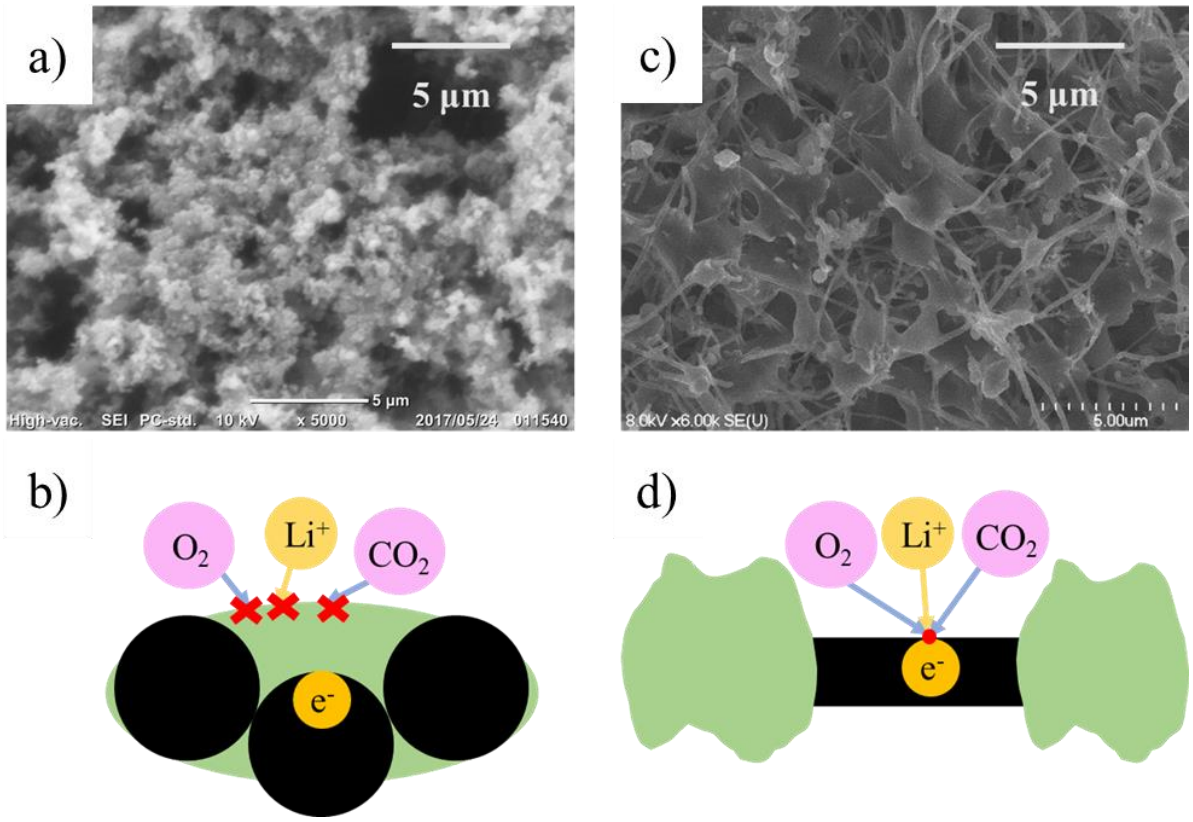

Figure 4.29 Illustration of carbon black: a) SEM, b) mechanism and carbon nanofiber electrode: c) SEM, d) mechanism

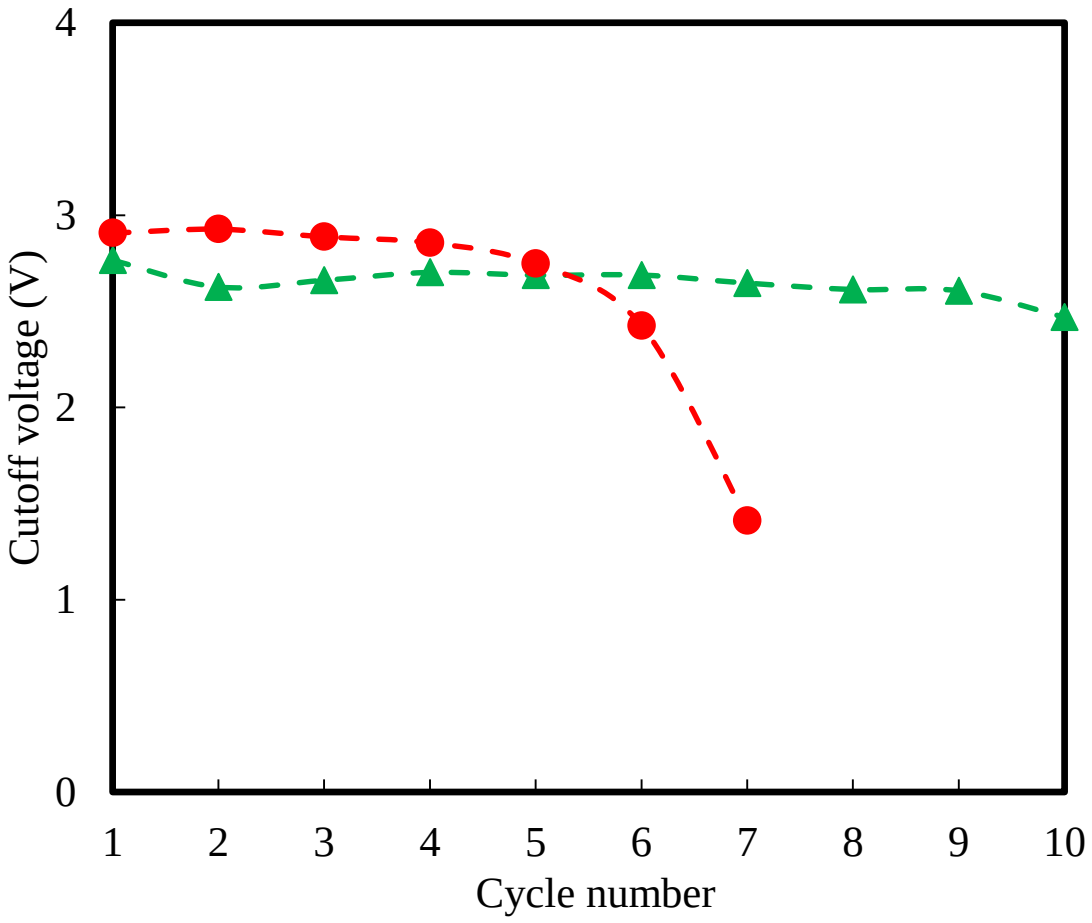

Figure 4.30 Cyclability of carbon nanofiber (green) and carbon black electrode (red)

4.4 Reference

[1] Shofiyah Sakinah, Nattanai Kunanusont, Yusuke Shimoyama, "Carbon Nanofiber Aerogel Fabricated by Supercritical Drying and Application in Li–O_2/CO_2 Battery", *JOURNAL OF CHEMICAL ENGINEERING OF JAPAN* 54 (2021) 239-247

[2] Shahzamani, Rouhollah Bagheri, Mahmood Masoomi, Majid Haghgoo, Akram Dourani, "Effect of drying method on the structure and porous texture of silica-polybutadiene hybrid gels: Supercritical vs. ambient pressure drying", *Journal of Non-Crystalline Solids* 460 (2017) 119-124

[3] Danae A. Voormeij and George J. Simandl, "Geological and Mineral CO2 Sequestration Options: A Technical Review", *Geological Fieldwork 2002* 1 (2003) 265-275

[4] Kunanusont, Nattanai, and Yusuke Shimoyama, "Porous carbon electrode for Li-air battery fabricated from solvent expansion during supercritical drying", *The Journal of Supercritical Fluids* 133 (2018) 77-85

[5] F. M. Smits, "Measurement of Sheet Resistivities with the Four-Point Probe", *The Bell System Technical Journal* 37 (1958) 711 – 718

[6] Nattanai Kunanusont, "Master dissertation", Tokyo institute of technology, Tokyo (2017)

[7] Shengxuan Zheng, Xiaohui Hu, Abdul-Rauf Ibrahim, Daoying Tang, Yuquan Tan, and Jun Li, "Supercritical Fluid Drying: Classification and Applications", *Recent Patents on Chemical Engineering* 3 (2010) 230 – 244

[8] Kultayeva, Shynar, Ha, Jang, Malik, Rohit, Kim, Young, and Kwang J. Kim, "Effects of porosity on electrical and thermal conductivities of porous SiC ceramics", *Journal of the European Ceramic Society* 40 (2020) 996-1004

[9] McKeen, Laurence W, "Solvent Systems", *Fluorinated Coatings and Finishes Handbook (Second Edition)* (2016) 107-118

[10] Saïdi, Sami, Aymen, Mannai, Bouzitoun, Mouna, and Abdelatif B. Mohamed, "Effect of α- to β-transformation on the dc and ac conductivity mechanism in polyaniline: Polyvinylidene fluoride composites films", *Materials Science in Semiconductor Processing* 26 (2014) 336-342

[11] Raghunandan Sharma & Kamal K. Kar, "Characteristics of Carbon Nanofibers", *Handbook of Nanocomposite Supercapacitor Materials I. Springer Series in Materials Science* 300 (2020)

Chapter 5 Improvement of carbon electrode using acetone as the solvent

5.1 Statement of problems and objectives

As mentioned in chapter 1, to further improve the performance of the Li-air battery, the results of Chapter 3 and Chapter 4 are combined to optimize the electrode production, which is later applied to the battery. In this case, from Chapter 3, acetone has the highest expansion rate compared to the other solvents. Using acetone as the solvent hopefully can increase the porosity of the electrode and improve the battery performance. From Chapter 4, the optimum electrode composition for higher porosity is when CB:PVDF:NMP is 1:1:32. Furthermore, the optimum drying temperature is 40 °C, and CNF as conductive material can improve the battery-specific capacity and cycle. The experiment of Chapter 5 was conducted using these pieces of information.

5.2 Experimental

5.2.1 Materials

As in Chapter 4, the experiment is separated into two parts: manufacturing the electrode and applying the electrode into a CO_2/O_2 battery. This chapter's materials are similar to those in section 4.2.1. From the previous chapter, the experiment demonstrates that the electrode containing carbon nanofiber outperforms the black carbon electrode. As a result, the only conductive substance used in this chapter was carbon nanofiber (CNF, purity 98 %) that was bought from Pyrograf Products, Inc. Next, the carbon particles were bonded with a binder, poly(vinylidene fluoride) (PVDF) from Fluorochem. Then, 1-Methyl-2-pyrrolidone (NMP, purity higher than 99.0 %), Cellulose acetate (CA, purity 100%), and acetone (purity higher than 95 %) were purchased from Fujifilm Wako. NMP and acetone were used as solvents. CA was used as binder in addition to PVDF. Figure 5.1 shows the molecular structure of CA, while NMP and acetone molecular structures were depicted in Figure 3.1, Then, Figure 4.1 displays the CNF picture and the molecular structure of PVDF.

The second stage of the experiment involves putting the manufactured electrodes into CO_2/O_2 batteries. Lithium bis(trifluoromethylsulfonyl) imide (LiTSFI) was supplied by Wako Pure Chemical Ind. Ltd. for the battery, which was employed as Li-salt in the electrolyte. In addition, the electrolyte was dimethyl sulfoxide (DMSO), obtained from Wako Pure Chemical

Ind. Ltd. For the supercritical drying process, carbon dioxide with a purity of 99.5 % mass was bought from Fujii-Bussan to fabricate the electrode under supercritical drying and for CO_2/O_2 batteries.

5.2.2 Fabrication of electrodes

5.2.2.1 Preparing black slurry

A black slurry mentioned in this chapter contains CNF as a conductive material, a binder (PVDF or CA), and a solvent (NMP or acetone). The summary of the electrode compositions is shown in Table 5.1.

For fabricating sample CA-0, PVDF was put into a vial filled with NMP as the starter. Then, the binder was completely dissolved in the solvent with ultrasonication help at 60 °C. Then, CNF was added to the solution and mixed with ultrasonication for an hour. Black slurry fabrication was followed by adding acetone to the mixture. Finally, the mixture was left for a night while stirred with a magnetic stirrer.

Then, the same as CNF/PVDF electrode fabrication method, CNF/CA (CA-1 to CA-7) samples were produced. First, CA is added into acetone in a vial and ultra-sonicated under 30 °C until it is completely dissolved. In the case of CNF/PVDF black slurry, PVDF was dissolved under 60 °C. However, acetone has a low boiling point; thus, to prevent acetone evaporation, acetone was dissolved at 30 °C. Then, CNF was added to CA/acetone solution. Next, this solution was ultra-sonicated for an hour and stirred with a magnetic stirrer for a night to homogenize CNF in the solution. The summary of the black slurry compositions is shown in Table 5.1.

5.2.2.2 Drying black slurry

In a petri dish with an inner diameter of 34 mm, 1 gram of homogenized black slurry is poured. Then, the petri dish was tapped to make the surface of the slurry even. The slurry is then dried using one of two methods: evaporation or supercritical drying. Evaporation or thermal drying is the process of drying materials by continual heating under atmospheric pressure until the solvent in the material is completely evaporated, and the products are commonly referred to as xerogel [1]. For evaporation drying, the CNF/PVDF and CNF/CA slurries were dried in a thermostat at 80 and 40 °C for 24 hours, respectively, to guarantee no solvent remained. Because acetone has a low boiling point, CNF/CA was dried at 40 °C.

The other process is supercritical drying, which is done under pressure and at temperatures higher than a fluid's critical point [2]. CO_2 is the fluid used in this process. The black slurry is dried using supercritical drying equipment for this process, as shown in Figure 4.2. CO_2's critical point is 31.1 °C and 7.38 MPa [3]. As a result, the experiment should be carried out at higher pressures and temperatures than those stated. This study was conducted at 20 MPa and 40 °C. The steps for supercritical drying black slurry are listed below.

Initially, a petri dish with black slurry was placed in a high-pressure cell as soon as possible to reduce evaporation and tightly closed to ensure no fluid was lost during the experiment. Next, the cell was placed in a thermostat set to the desired temperature and connected to stainless steel tubing. Next, the connectors between the cell and the line were tightly closed to keep the fluid from leaking. Finally, a back pressure used to control the pressure was set to the desired pressure.

The valves were confirmed to be closed before the experiment began. Then, at the start of the equipment, a CO_2 cylinder was opened, followed by the opening of the V1, V2, V4, and V5 valves. V4 was opened slowly to avoid a sudden pressure change inside the high-pressure cell. After CO_2 had filled the high-pressure cell and the pressure displayed on the pressure meter remained constant, the pump was turned on, causing the pressure to rise to the desired temperature. Later, valve V6 was opened, followed by the control valve or needle valve at the equipment's end being slowly opened. The flow rate of CO_2 was then adjusted by manipulating the control valve while watching the wet gas meter. The CO_2 flow rate was set at around 150 mL min^{-1}. A solvent trap was installed between the control valve and the wet gas meter to catch the solvent flowing out with the CO_2, reducing the likelihood of solvent entering the wet gas meter.

The pump was switched off, and the CO_2 cylinder was closed after drying. Drying was held for 6 hours for sample CA-0, where the solvent was a mixture of NMP and acetone, to verify that the NMP was removed entirely from the black slurry. Due to acetone's low boiling point, drying for CA-1 through CA-7, which contains only acetone as the solvent, took only 1.5 hours. In the preliminary experiment, electrodes were weighed after 1.5 hours of supercritical drying, and more than 99% of the solvent was eliminated. This result shows that 1.5 hours is sufficient for supercritical drying when using acetone as the solvent.

The high-pressure cell was depressurized by allowing CO2 to escape until the pressure meter's pressure returned to atmospheric pressure. By changing the control valve while

watching the wet gas meter, the flow rate of CO_2 was kept at roughly 200 mL min^{-1}. Finally, the high-pressure chamber was opened, and a petri dish containing aerogel (dry black slurry) was removed.

5.2.2.3 Preparing Li-O_2/CO_2 battery coin cell

The aerogel was cut into a circular electrode with a 13.0 mm diameter. The weight of the electrode was then determined using a balance. Before assembling the battery, 1 M LiTFSI/DMSO electrolyte was made by dissolving LiTSFI in DMSO. Then a glove box was filled with a coin cell casing, lithium metal, spacers, electrolyte, Whatman glass fiber, electrode, and gas diffusion layer (carbon fiber). The air in the glove box was then evacuated until the humidity level in the glove box was less than 5%. Humidity should be kept as low as feasible to prevent lithium metal from interacting with water vapor in the air. The glove box was soon filled with argon gas. Finally, the battery was built inside the glove box in the following order: coin cell case, lithium metal, LiTFSI/DMSO electrolyte on Whatman glass fiber, electrode, spacers, and coin cell case, as shown in Figure 4.3. The constructed battery was soon transferred to a crimping machine to be closed. Then it was taken from the glove box.

5.2.3 Analysis

5.2.3.1 Morphology investigation

The morphology of carbon electrodes was studied using a scanning electron microscope (SEM) (JSM-6000 Plus, JEOL). The top surface and the electrode cross-section were the objects analyzed.

5.2.3.2 Porosity and pore volume measurement

Porosity measurements were performed to establish the differences in aerogel for various scenarios. To get the porosity value, first, compute the total volume of the aerogel by multiplying the top area by the thickness of the aerogel (Equation 4.1).

The top area and thickness of the aerogel were measured using ImageJ, an image analysis software. First, a bird's-eye view of the top section of the aerogel was captured. The image was then opened with the ImageJ program. The image was then converted to 8-bit and the threshold was changed to produce a black-and-white image. The top area was then determined using particle analysis in the software. Finally, the thickness was calculated using ImageJ by taking the average of the aerogel thickness from roughly 200 locations in 20 cross-section SEM pictures of an aerogel.

Furthermore, from Equation 4.2, the void volume of the aerogel was calculated by subtracting the bulk volume from the total volume of the aerogel. Next, this bulk volume was calculated by dividing the weight of solids (black slurry without solvents) by the density of those solids. Table 5.2 displays the densities of the solids. Finally, the porosity of an aerogel was estimated by dividing its void volume by its total volume (Equation 4.3).

In addition of porosity, in this chapter, pore volumes are also calculated. Pore volumes are calculated from the equation as follows by dividing the void volume which is obtained from Equation 4.2 with the electrode mass.

$$V_{pore} = \frac{V_{void}}{w_{solid}} \qquad \text{(Equation 5.1)}$$

Where, $V_{pore}\ (cm^3 \cdot g^{-1})$, $V_{void}\ (cm^3)$, $W_{solids}\ (g)$ are the pore and void volume of aerogel, the solids' weight, and the solids' density.

5.2.3.3 Capacity measurement

Only capacity measurement was performed in this chapter to compare the respective capacity of the battery employing CNF/PVDF and CNF/CA electrodes. First, the coin cell assembled in section 5.2.2.3 was placed in a coin cell holder in a glass jar, which was then connected to the potentiostat and galvanostat, which were used to determine the electrode capacity. The temperature within the cell box was regulated at 25 °C. Then, a mixture of oxygen and carbon dioxide was pushed within at a flow ratio of one. The overall flow rate of the mixed gases was set at 100 mL min^{-1} at atmospheric pressure. Figure 4.5 depicts the schematized apparatus for this experiment.

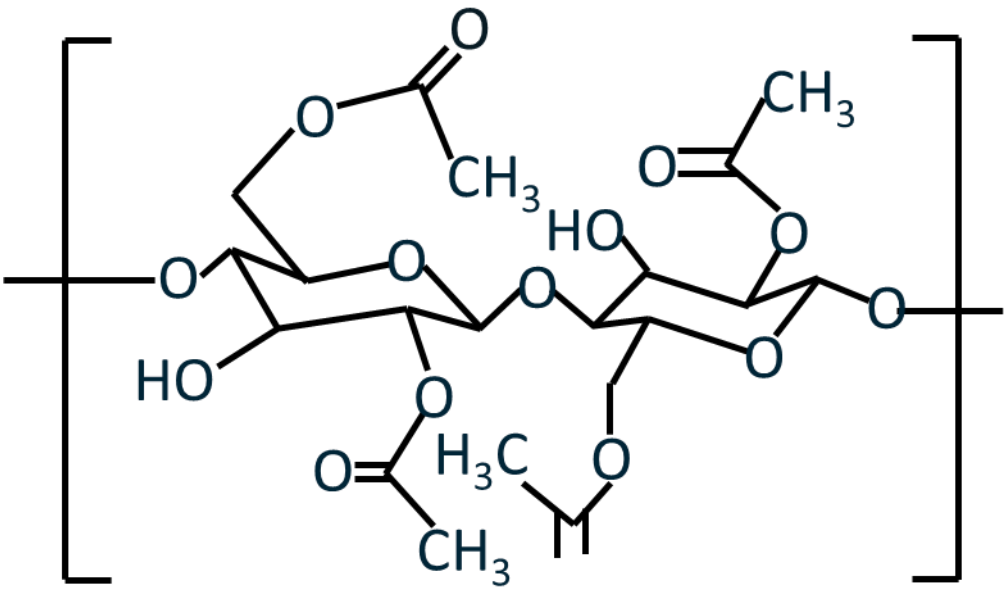

Figure 5.1 Molecular image of cellulose acetate (CA)

Table 5.1 Summary of the electrodes

Electrode No.	CNF : PVDF : NMP : acetone (g/g/g/g)	Drying condition		
		Method	Temperature (°C)	Pressure (MPa)
CA-0	1.0 : 1.0 : 16 : 16	Supercritical drying	40	20.0
	CNF : CA : acetone (g/g/g)			
CA-1	1.0 : 1.0 : 32	Supercritical drying	40	20.0
CA-2	1.0 : 0.5 : 32			
CA-3	1.0 : 0.3 : 32			
CA-4	1.0 : 0.1 : 32			
CA-5	1.0 : 1.0 : 32	Evaporation	40	0.1
CA-6	1.0 : 1.0 : 32	Supercritical drying	40	5
CA-7				7.5

Table 5.2 Density of CNF, PVDF, and CA

Substance	Density (g cm^{-3})	Ref.
Carbon nanofiber	1.9	*)
PVDF	1.6482	[1]
CA	1.3	*)

*) product specification

5.3 Result and discussion

5.3.1 Black slurry using a combinative organic solvent

In Chapter 3 , it was mentioned that acetone has the most significant expansion than other mentioned organic solvents. In this section, the possibility of NMP and acetone to improve the electrode performance was investigated. The summary of electrode materials and drying method is shown in Table 5.3. This section used only CNF as conductive materials. However, the solvents used for this section are NMP and acetone.

The images of the electrode using NMP as a solvent with evaporation drying are shown in Figure 4.21. While in Figure 4.24 shows the pictures of the electrode using NMP as a solvent and dried with supercritical drying. Finally, Figure 5.2 displays the images of the electrode using the combination of NMP and acetone as a solvent with supercritical drying. Those figures demonstrate the electrode's top-view image and the surface and cross-sectional images taken by SEM.

In Figure 4.21, PVDF aggregation can be observed on the surface of the electrode, while it does not exist in the other electrodes shown in Figure 4.24 and Figure 5.2. It shows that evaporation drying can form PVDF agglomeration when supercritical drying can prevent it.

While comparing Figure 4.21, Figure 4.24, and Figure 5.2, the thickness of each electrode varies. The thinnest electrode is the electrode with NMP and evaporation drying (Figure 4.21). On the contrary, the electrode contains NMP and acetone as the solvent and is dried by supercritical drying (Figure 5.2) is the thickest. Moreover, the electrode fabricated by evaporation drying has a significant difference in thickness compared with others produced with supercritical drying. Because, in evaporation drying, surface tension exists during the whole process. As the solvent evaporates from the black slurry, the mixture surface gets lower due to surface tension, and the pores formed inside the electrode collapse. On the other hand, looking back to the result and discussion in Chapter 3, the organic solvent in a supercritical CO_2 environment expanded before forming a homogenous phase in which surface tension does not exist. Consequently, when fabricating an electrode using this method, pores formed inside it do not collapse due to the absence of surface tension.

The thickness of the electrode fabricated by the supercritical CO_2 method with different solvent compositions is also diverse, which can be observed in Figure 4.24 and Figure 5.2. The reason for this occurrence also can be explained with the result and discussion in Chapter 3. In

Chapter 3, NMP and acetone in the supercritical CO_2 environment are investigated and the result shows that acetone expands more than NMP. Thus, it is evident that the electrode consisting of NMP and acetone can have a larger thickness than the electrode consisting of NMP only because the mixture containing acetone can expand larger. Therefore, the pores of this electrode (Figure 5.2) also look more prominent than the others (Figure 4.21 and Figure 4.24).

The porosity of each aerogel was calculated with the equation in section 4.2.3. First, the top area and thickness were calculated using an image analysis software, ImageJ, as mentioned in 4.2.3. Then, the total volume of the aerogels was determined by multiplying the top area and thickness (Equation 4.1). After that, the bulk volume of the aerogels was calculated by dividing CNF and PVDF weight by its density in Table 5.2 and void volume was determined by subtraction of actual total volume and bulk volume (Equation 4.2 and 4.3). Finally, the ratio of void volume and the actual total volume was calculated to get the porosity value. These calculation results are displayed in Table 5.4.

The calculation results were projected into a graph in Figure 5.3 and Figure 5.5. As shown in the bar diagram, aerogel fabricated by evaporation drying has the lowest porosity, while whether acetone was mixed with NMP does not have a significant difference in porosity. Evaporation drying results in low porosity and is the reason for thickness, where the pores inside the aerogel collapse with this method. Hence, both of thickness and porosity of the aerogel are lower than the aerogel made by supercritical drying. The mechanism difference is explained in Figure 5.6, wherein evaporation drying, the solution containing CNF decreases with time and thin and less porous aerogel was formed. On the other hand, supercritical CO_2 is dissolved into the solution in supercritical drying, which expands it and finally, thick and highly porous aerogel can be obtained.

In the case of the solution containing acetone, the porosity difference is slight despite the higher porosity than the solution not containing acetone. Even though the previous chapter shows that acetone can expand more than NMP in the presence of supercritical CO_2, the porosity itself does not change much. This phenomenon might happen because acetone is more volatile than NMP. Thus, acetone evaporates faster than NMP. Moreover, porosity was calculated by the ratio of void volume and total volume; hence the porosity cannot be bigger than 1. If both of the pore volumes shown in Figure 5.5 are compared, aerogel fabricated with acetone and NMP as solvent has approximately 1.4 times bigger void volume.

Table 5.3 Summary of the electrode

Electrode No.	CNF : PVDF : NMP : acetone (g/g/g/g)	Drying condition		
		Method	Temperature (°C)	Pressure (MPa)
C-10	1.0 : 1.0 : 32 : 0	Evaporation	80	0.1
C-13	1.0 : 1.0 : 32 : 0	Supercritical drying	40	20.0
CA-0	1.0 : 1.0 : 16 : 16	Supercritical drying	40	20.0

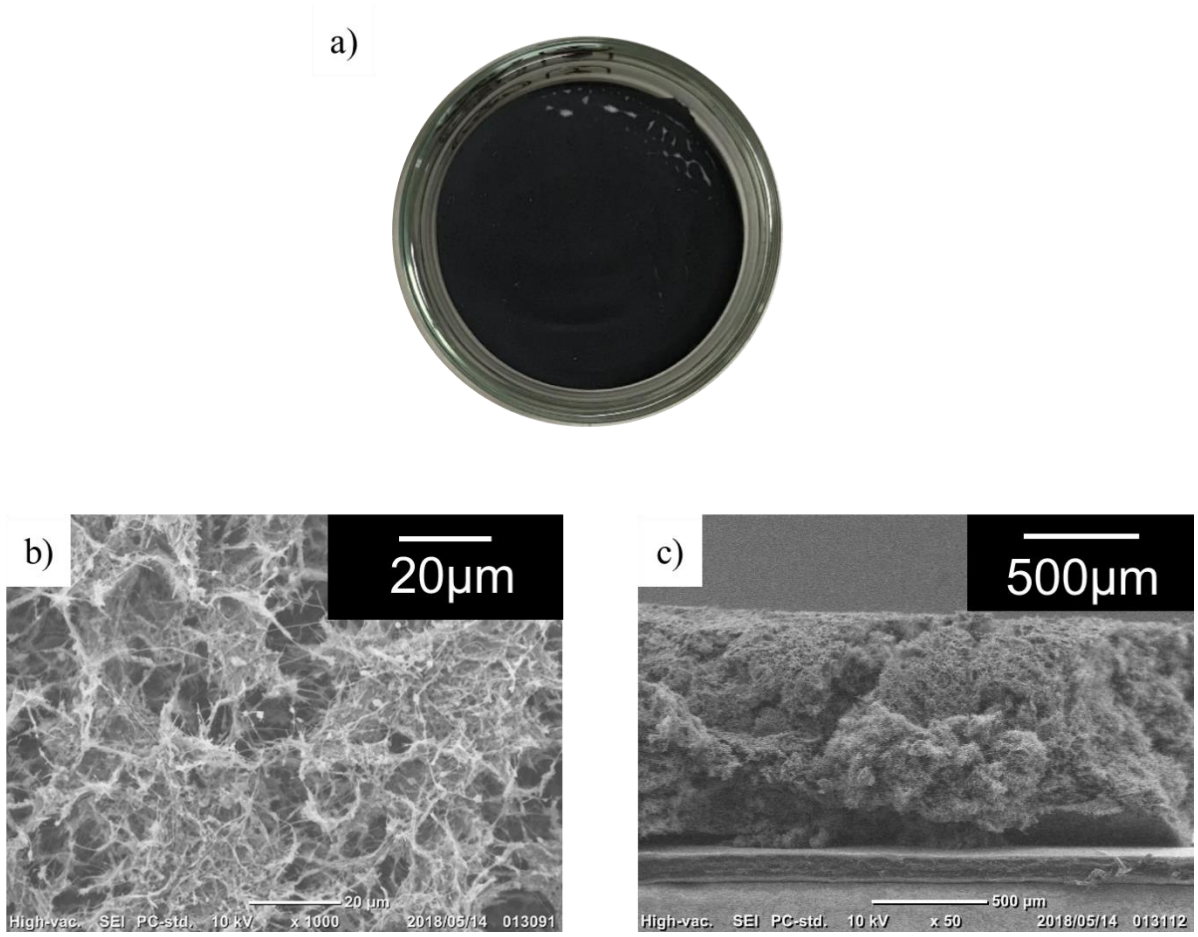

Figure 5.2 NMP+acetone/scCO_2 electrode (CA-0): a) Top view images, b) surface SEM images, and c) cross-section SEM images

Table 5.4 Porosity calculation of each electrode when CNF : PVDF : solvent = 1 : 1 : 32

Sample No.	Mass (g)	Top area (cm^2)	Thickness (cm)	Total volume (cm^3)	Density (g cm^{-3})	Void volume (cm^3)	Porosity	Pore volume (cm^3 g^{-1})
C-10	0.059	8.978	1.267	0.114	0.520	0.081	0.715	1.375
C-13	0.059	8.710	5.919	0.516	0.115	0.482	0.935	8.150
CA-0	0.059	8.075	8.829	0.713	0.083	0.680	0.953	11.514

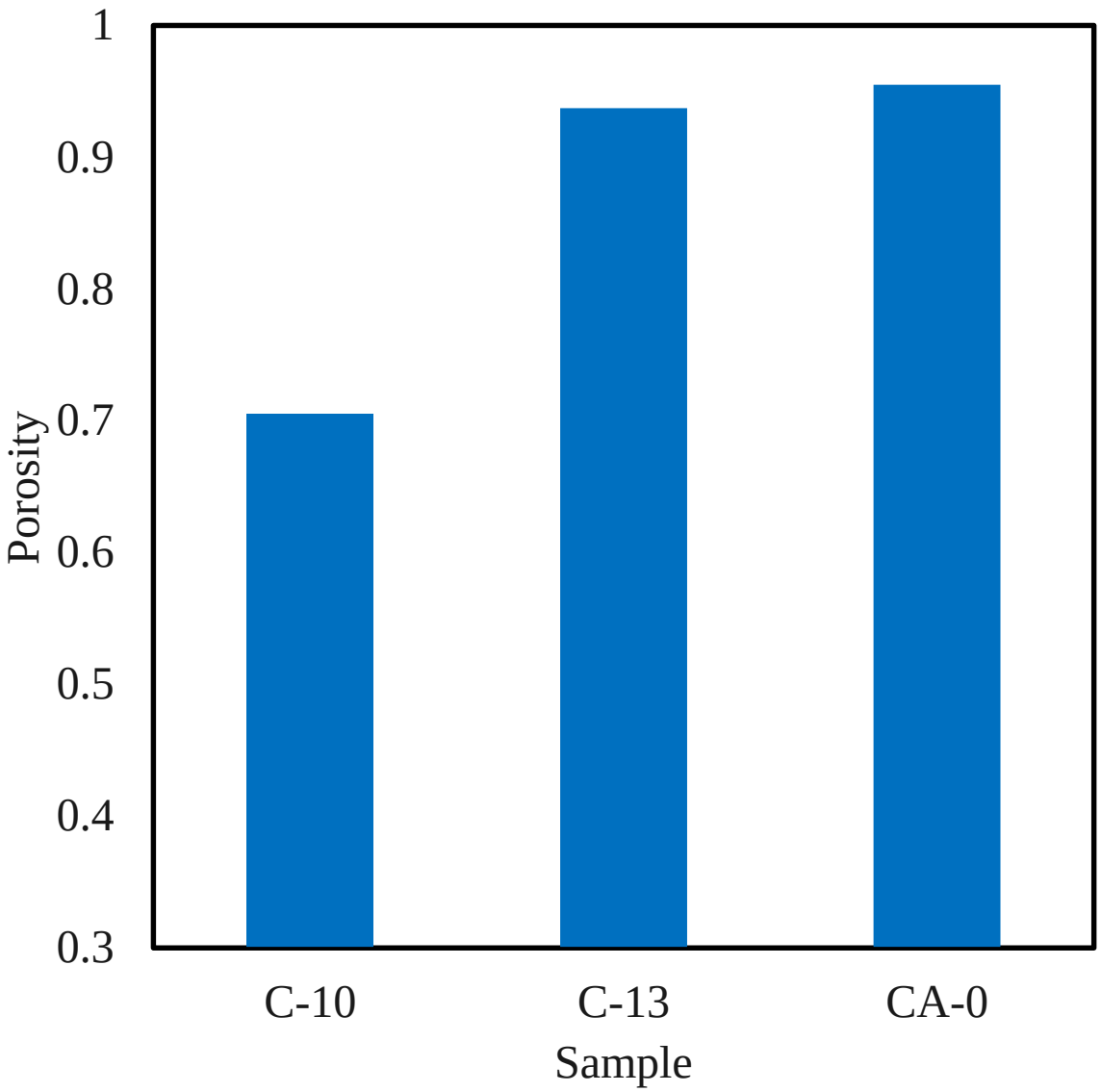

Figure 5.3 Porosity of CNF electrode fabricated with different solvent compositions

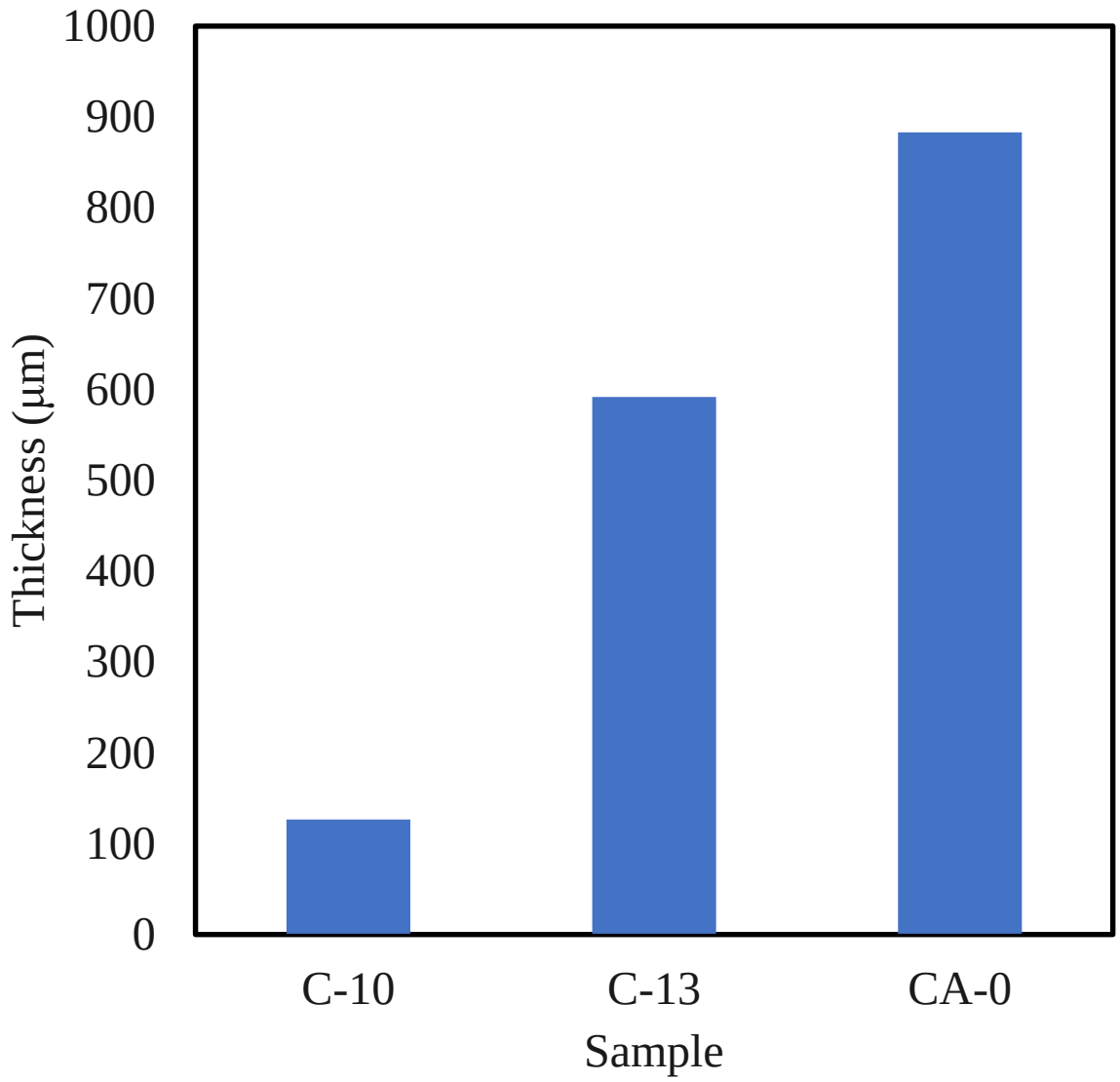

Figure 5.4 Thickness of CNF electrode fabricated with different solvent compositions

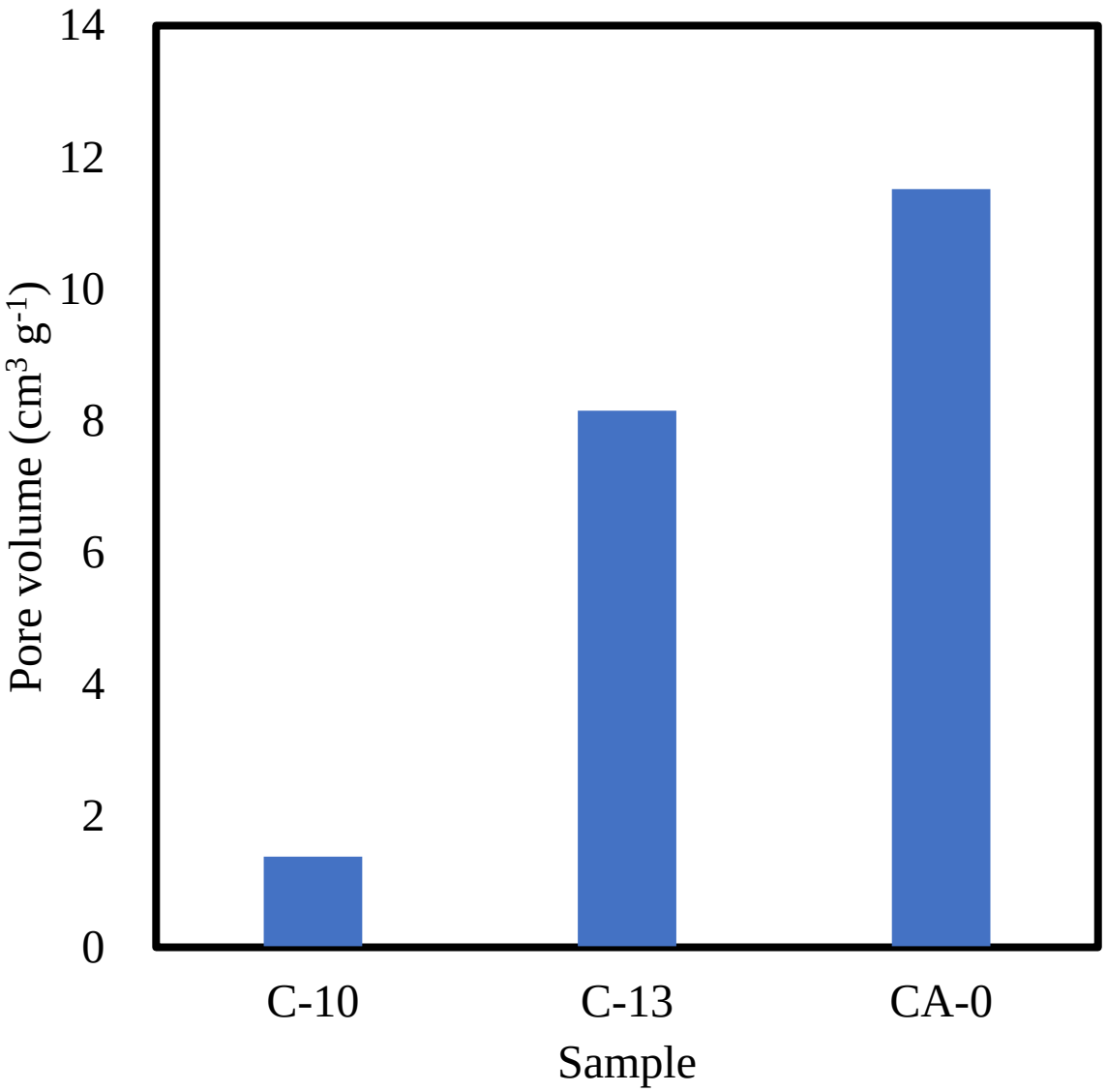

Figure 5.5 Pore volume of CNF electrode fabricated with different solvent compositions

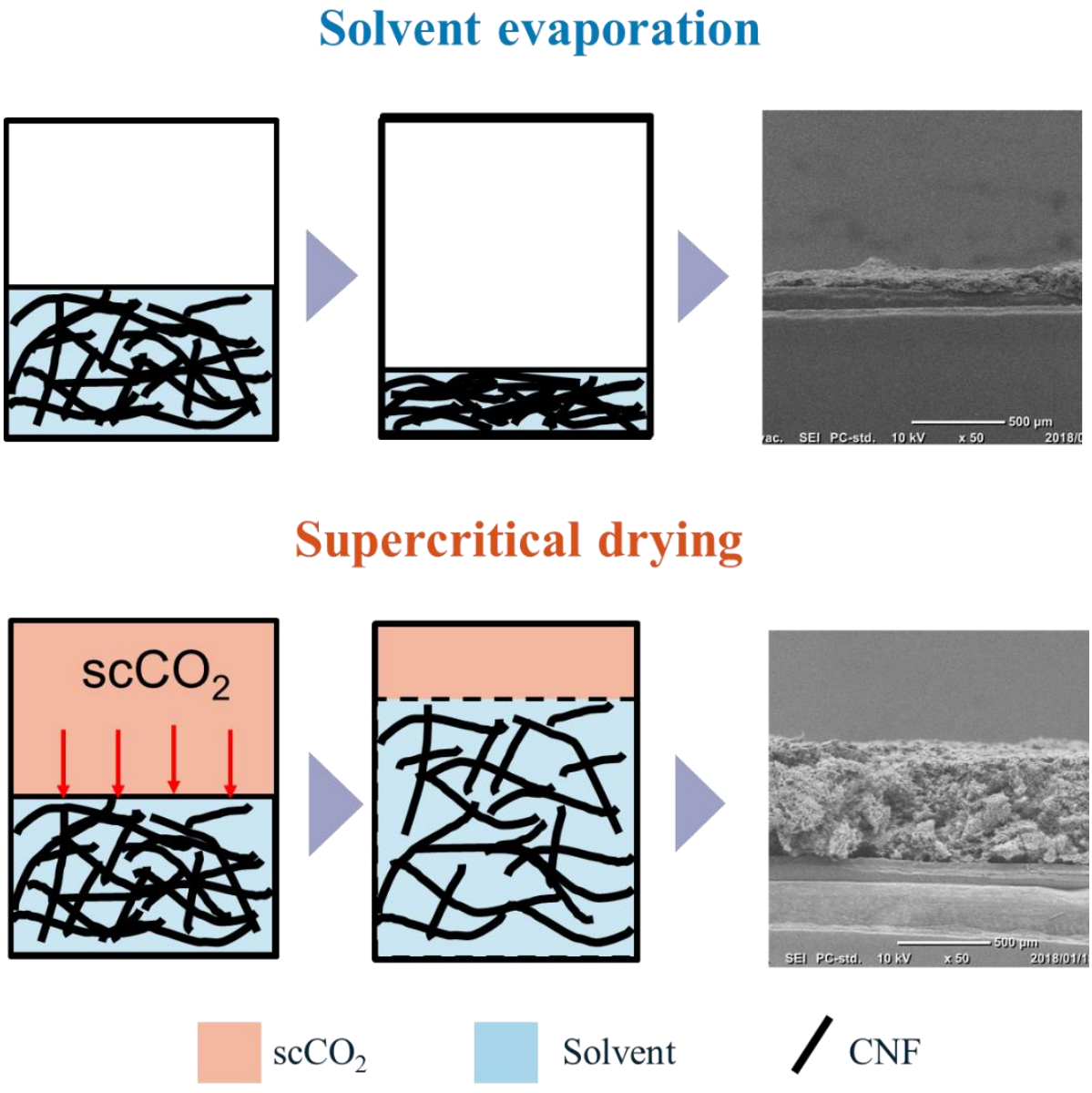

Figure 5.6 Illustration of solvent evaporation drying and supercritical drying process

5.3.2 CNF/CA aerogel

In the previous section, combining NMP and acetone as solvents can increase an electrode's thickness and void volume. Moreover, in a study, a high porosity of carbon electrodes is proven to be very effective in increasing a battery's specific capacity [2]. On the other hand, NMP has a high boiling point [3] which affects the time length for the drying process, while acetone has a low boiling point [4] that can fasten the drying process. Consequently, to further improve the electrode and modify the time efficiency of electrode manufacturing, an idea was to completely change the solvent from NMP to acetone. However, a high temperature is necessary to dissolve PVDF in acetone since acetone is a latent solvent to PVDF [5].

An alternative binder is also necessary to replace the organic solvent from NMP with acetone. In search of an alternative binder, our research group found studies about cellulose acetate. Cellulose acetate is produced from wood and is non-hazardous, biodegradable, and environmentally friendly [6, 7]. Although its conductivity is small [8], the most crucial characteristic is its solubility in acetone [9, 10].

The summary of CNF/CA electrodes for this section is displayed in Table 5.5. CA-1 to CA-4 were fabricated with supercritical drying at 40 °C and 20 MPa, while their different aspects are the amount of binder. CA-1 has the highest, and CA-4 has the lowest amount of binder. The amount of binder was varied not only to investigate the possibility of fabricating CNF/CA electrodes with supercritical drying but also to study the effect of it on the battery performance.

Figure 5.7 to Figure 5.10 shows the top view images, surface SEM images, and cross-section SEM images of electrodes CA-1 to CA-4. From these top-view and surface SEM images, a conclusion can be drawn that there is no significant difference between the electrodes.

Table 5.6, Figure 5.11, and Figure 5.13 show the porosity calculation and porosity graph for CNF/CA electrodes. From the graph, the CNF/CA electrodes' porosity does not change significantly; only a slight increase can be observed where C-4 has the highest porosity value. However, in Figure 5.13, the differences of pore volume are clear. C-4 electrode has the highest porosity and pore volume because it contains more solvent and, consequently, has less solid. Because, in the drying process, supercritical CO_2 is dissolved into the solvent before extracting it from the drying system. Consequently, more solvent causes more supercritical CO_2 to be

dissolved, and more porous can be formed. This phenomenon is similar to section 4.3.1, where C-4, which contains more solvent, has the highest porosity and pore volume.

The thickness of CNF/CA electrodes is shown in Figure 5.12. This graph also shows that the thickness also relatively increases with less binder. However, CA-4 is relatively less thick when it contains the least binder. The thickness and surface area determine the total volume of an electrode (Equation 4.1). However, porosity comes from the electrode void volume and total volume (Equation 4.3) when the void volume is determined by subtracting the bulk volume from the actual volume (Equation 4.2). Since the bulk volume is calculated by the ratio of solid weight and electrode density, the bulk volume value will be low when the binder contained in the electrode is low. Consequently, the porosity is high even with a smaller thickness value. A thinner structure might happen because of low binder support since the binder amount is minimal.

Then, for representative, CA-1 and CA-3 were arranged into coin cells to test the specific capacity of the battery compared to the result of the CNF/PVDF electrode in Chapter 4. The result of the specific capacity measurement is displayed in Figure 5.14. The graph shows that CA-3, which has a low binder ratio, has a higher specific capacity because when the binder ratio is small, there are more exposed CNFs where the reaction occurs, which leads to an increase in the specific capacity of the battery. Moreover, compared to CNF/PVDF electrode in section 4.3.3, CNF/CA with the same ratio gives 7.44 mA h cm^{-2} for the value of specific capacity, which is similar to the CNF/PVDF electrode. Consequently, CNF/CA can also be considered one of the material choices in making an electrode.

Table 5.5 Summary of CNF/CA electrode

Electrode No.	CB : CA : acetone (g/g/g/g)	Drying condition		
		Method	Temperature (°C)	Pressure (MPa)
CA-1	1.0 : 1.0 : 32	Supercritical drying	40	20.0
CA-2	1.0 : 0.5 : 32			
CA-3	1.0 : 0.3 : 32			
CA-4	1.0 : 0.1 : 32			

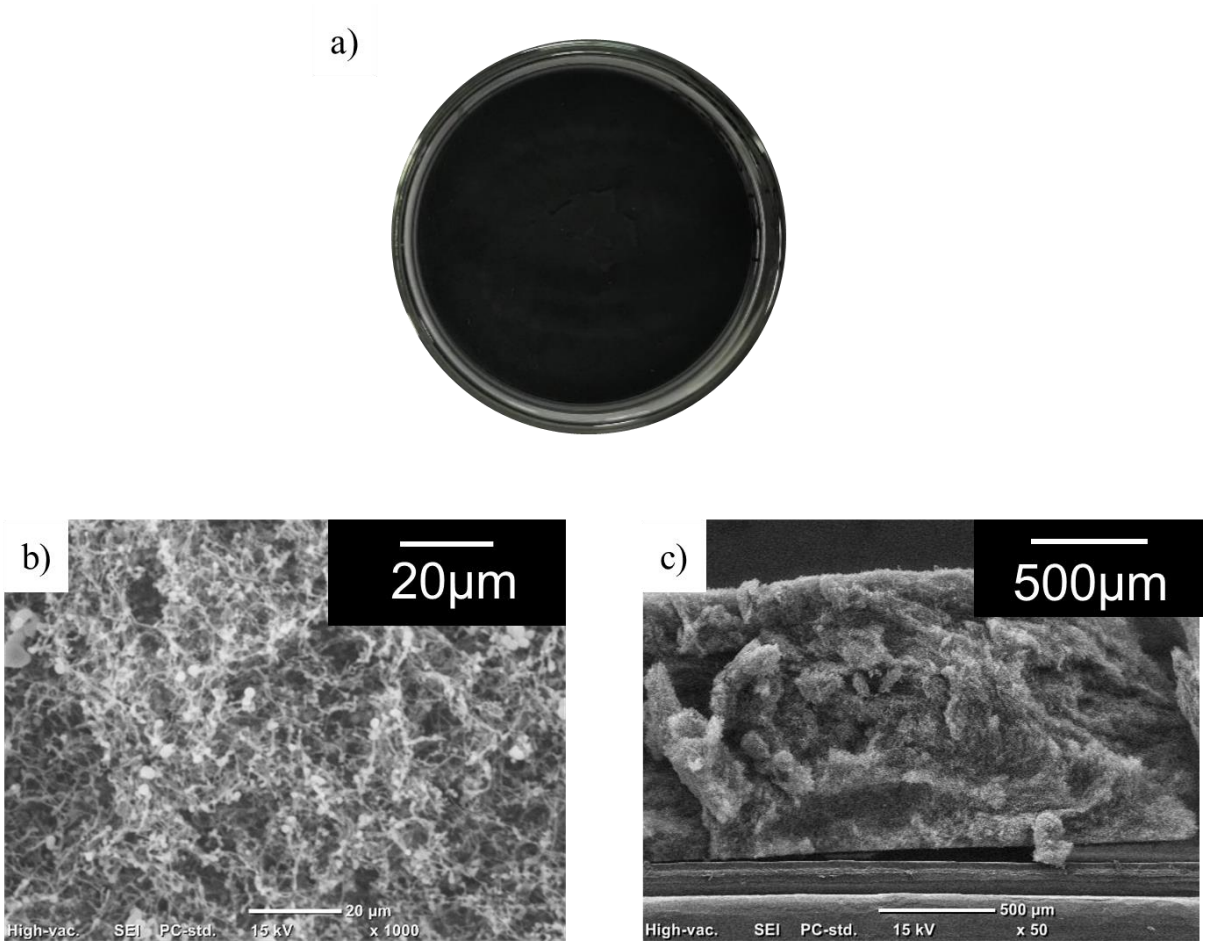

Figure 5.7 CNF/CA electrode (CA-1): a) Top view images, b) surface SEM images, and c) cross-section SEM images

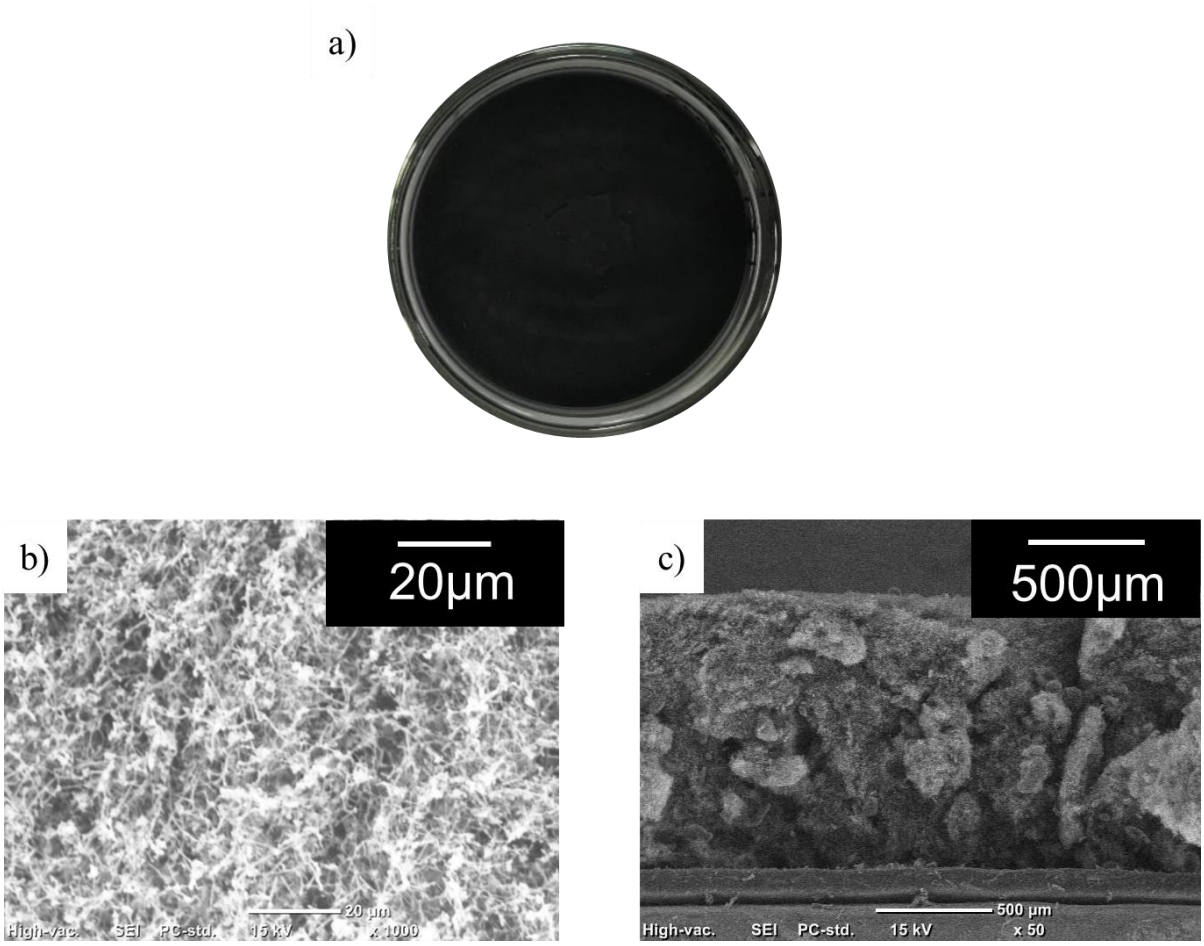

Figure 5.8 CNF/CA electrode (CA-2): a) Top view images, b) surface SEM images, and c) cross-section SEM images

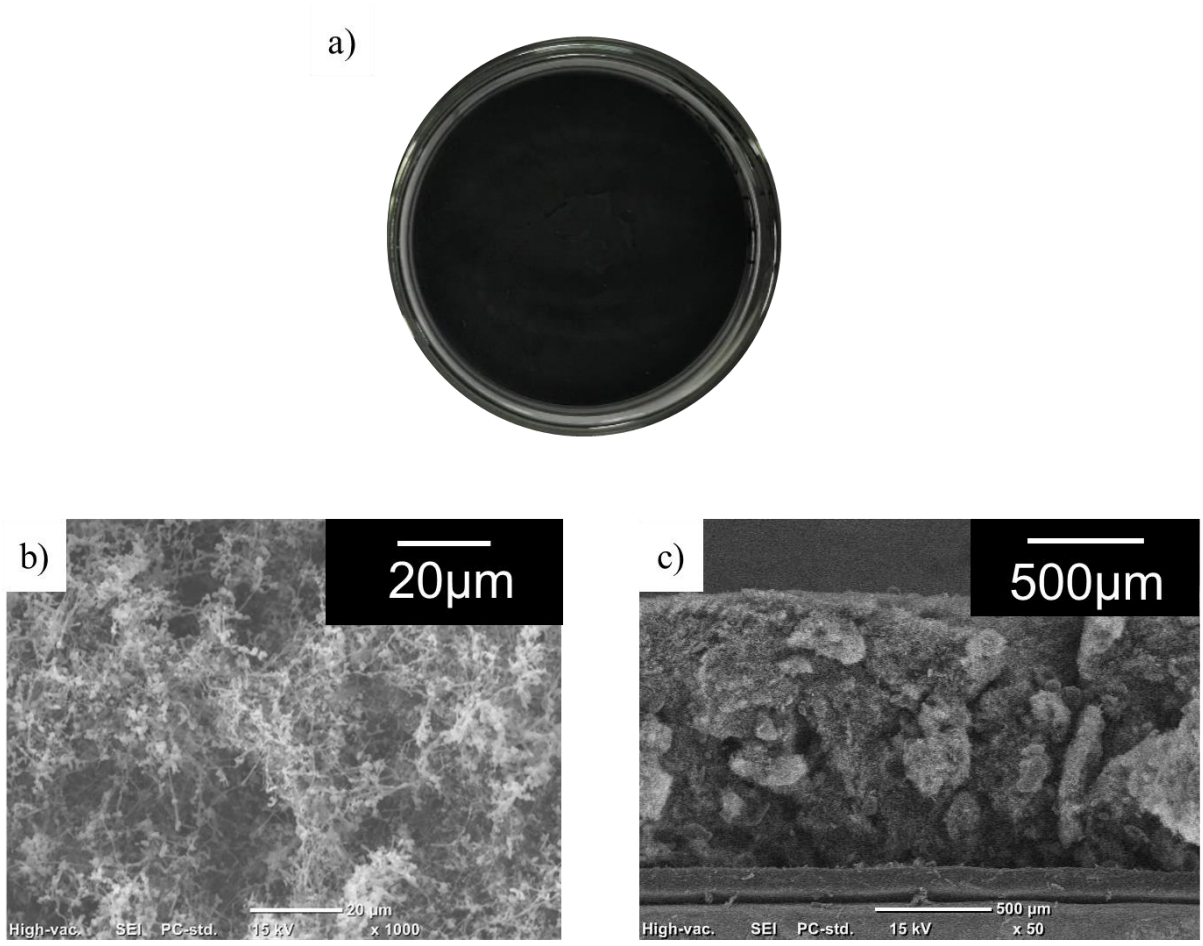

Figure 5.9 CNF/CA electrode (CA-3): a) Top view images, b) surface SEM images, and c) cross-section SEM images

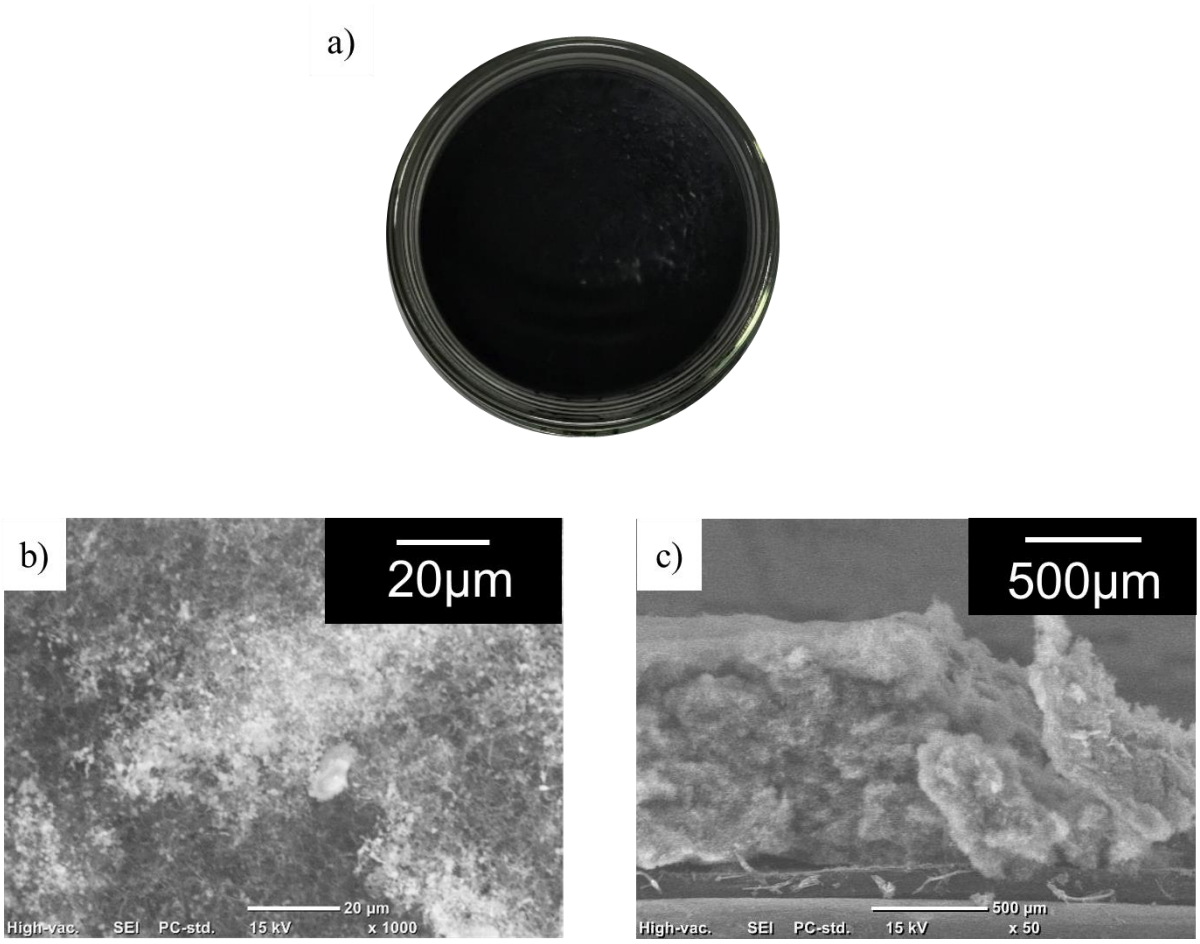

Figure 5.10 CNF/CA electrode (CA-4): a) Top view images, b) surface SEM images, and c) cross-section SEM images

Table 5.6 Porosity calculation of CNF/CA electrode with different amount of CA

Sample No.	Mass (g)	Top Area (cm^2)	Thickness (mm)	Total Volume (cm^3)	Density (g cm^{-3})	Void volume (cm^3)	Porosity	Pore Volume (cm^3 g^{-1})
CA-1	0.060	8.724	11.819	1.031	0.058	0.992	0.962	16.520
CA-2	0.045	7.209	12.436	0.897	0.051	0.869	0.969	19.128
CA-3	0.040	8.537	13.110	1.119	0.036	1.096	0.979	27.310
CA-4	0.034	8.754	12.366	1.083	0.031	1.064	0.983	31.383

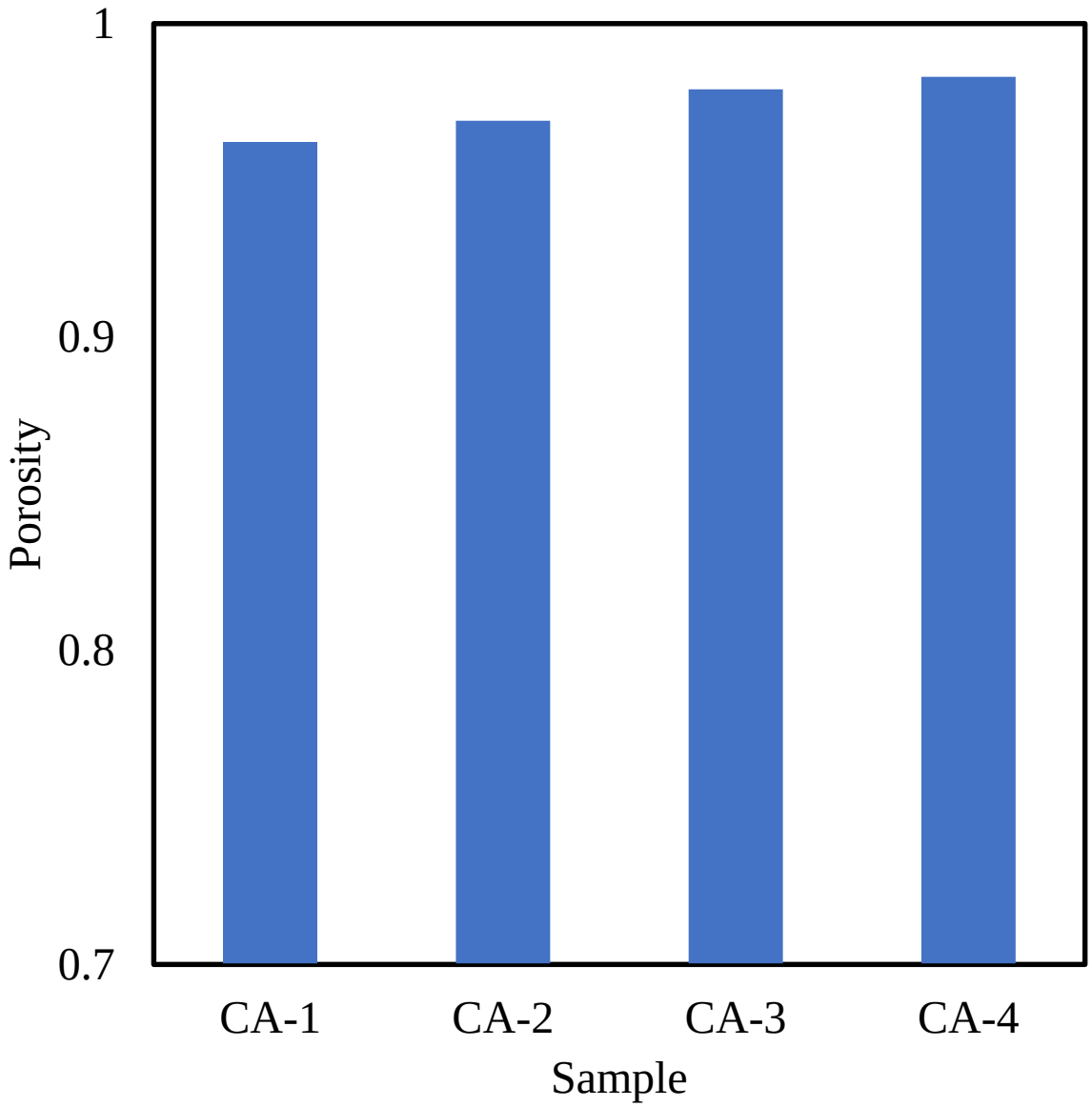

Figure 5.11 Porosity of CNF/CA electrode fabricated with different amount of CA

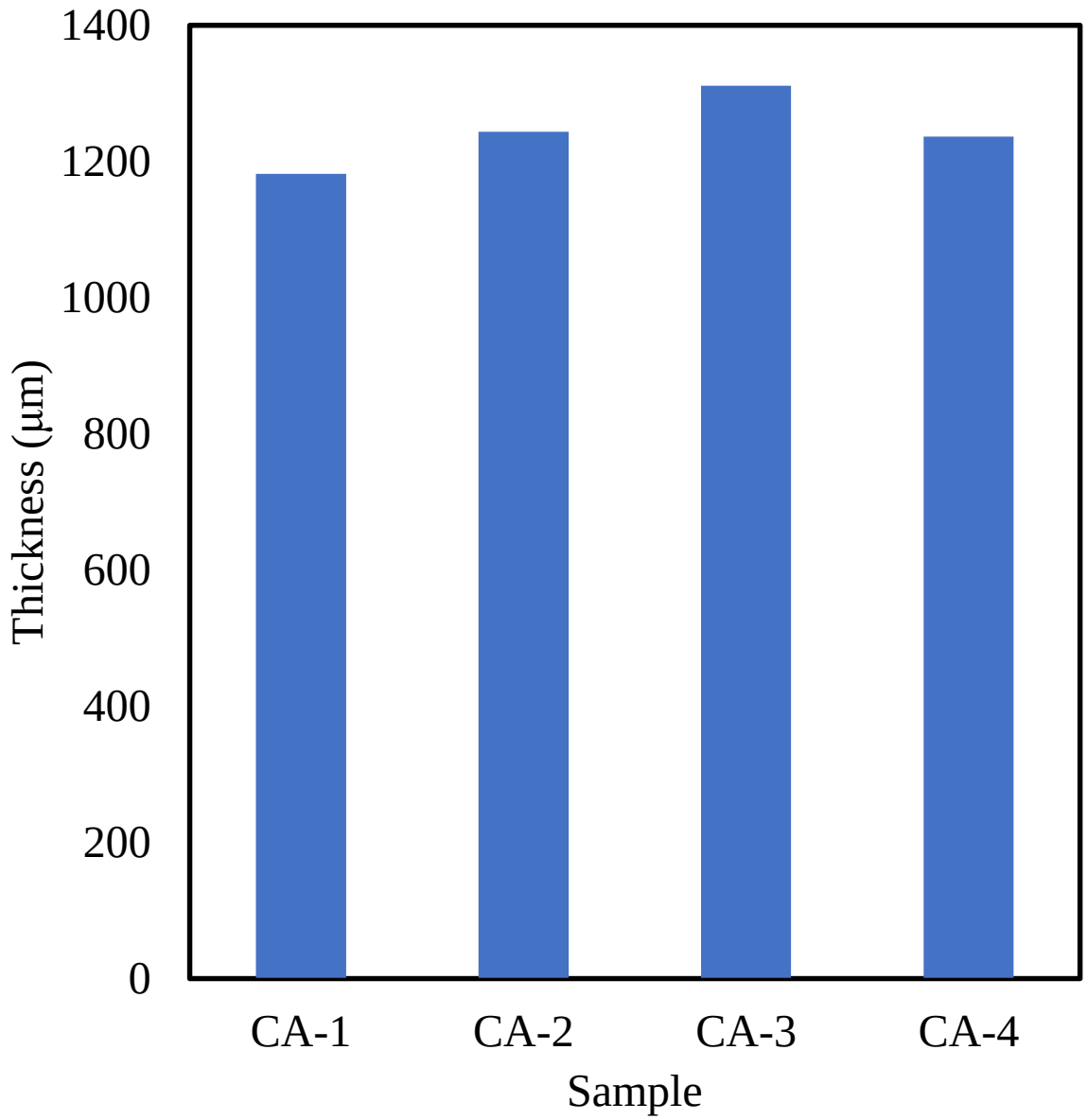

Figure 5.12 Thickness of CNF/CA electrode fabricated with different amounts of CA

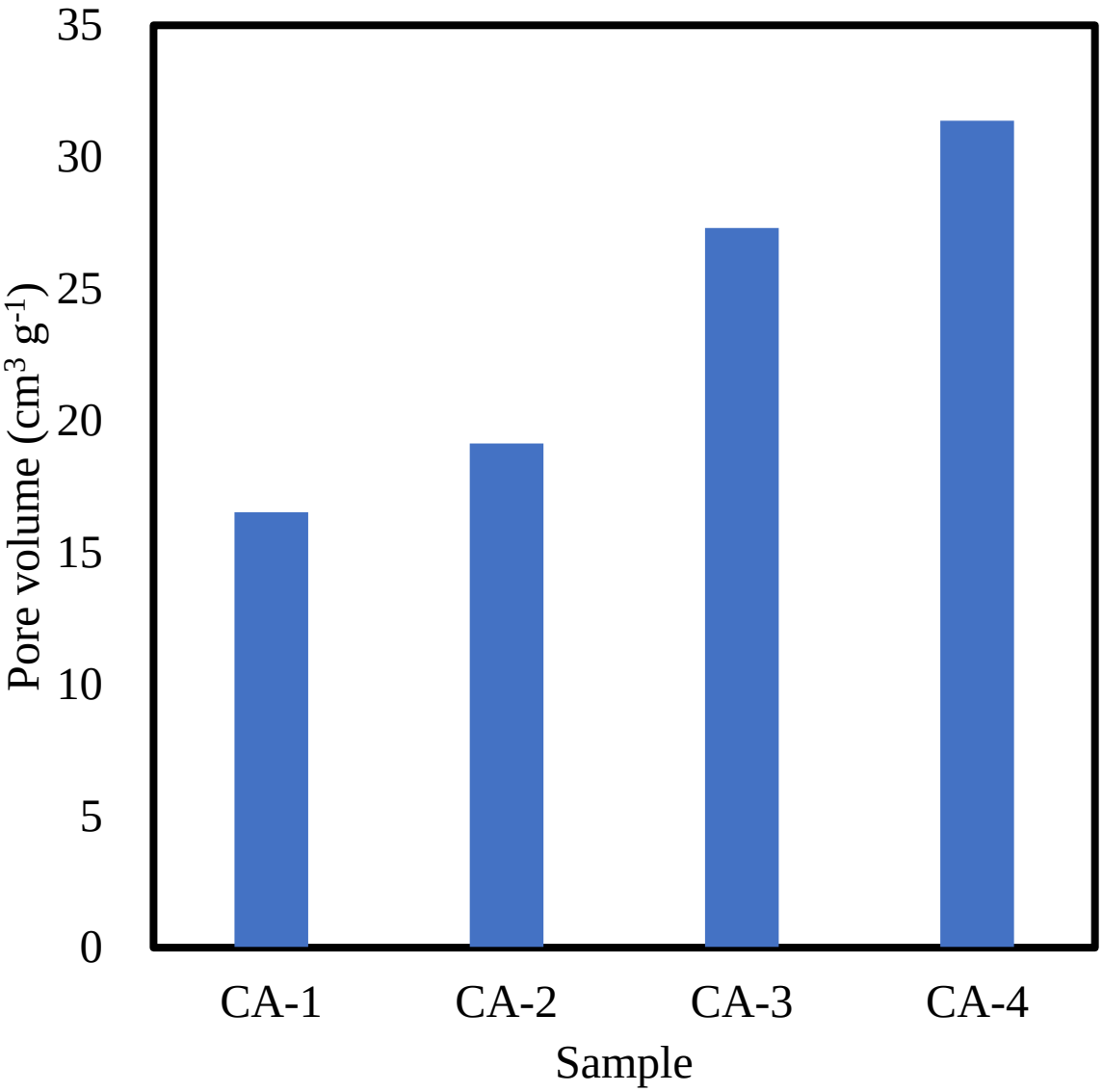

Figure 5.13 Pore volume of CNF/CA electrode fabricated with different amount of CA

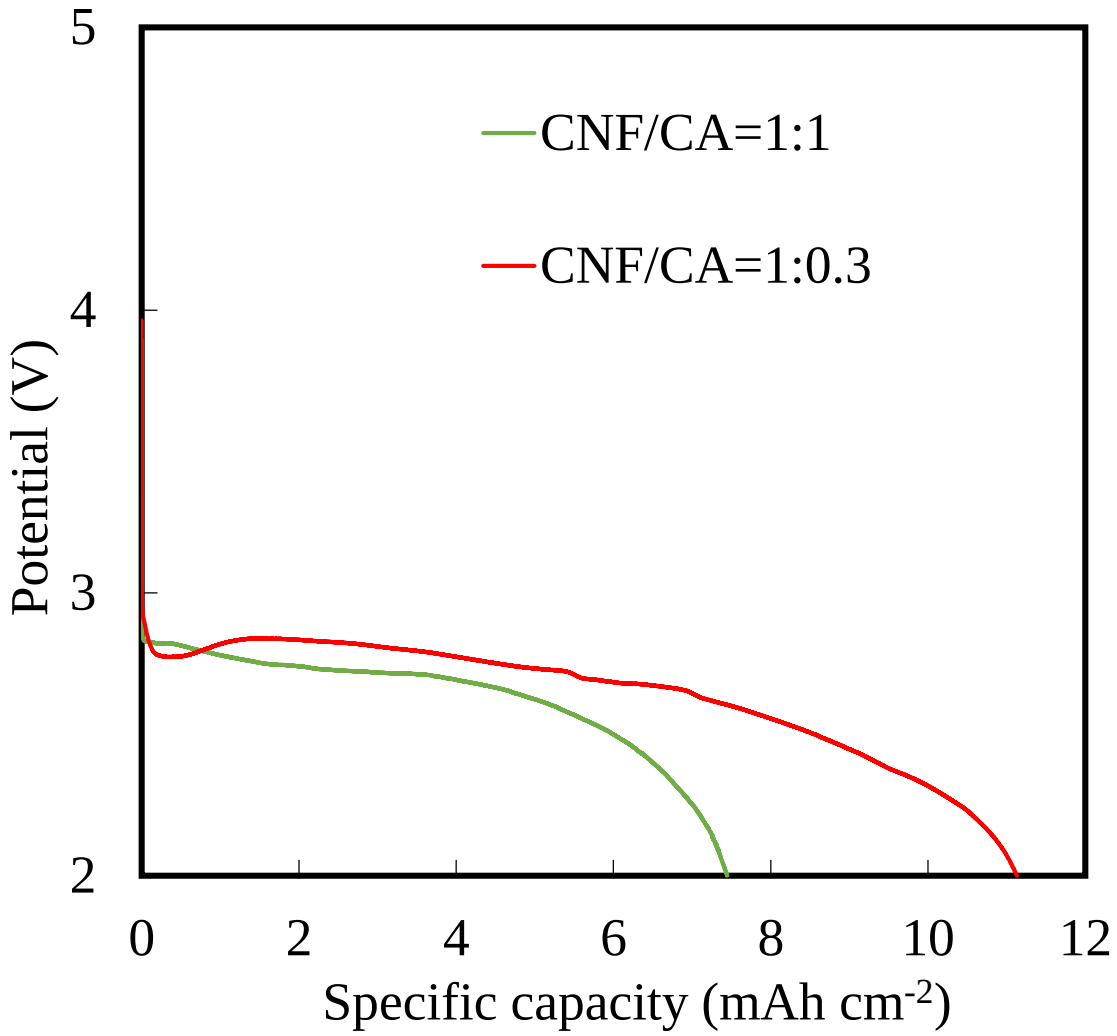

Figure 5.14 Specific capacity of CNF/CA electrode with the ratio of CNF:CA=1:1 (CA-1, red) compared to the ratio of CNF:CA=1:0.3 (CA-3, green)

5.3.3 Low-pressure drying

Low-pressure drying was conducted to investigate whether it is possible to get a highly porous electrode at a low pressure higher than atmospheric pressure. The summary of this experiment is displayed in Table 5.7.

These electrodes' top view, surface SEM, and cross-section SEM images are shown in Figure 5.15, Figure 5.16, Figure 5.17, and Figure 5.7. From Figure 5.16, it is clear that below the critical pressure, at 5 MPa, the electrode already has fine porous on the surface. However, observing the cross-sectional image, the electrode is not expanded as the electrodes dried at a pressure higher than critical pressure, in this case, 7.5 MPa in Figure 5.17.

The porosity calculation is summarized in Table 5.8 and then plotted into a graph in Figure 5.18, while the thickness and pore volume graph is plotted in Figure 5.19 and Figure 5.20. Figure 5.18 shows that the porosity of electrodes fabricated below the critical pressure is lower than electrodes fabricated above the critical pressure. On the other hand, electrodes made above the critical pressure have high porosity and thickness. This phenomenon is related to the result in Chapter, section 3.3.3. In the case of NMP, the solvent's expansion still increases after reaching CO_2 critical pressure, and the expansion rate becomes stable after reaching 20 MPa. However, in using acetone as a solvent, acetone expands after reaching CO_2 critical pressure increases and falls after reaching 20 MPa. Looking at Figure 3.20, the expansion rates of acetone when the pressure is just above the critical pressure and 20 MPa, have similar values.

In a study of CB/PVDF electrode fabrication with supercritical drying, drying the electrodes with different pressure will result in different porosities. When the drying pressure is low, the porosity will be low, and when the drying pressure is high, the porosity will also be high [2]. However, in this research, using acetone as a solvent for CNF/CA electrode fabrication by supercritical drying, drying in relatively low pressure (7.5 MPa) and high pressure (20 MPa) result in an insignificant difference in porosity and thickness with an increase in pore volume at 7.5 MPa. In conclusion, fabricating CNF electrode in low pressure is possible and similar battery performance can be expected when using acetone as a solvent for producing electrodes. By utilizing low pressure, energy consumption in increasing pressure also can be reduced. Moreover, using acetone as a solvent can shorten the time for electrode

production since acetone only needs 1.5 hours to dry, while using NMP as a solvent needs 6 hours to dry.

Table 5.7 Summary of CNF/CA electrodes dried in low pressure

Electrode No.	CB : PVDF : NMP (g/g/g/g)	Drying condition		
		Method	Temperature (°C)	Pressure (MPa)
CA-5	1.0 : 1.0 : 32	Evaporation	40	0.1
CA-6				5
CA-7	1.0 : 1.0 : 32	Supercritical drying	40	7.5
CA-1				20.0

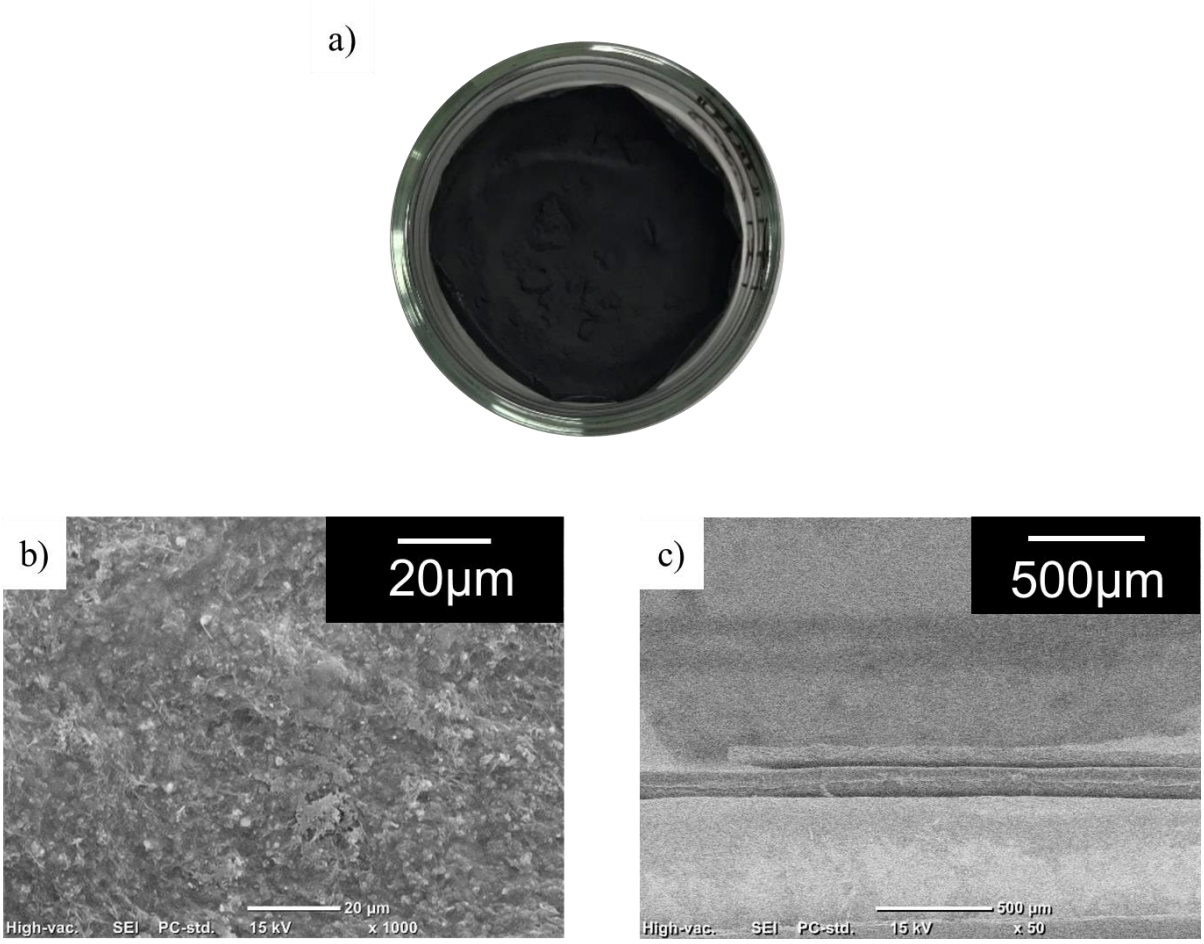

Figure 5.15 CNF/CA electrode dried at 0.1 MPa (CA-5): a) Top view images, b) surface SEM images, and c) cross-section SEM images

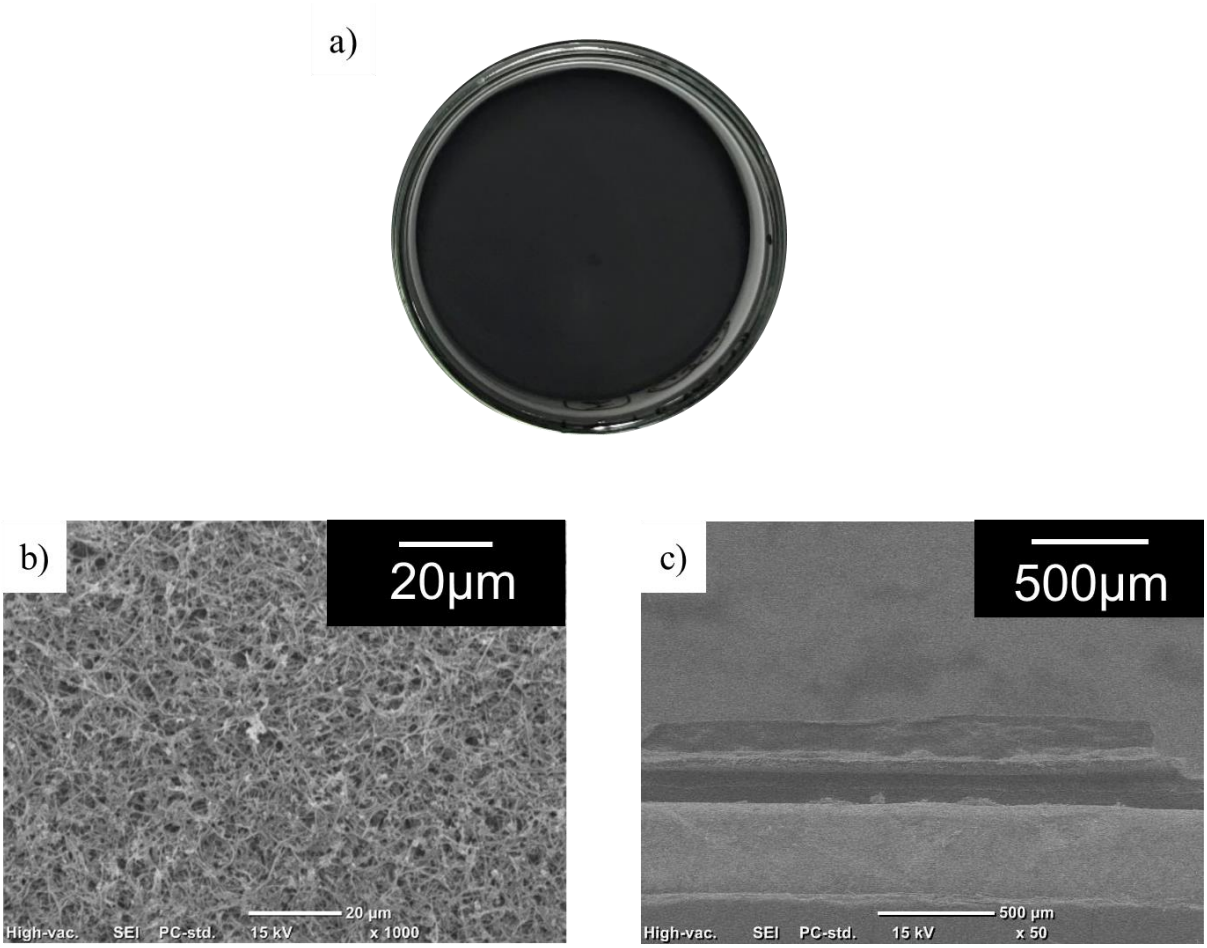

Figure 5.16 CNF/CA electrode dried at 5 MPa (CA-6): a) Top view images, b) surface SEM images, and c) cross-section SEM images

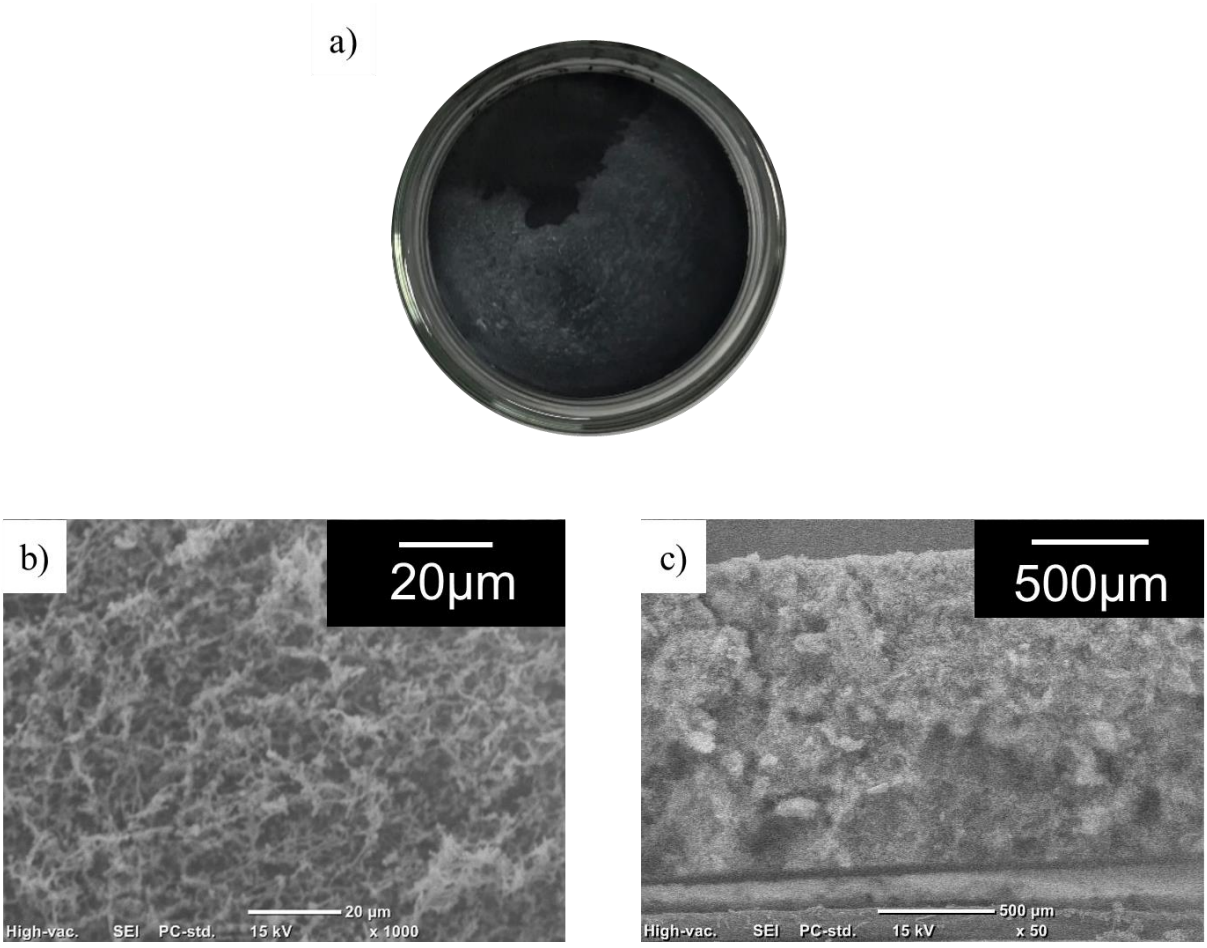

Figure 5.17 CNF/CA electrode dried at 7.5 MPa (CA-7): a) Top view images, b) surface SEM images, and c) cross-section SEM images

Table 5.8 Porosity calculation of CNF/CA electrode dried at low pressure

Sample No.	Mass (g)	Top area (cm^2)	Thickness (mm)	Total volume (cm^3)	Density (g cm^{-3})	Void volume (cm^3)	Porosity	Pore Volume (cm^3 g^{-1})
CA-5	0.059	8.412	0.579	0.049	1.219	0.010	0.210	0.172
CA-6	0.061	13.270	1.635	0.217	0.281	0.178	0.818	2.915
CA-7	0.060	9.315	12.657	1.179	0.050	1.140	0.967	19.158
CA-1	0.060	8.724	11.819	1.031	0.058	0.992	0.962	16.520

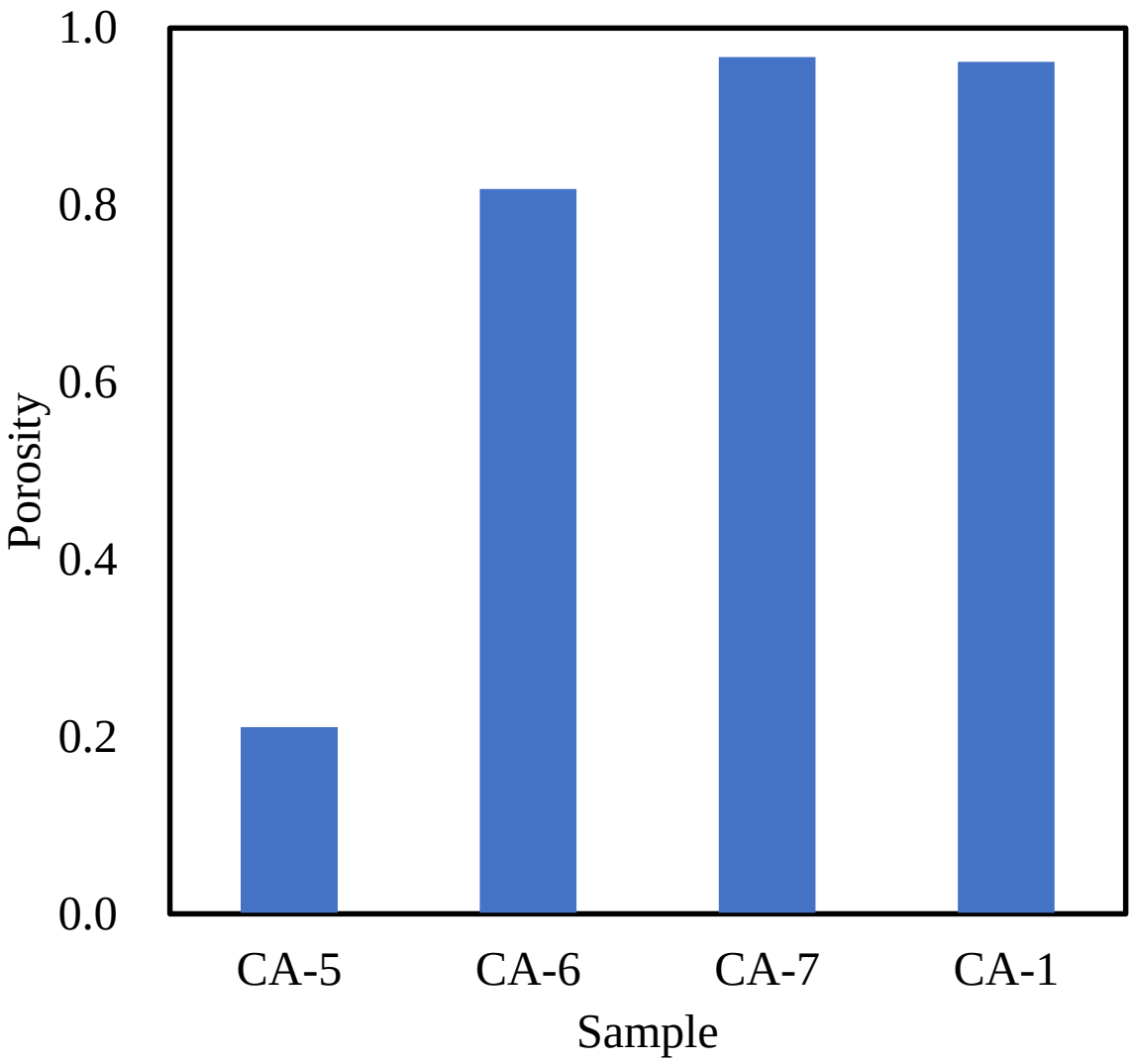

Figure 5.18 Porosity of CNF/CA electrode fabricated with at low pressure and high pressure

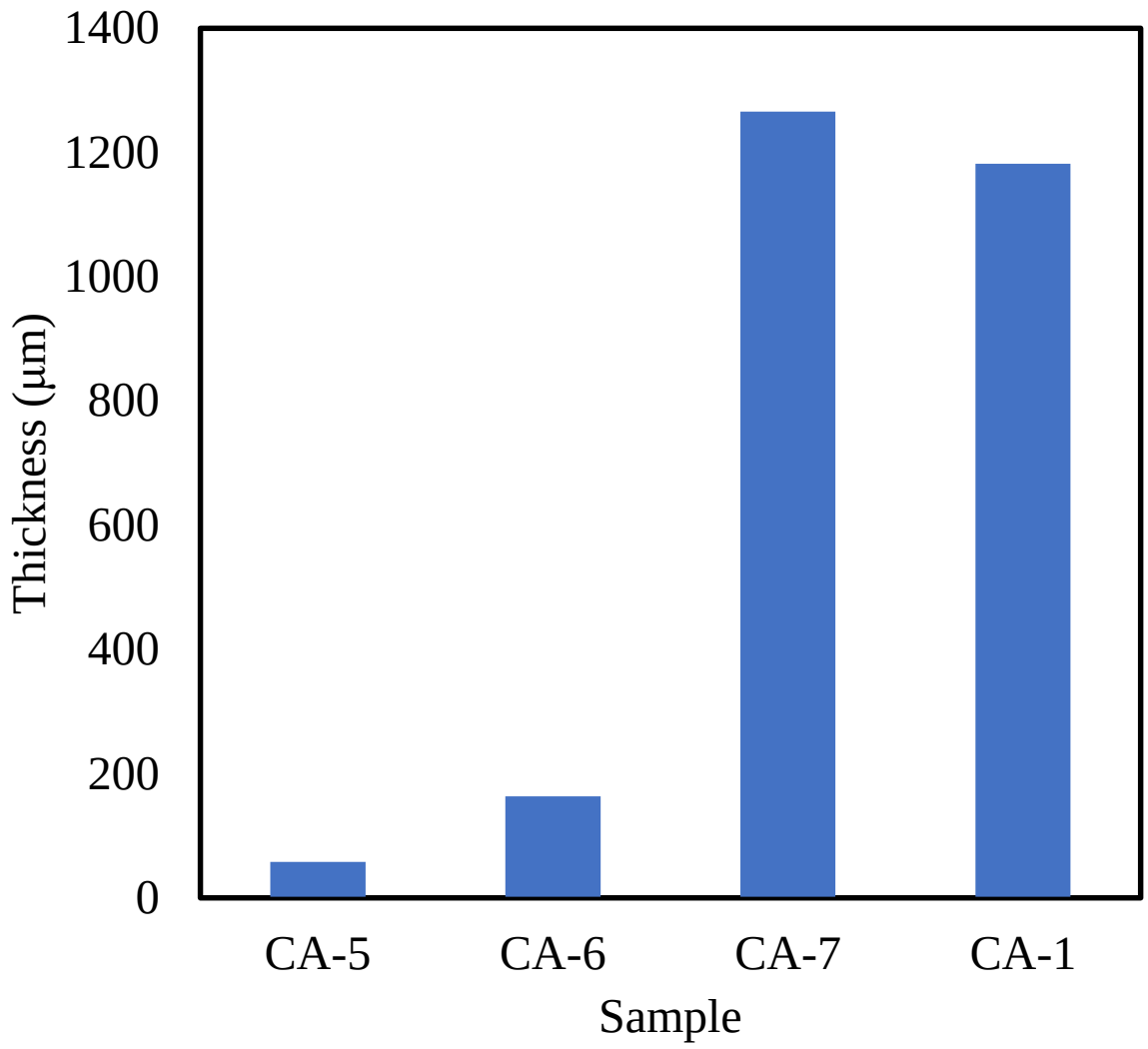

Figure 5.19 Thickness of CNF/CA electrode fabricated at low pressure and high pressure

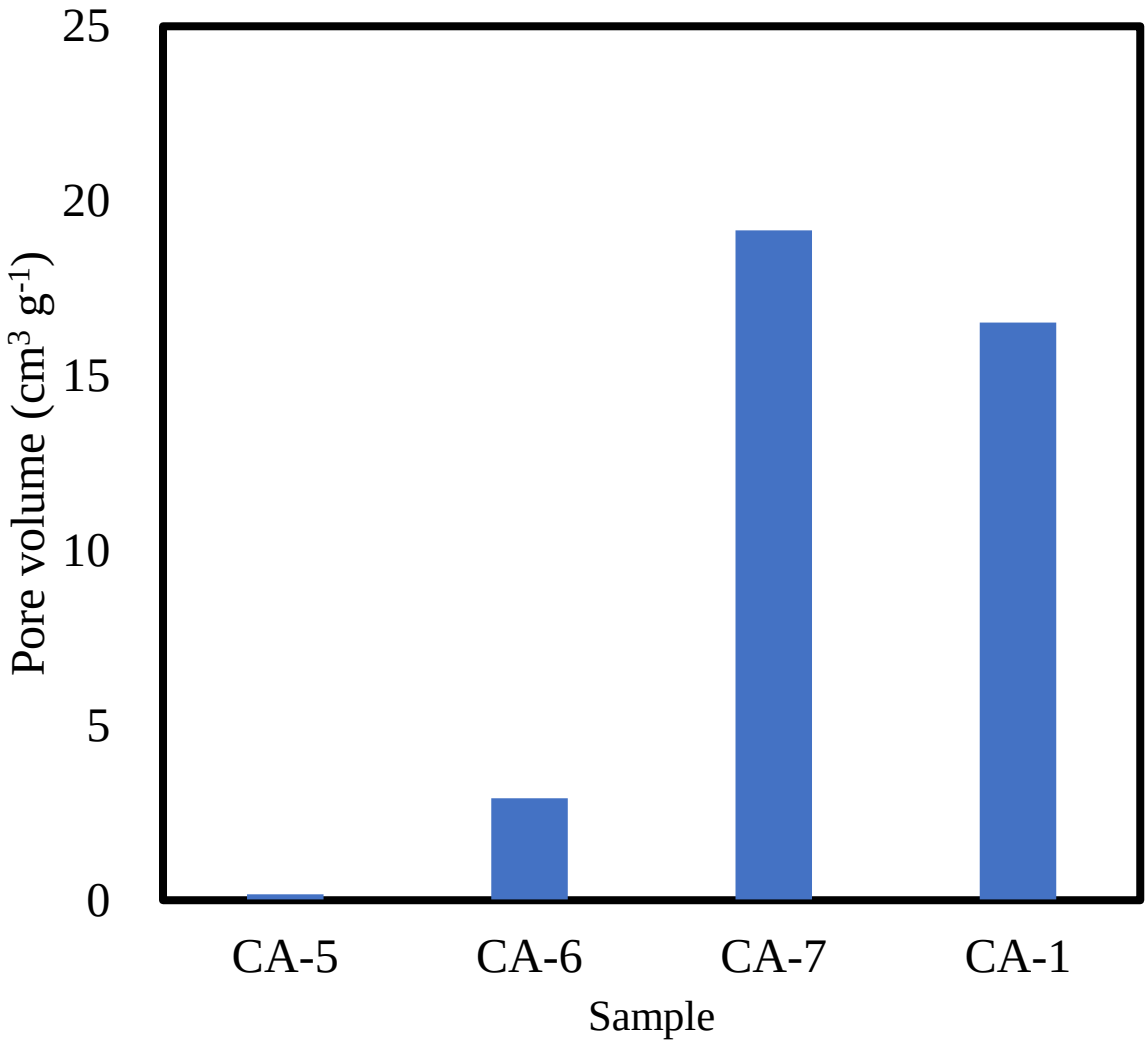

Figure 5.20 Pore volume of CNF/CA electrode fabricated at low pressure and high pressure

5.5 References

[1] Nattanai Kunanusont, "Master dissertation", Tokyo institute of technology, Tokyo (2017)

[2] Kunanusont, Nattanai, and Yusuke Shimoyama, "Porous carbon electrode for Li-air battery fabricated from solvent expansion during supercritical drying", *The Journal of Supercritical Fluids* 133 (2018) 77-85

[3] McKeen, Laurence W, "Solvent Systems", *Fluorinated Coatings and Finishes Handbook (Second Edition)* (2016) 107-118

[4] Jon W. Wong and Kai Zhang, "Solvent-Based Extraction Techniques for the Determination of Pesticides in Food", *Comprehensive Sampling and Sample Preparation* (2011)

[5] Chengtian Zhou, Sourav Bag, Bowen Lv and Venkataraman Thangadurai, "Understanding the Role of Solvents on the Morphological Structure and Li-Ion Conductivity of Poly(vinylidene fluoride)-Based Polymer Electrolytes", *Journal of The Electrochemical Society* 167 (2020)

[6] Kiyofumi Sakai, Tatsuo Yamauchi, Fumiko Nakasu, Tatsuhiko Ohe, "Biodegradation of cellulose acetate by Neisseria sicca", *Bioscience, biotechnology, and biochemistry* 60 (1996) 1617–1622

[7] Kaur, Gaganjot, Grewal, Jasleen, Jyoti, Kiran, Jain, Upendra K., Chandra, Ramesh, and Jitender Madan, "Oral controlled and sustained drug delivery systems: Concepts, advances, preclinical, and clinical status", *Drug Targeting and Stimuli Sensitive Drug Delivery Systems* (2018) 567-626

[8] Endang W. Laksono, Marfuatun, and Demas Aji, "Conductivity of Cellulose Acetate Membranes from Pandan Duri Leaves (Pandanus tectorius) for Li-ion Battery", *MATEC Web of Conferences* 64 (2016)

[9] B. Ghorani, S. J. Russell, P. Goswami, "Controlled Morphology and Mechanical Characterisation of Electrospun Cellulose Acetate Fibre Webs", *International Journal of Polymer Science* 2013 (2013)

[10] Cardea, Stefano, and Iolanda De Marco, "Cellulose Acetate and Supercritical Carbon Dioxide: Membranes, Nanoparticles, Microparticles and Nanostructured Filaments", *Polymers* 12 (2020) 162

Chapter 6 Conclusion

6.1 Summary of this work

This work can be summarized as follows:

(1) A slow pressurization rate leads to high solvent expansion and a slower formation of homogeneous phase because of slower CO_2 intake. (Chapter 3)

(2) CO_2 and NMP under high temperatures show no substantial impact on solvent expansion rate. However, due to reduced CO_2 density, CO_2 intake into the solvent is slower, resulting in a slower-to-form homogeneous phase. The solvent expansion of ethanol and acetone, on the other hand, decreases significantly with rising temperature because their vapor pressure increases dramatically at high temperatures, and solvents evaporate faster, reducing the expansion rate. (Chapter 3).

(3) Varying solvents have different expansion rates and durations, resulting in a homogeneous phase. Acetone with high vapor pressure creates a homogeneous phase more quickly. Furthermore, the dielectric constant or polarity and the vapor pressure influence the solvent expansion rate. (Chapter 3)

(4) A small amount of solvent leads to a faster expansion rate and a slower formation of a homogeneous phase. The CO_2 outlet flow rate does not affect the solvent expansion rate or the time required to establish a homogeneous phase. (Chapter 3)

(5) The solvent amount in supercritical drying affects the porosity of electrodes. Where a higher amount of solvent results in higher porosity. Moreover, drying temperature does not significantly impact porosity, but drying at high temperatures can result in the cracking of electrodes. (Chapter 4)

(6) Carbon nanofiber electrode delivers higher specific Li-O_2/CO_2 battery capacity because it has a more approachable reaction site, while carbon black electrode has less because PVDF covers them. Carbon nanofiber's mechanical strength can increase the battery's cyclability and endure ten cycles. (Chapter 4)

(7) Carbon nanofiber electrode produced by supercritical CO_2 enhances porosity considerably. Although mixing NMP with acetone as a solvent for constructing electrodes does not dramatically modify porosity, thickness is increased due to the presence of acetone, as described in point (3). (Chapter 5)

(8) CNF/CA electrodes give a high porosity of over 95%. The porosity does not differ much with various amounts of a binder. Furthermore, CNF/CA and CNF/PVDF electrodes with the same ratio give similar results in the specific capacity of the batteries. (Chapter 5)

(9) Even though a study explains that the porosity of electrodes using NMP as the solvent and made by supercritical drying is affected by drying pressure, electrodes using acetone as the solvent is not significantly affected by drying pressure. Therefore, CNF/CA with acetone as a solvent can be considered an alternative for making highly porous electrodes, accounting for efficient drying time, lower energy consumption (low pressure can be used), and excellent battery performance. (Chapter 5)

6.2 The direction of future work

Although much data can be retrieved for solvent expansion, using the latest technology in computing science, it will be handy if calculation and fitting for supercritical CO_2 parameters can be estimated to control the porosity and thickness of the material by simulation or machine learning. Furthermore, it will also be beneficial if we can get data on what combination of conductive materials, binders, and solvents will be better for the battery system by machine learning or simulation.

List of awards and conferences

1. Awards

[1] Silver prize (銀賞)

Shofiyah Sakinah, “Porous carbon electrode fabricated from supercritical drying”, Tokyo Institute of Technology, Faculty of Engineering, Department of Chemical Engineering, Chemical Engineering Course Bachelor Thesis Presentation, Tokyo, Japan, February 2018

[2] Excellent student’s presentation award (優秀賞)

Shofiyah Sakinah, Nattanai Kunanusont, Takashi Nishioka, Yusuke Shimoyama, “Thick and porous electrode fabrication from solvent swelling and drying by supercritical carbon dioxide”, 20th Society of Chemical Engineering Japan Student Presentation, Tokyo, Japan, March 2018

[3] Excellent Student Award for Outstanding Academic Achievement (優秀学生賞)

Tokyo Institute of Technology, March 2018

[4] Excellent student’s presentation award (優秀学生賞)

Shofiyah Sakinah, Nattanai Kunanusont, Yusuke Shimoyama, “Expanded carbon nanofiber aerogel by supercritical carbon dioxide”, 26th Society of Chemical Engineering Japan Regional Meeting in Muroran 2018, Muroran, Japan, August 2018

[5] Special Student Award (学生特別賞)

Shofiyah Sakinah, Nattanai Kunanusont, Yusuke Shimoyama, “Solvent expansion on homogeneous formation of organic solvent phase with high-pressure CO_2 phase”, Society of Chemical Engineering Japan Regional Meeting in Yokohama 2019, Yokohama, Japan, August 2019

2. Conferences

[1] Shofiyah Sakinah, Mika Sasaki, Masahide Hagiri, “Silver (I) Ion Exchange of hardened paste of α-Tricalcium Phosphate and Polycarboxylic Acid”, 1st Kitakanto-Ban'etsu Forum on Chemical Technology and Bioengineering, Hitachi, Japan, December 2015

[2] Shofiyah Sakinah, Mika Sasaki, Masahide Hagiri, “Development of photocatalytic activity for Silver (I) Ion Exchange of hardened paste of α-Tricalcium Phosphate and Polycarboxylic Acid”, College symposium in Kagawa, Kagawa, Japan, January 2016

[3] Shofiyah Sakinah, Nattanai Kunanusont, Takashi Nishioka, Yusuke Shimoyama, “Thick and porous electrode fabrication from solvent swelling and drying by supercritical carbon dioxide”, 20th Society of Chemical Engineering Japan Student Presentation, Tokyo, Japan, March 2018

[4] Shofiyah Sakinah, Nattanai Kunanusont, Yusuke Shimoyama, “Expanded carbon nanofiber aerogel by supercritical carbon dioxide”, 26th Society of Chemical Engineering Japan Regional Meeting in Muroran 2018, Muroran, Japan, August 2018

[5] Shofiyah Sakinah, Nattanai Kunanusont, Yusuke Shimoyama, “Fabrication of expanded carbon nanofiber aerogel using supercritical carbon dioxide drying”, 8th CSJ Festa 2018, Tokyo, Japan, October 2018 (Poster)

[6] Shofiyah Sakinah, Yusuke Shimoyama,” Fabrication of chitosan aerogel using supercritical drying for air dehydration application”, Society of Chemical Engineering Japan’s 84th Annual meeting, Tokyo, Japan, March 2019 (Poster)

[7] Shofiyah Sakinah, Nattanai Kunanusont, Yusuke Shimoyama, “Solvent expansion on homogeneous formation of organic solvent phase with high-pressure CO_2 phase”, Society of Chemical Engineering Japan Regional Meeting in Yokohama 2019, Yokohama, Japan, August 2019

[8] S. Sakinah, N. Kunanusont, Y. Shimoyama,” Carbon nanofiber aerogel fabricated by supercritical drying and application in Li-O2/CO_2”, IMPRES 2019, Kanazawa、Japan, October 2019 (International conference, poster)

[9] S. Sakinah, Y. Orita, Y. Shimoyama, “Enhanced solvent expansion during supercriticaly drying for fabrication of porous carbon nanofiber electrode on Li-

O2/CO2 battery", International Chemical Engineering Symposia 2021, D314, Japan, (2021)

3. Publications

[1] Shofiyah Sakinah, Nattanai Kunanusont, Yusuke Shimoyama, "Carbon nanofiber aerogel fabricated by supercritical drying and application in Li-O_2/CO_2 Battery", Journal of Chemical Engineering of Japan, Vol. 54, No. 5, pp. 239-247, 2021

[2] Hagiri, M., Uchida, K., Kamo Sasaki, M. et al. "Preparation and characterization of silver orthophosphate photocatalytic coating on glass substrate". Sci Rep 11, 13968 (2021)